WESTERN PACIFIC PALEOCEANOGRAPHY ACROSS THE EARLY–MIDDLE PLEISTOCENE BOUNDARY (~773 KA, MARINE ISOTOPE STAGE 19): DINOFLAGELLATE CYSTS OF THE CHIBA COMPOSITE SECTION, JAPAN

Eseroghene Jedidiah Balota

Department of Earth Sciences

A thesis submitted in partial fulfilment of the requirements for the degree of

M.Sc. in Earth Sciences

Faculty of Mathematics and Science, Brock University

St. Catharines, Ontario

©2018

DEDICATION

This thesis is dedicated to God almighty, my fiancée, Ife, my parents and siblings.

ABSTRACT

The Chiba composite section, central Boso Peninsular, Japan, is a candidate Global Boundary Stratotype Section and Point for the Early–Middle Pleistocene Subseries boundary. This well-exposed, continuous and expanded marine silty sedimentary succession has a detailed paleomagnetic record and an ultra-high-resolution oxygen isotope stratigraphy supported by U-Pb zircon dating of the Byk-E tephra bed which occurs ~1 m below the Matuyama–Brunhes boundary. A detailed dinoflagellate cyst (dinocyst) study from late Marine Isotope Stage (MIS) 20 to late MIS 19 provides information on paleoceanographic changes in the Western Pacific Ocean between 791 and 770 ka. During Termination IX, a decrease in heterotrophic species (e.g. *Brigantidinium* spp., *Selenopemphix nephroides*) and corresponding increase in warm-water autotrophs (e.g. *Spiniferites hyperacanthus*/*mirabilis*, *Spiniferites* sp. 2) indicate a progressive decline in productivity corresponding to deglaciation and a transition from cold nutrient-rich waters of MIS 20 to warm conditions in MIS 19. This gradual warming is interrupted by a sudden but brief cooling at 790 ka which is also reflected in the MAT-based dinocyst sea-surface temperature (SST) for February and August. The dinocyst record shows a gradational response to the onset of MIS 19c. Abundant warm-water autotrophic dinocysts during MIS 19c reflects warm conditions and a northward shift of the warm Kuroshio current from 786 to 773 ka. The end of MIS 19c is marked by a sharp decrease in species richness and evenness, an abrupt and sustained rise to dominance of *Protoceratium reticulatum,* and a corresponding increase in dinocyst concentrations, indicating an increase in productivity and presaging the onset of the MIS 18 glaciation. Pollen and spore concentrations show a strong terrestrial influence during MIS 19. During the peak of MIS 19, *Tsuga* has low abundance while angiosperm pollen (deciduous broadleaved trees) increase significantly, which is similar to vegetation presently dominant in the northeastern part of the Japanese archipelago.

ACKNOWLEDGEMENTS

Many thanks to God almighty who enabled me to start and complete this work. I am immensely grateful to Prof. Martin J. Head, my supervisor, for guiding me through this work. He introduced me to this research on the Chiba section and provided all the resources for its successful completion. I really appreciate his mentorship and relentless sharing of knowledge with me. I thank Prof. Makoto Okada for his great support and for providing all the samples analysed in this research. I appreciate the efforts of the Chiba research members for their ongoing work on the Chiba section, which gave me great insight and knowledge in writing this thesis. I thank Prof. Francine McCarthy and Prof. Rick Cheel for their kind support and for providing more insight to this thesis. I appreciate my wonderful colleagues, Mukudzei Dube, Saif Silwadi and Walid Abomriga, who were also very helpful in sharing their knowledge with me on dinoflagellate cysts. I gratefully acknowledge research funding from a Natural Sciences and Engineering Research Council of Canada (NSERC) Discovery Grant to Prof. Martin J. Head, Brock University graduate funding, and the Dean of Graduate Studies Spring 2016 Research Scholarship from the Faculty of Graduate Studies, Brock University.

Words alone cannot express my appreciation for my fiancée, Ifelayo, for her unconditional love for me. She was always beside me throughout this research offering words of encouragement and motivation. I am indebted to my wonderful parents for their huge support, prayers, words of advice and frequent calls. I also thank my siblings; Evwophia, Egaverere and Eguolo for their support, Emma Totor for his financial support, Pastor Ifeanyi and Obiageli Uzoka for their material and financial support, and all DLCM members in Canada for helping me in one way or another during my MSc program. I thank you all.

TABLE OF CONTENT

LIST OF FIGURES

LIST OF TABLES

LIST OF PLATES

LIST OF COMMONLY USED ABBREVIATIONS

GSSP:	Global Boundary-Stratotype Section and Point
MIS:	Marine Isotope Stage
MAT:	Modern Analogue Technique
SST:	Sea-Surface Temperature
SSS:	Sea-Surface Salinity
ODP:	Ocean Drilling Program
IODP:	Integrated Ocean Drilling Program
EPICA:	European Project for Ice Coring in Antarctica
HCl:	Hydrochloric Acid
HF:	Hydrofluoric Acid
EAWM:	East Asian Winter Monsoon

CHAPTER ONE

1.1 Introduction

The Chiba composite section, located in the central Boso Peninsula, Chiba Prefecture, Japan, is one of three candidate global boundary stratotype sections and points (GSSPs) for the Middle Pleistocene Subseries, and the only candidate for the Pacific realm (Head and Gibbard 2005, 2015a, b; Head et al., 2008). It is a marine section exposed on land and consists of an expanded and continuous silty sedimentary sequence that bears excellent records of paleoceanographic and paleoclimatic changes across the Early–Middle Pleistocene boundary; this occurs within Marine Isotope Stage (MIS) 19, an interglacial, spanning the boundary between the Matuyama and Brunhes magnetochrons (Head and Gibbard 2015b). The Chiba composite section, deposited on the continental slope along the Pacific margin of the Japanese archipelago, contains continuous and highly-resolved marine records that capture changes in both terrestrial and marine paleoenvironments with well-developed chronological control. Its geographic location (Fig. 1) and excellent exposure provide a rare opportunity to study and construct links at high resolution between atmospheric and oceanic circulation, terrestrial environmental changes, and evolution of the biota, thereby providing an improved understanding of the Earth's climate system, particularly across the Early–Middle Pleistocene boundary (Kazaoka et al., 2015; Suganuma et al., 2018).

The Chiba composite section, placed within in the Kokumoto Formation, Kazusa Group, contains undisturbed sediments of Early and Middle Pleistocene age yielding well-preserved microfossils and geochemical signatures, and bears the Matuyama–Brunhes (M–B) paleomagnetic Chron boundary with widespread tephra beds including the Ontake-Byakubi-E (Byk-E) tephra bed which occurs just 1.1 m below the M–B paleomagnetic boundary (Kazaoka et al., 2015; Suganuma et al., 2015, 2018; Hyodo et al., 2016; Nishida et al., 2016; Takeshita et al., 2016; Okada et al., 2017). Recent studies of this composite section have

mostly focused on the Early–Middle Pleistocene boundary, the M–B polarity reversal and the widespread tephra beds occurring within the section (Suganuma et al., 2018 and references therein). These studies have been conducted in the context of preparing the Chiba composite section as a candidate for the Middle Pleistocene GSSP. Significantly, the M–B paleomagnetic Chron boundary had already been chosen to serve as the primary chronostratigraphic guide for the Early–Middle Pleistocene boundary. This decision had been made by the Early–Middle Pleistocene Boundary Working Group, a constituent body of the Subcommission on Quaternary Stratigraphy, itself a constituent subcommission of the International Commission on Stratigraphy, in 2004 (Head et al., 2008). That decision follows long tradition, mostly because it represents a brief and synchronous event and can be observed both in marine and terrestrial records (Richmond, 1996; Pillans, 2003; Head and Gibbard 2005, 2015a; Head et al., 2008). Any GSSP must also involve multiple criteria around the primary guide (in this case the M–B paleomagnetic boundary) in order to achieve the best possible opportunities for correlation with other sections in various depositional settings (Remane et al., 1996). The M–B paleomagnetic boundary has an age of ~773 ka, within MIS 19 (Channell et al., 2004; Head and Gibbard 2005; Head and Gibbard 2015b; Suganuma et al., 2018). The Early–Middle Pleistocene boundary occurs at the approximate midpoint of the Early–Middle Pleistocene transition, an interval marked by a fundamental reorganization of the Earth's climate system with records of this transition occurring in both marine and terrestrial realms (Head and Gibbard 2015b and references therein). The interval representing interglacial MIS 19 and its transition from glacial MIS 20 is the focus of this study. MIS 19 is known to be the closest analogue for the present interglacial in terms of its astronomical signature, particularly the phasing of obliquity and precession, and similar paleoclimate signal (Pol et al., 2010; Tzedakis, 2010; Tzedakis et al., 2012). However, differences in high-frequency oscillations between MIS 1 (2500 years) and MIS 19 (5000

years) reported from the eastern North Atlantic (Sánchez Goñi et al., 2016) and differences in the vegetational development on the Iberian Peninsula (Oliveira et al., 2017) suggest that similarities under natural boundary conditions are not as great as previously thought.

Numerous studies have been conducted on the Chiba composite section relating to biostratigraphy, oxygen isotope stratigraphy, magnetostratigraphy and tephrostratigraphy (see Suganuma et al., 2018 and references therein). No study, however, has been undertaken on dinoflagellate cysts from the Chiba composite section. Hence, this study aims to investigate the occurrence of dinoflagellate cyst assemblages in the Chiba composite section and their responses to paleoceanographic changes across the Early–Middle Pleistocene boundary in the western Pacific Ocean from late MIS 20 to late MIS 19 (~791–768 ka), in particular Termination IX which represents the MIS 20–19 boundary.

1.2 Purpose of study

This study aims to:

1. use dinoflagellate cyst assemblages from the Chiba composite section to unravel paleoceanographic changes across the Early–Middle Pleistocene boundary during MIS 19;
2. compare dinoflagellate cyst assemblage changes with the benthic foraminiferal oxygen isotope record and other records from the same section to examine any leads or lags in their response to paleoclimatic changes, particularly across Termination IX;
3. characterize and evaluate the timing of full interglacial conditions for MIS 19, given the status of MIS 19 as the closest analogue for the present interglacial, in order to provide a hypothetical timing for the onset of the next glaciation;
4. elucidate the structure and climatic development during and just prior to MIS 19, both in the terrestrial and marine realms, using dinoflagellate cyst assemblage composition

data, in order to enhance our understanding of climate dynamics and taphonomy during the Early Pleistocene;

5. estimate sea-surface parameters such as sea-surface temperature (SST) and sea-surface salinity (SSS) during MIS 19 in the Western Pacific Ocean using transfer functions derived from a modern Northern Hemisphere dinoflagellate cyst dataset.

CHAPTER TWO

2.0 THE STUDY LOCATION

2.1 The Chiba composite section

The Chiba composite section lies at the intersection between the easternmost margin of the Eurasian Continent and the Pacific Ocean (Fig. 1). Its marine sedimentary record preserves the interplay of terrestrial and marine climatic and environmental changes, most notably the interaction between the westerly jet, East Asian monsoon and the North Pacific Gyre (subtropical and subpolar) (Suganuma et al., 2018) (Fig. 1a). The geographic location of the Japanese archipelago provides an extraordinary opportunity for various kinds of paleoclimatic and paleoceanographic studies, which indeed has produced numerous geological data. The Chiba composite section extends from MIS 20 to early MIS 18 and hence spans the M–B boundary which serves as the primary guide for the Early–Middle Pleistocene boundary and occurs within MIS 19 (Head et al., 2008; Kazaoka et al., 2015). The paleoclimatic and paleoceaographic history of the Chiba composite section has been captured in detail using a wide variety of terrestrial and marine proxies (Suganuma et al., 2018).

The Chiba composite section consist of the Chiba section, which outcrops along the Yoro River (35°17.41'N; 140°8.48'E) (Fig. 2) and forms part of the Yoro River section, the Yoro–Tabuchi section (35°17.41'N; 140°8.49'E) in the village of Tabuchi, the Yanagawa section along the Yana River (35˚17.15'N; 140˚7.88'E) in the vilage of Yanagawa, and the Kokusabata section along the Kokusabata River (35˚18.52'N; 140˚11.89'E) in the village of Kokusabata (Fig. 4). Occurring within the Kokumoto Formation and exposed along deeply incised river valleys, these sections are adjacent and continuous across the Early–Middle Pleistocene boundary interval (Kazaoka et al., 2015; Suganuma et al., 2018).

2.1.1 The Chiba section

The Chiba section, previously called the Tabuchi section (e.g. Kazaoka et al., 2015; Nishida et al., 2016), is the proposed location of the GSSP and also the focus of this study. It occurs geographically in the middle of the other sections that comprise the Chiba composite section, is easy to access, and outcrops along the Yoro River valley in the village of Tabuchi where the river-cut exposures are spectacular (Fig. 2). Sedimentation here is continuous across the Early–Middle Pleistocene boundary, and the occurrence of the Byk-E and Ku2 tephra beds just above the boundary allows precise correlation with the other sections. The Byk-E tephra has been proposed as the level of the GSSP at the Chiba section (Suganuma et al., 2018; Fig. 2, 4 and 5) and has a U-Pb zircon age of 772.7 ± 7.2 ka (Suganuma et al., 2015). The Chiba section mainly consists of a thick siltstone unit with intercalations of thinly bedded sand, coarse silts, shell fragments and thin tephra beds including several volcanic scoria and pumice horizons (Kazaoka et al., 2015; Fig. 11). The section is well known to be a stable depositional unit and lacks slump structures or unconformable boundaries within this interval. However, the silty beds are significantly bioturbated (Nishida et al., 2016). Nishida et al. (2016) noted that the groove casts occurring within the section reveal an orientation of 66°NE and 80°NE for the paleocurrent directions (Fig. 7 and 9), which is consistent with the general paleocurrent directions (east to northeast) for the Kazusa Group in general (Ito et al., 2016).

2.2 Modern oceanographic setting of the Western Pacific Ocean and climate of the Japanese archipelago

The land–ocean exchanges over the Japanese archipelago, which includes the Boso Peninsula, are presently under the influence of the subtropical Kuroshio Current, the subarctic Oyashio Current, and warm Tsushima Current (Fig. 1b) (Suganuma et al., 2018). The

Oyashio Current descends beneath the Kuroshio Current (Fig. 1a and b) and both form the Subarctic Front in the northwestern Pacific Ocean. A pronounced latitudinal sea-surface temperature (SST) gradient which is greatest off the Boso Peninsula is created by the mixing of these two currents (Suganuma et al., 2017). Paleoceanographic records capturing the interplay between these two currents are well preserved in the Kazusa Group, which was open to the Pacific during the Pleistocene. The Kuroshio Current (western boundary of the Subtropical Gyre) carries warm waters from the tropics and supplies heat to the Japanese Island. It flows along the eastern margin of the Japanese archipelago and turns eastward just after the Boso Peninsula before reaching the Subarctic Front, forming the Kuroshio Extension Current (northern boundary of the Subtropical Gyre). The Tsushima Current branches off from the Kuroshio Current in the south of the Japanese archipelago and flows northwest along the western margin of the island into the Sea of Japan (Suganuma et al., 2018). The Oyashio Current, which occupies the northwest Pacific Ocean, carries cold waters from the Okhotsk Sea and turns eastwards becoming the Subarctic Current flowing along the Subarctic Front (Favorite et al., 1976). The annual mean SST of the Kuroshio Current off central Japan is approximately 20–22°C whereas that of the Oyashio Current off the northern part of Japanese islands is approximately 4–8°C. Furthermore, a sea-surface salinity gradient is observed between the Oyashio- (ca. 33.0 psu) and Kuroshio-influenced regions (ca. 34.5 psu). It is noteworthy that the Kuroshio Current is oligotrophic, whereas the Oyashio Current is nutrient-rich. The interplay between these two current systems accordingly has a strong impact on the marine biota (Suganuma et al., 2018). In the Kanto Basin, which includes the central part of the Boso Peninsula, the present-day natural vegetation is mainly warm-temperate broadleaved evergreen forest. The northern and surrounding higher-relief ranges of the Kanto Basin consist of cool-temperate deciduous broadleaved and coniferous forests (Yoshioka, 1973).

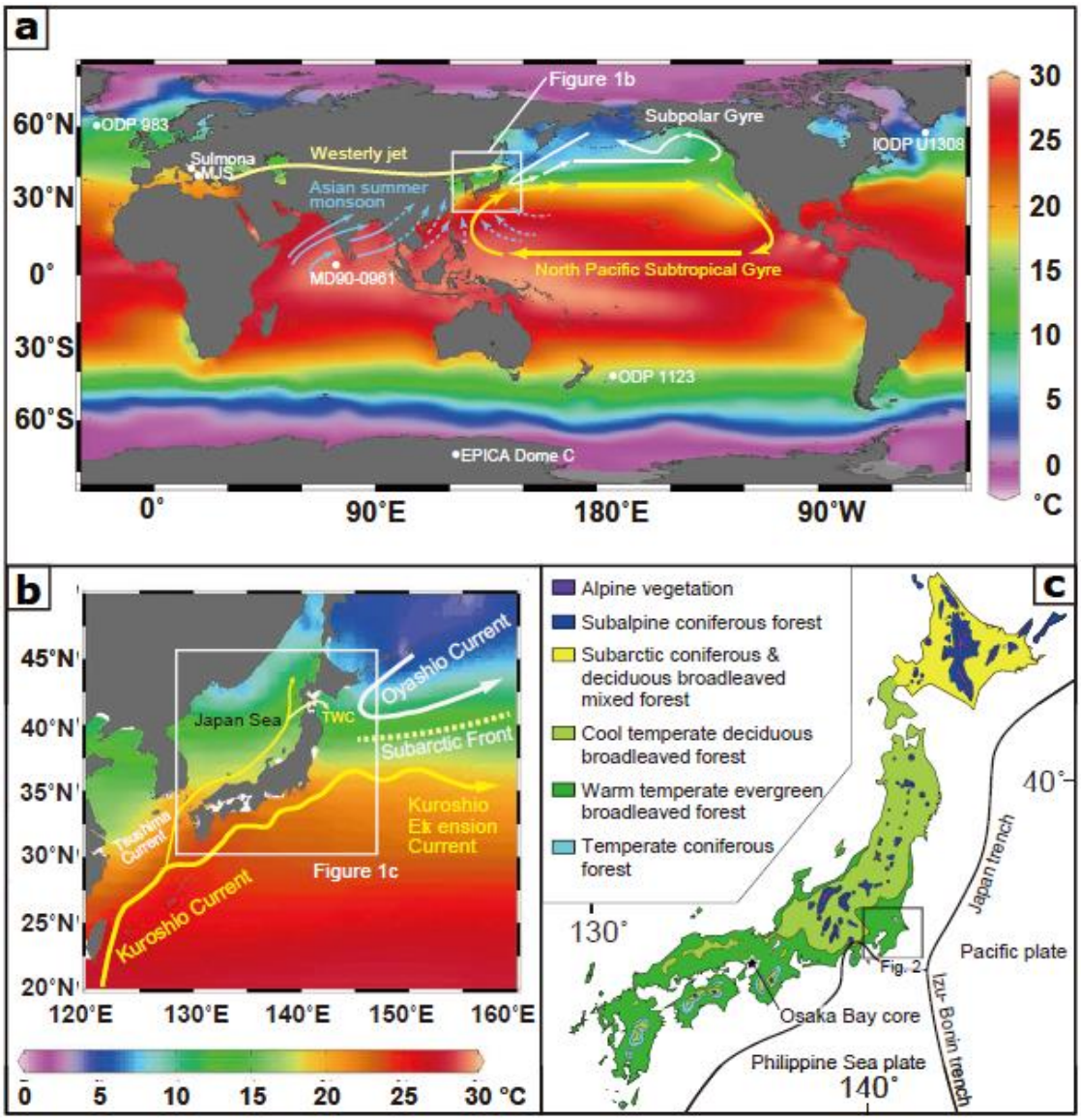

Fig. 1: Location and geographic setting of the Chiba composite section, central Boso Peninsula, Japan. (a) and (b) oceanographic and atmospheric circulation patterns around the Japanese island in summer. TWC = Tsugaru Warm Current. (c) vegetation map of the Japanese islands with mini box indicating the position of the Boso Peninsula, Chiba Prefecture (Source: Suganuma et al., 2018).

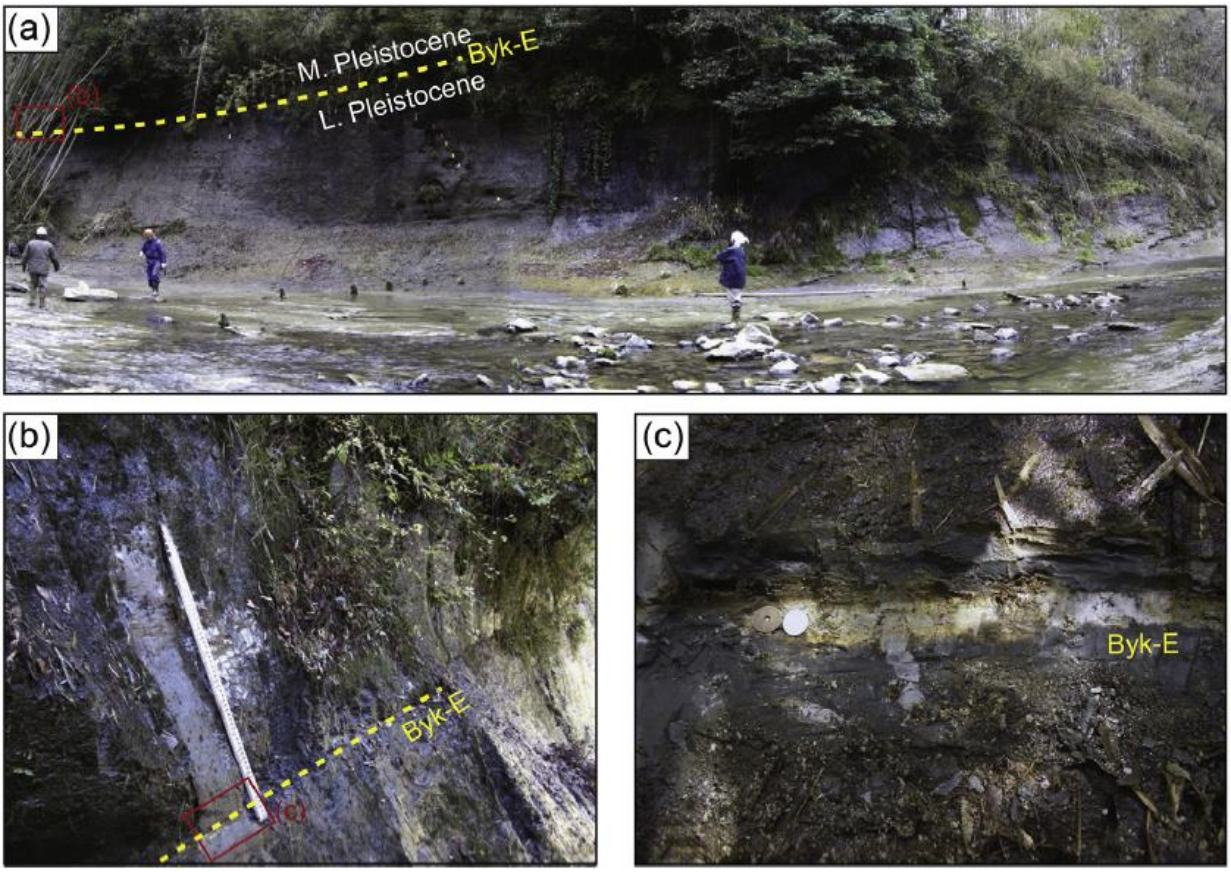

Fig. 2: Sedimentary succession across the Early–Middle Pleistocene boundary in the Chiba section (previously known as the Tabuchi section). (a) Overview of the Chiba section with yellow broken line indicating the boundary which has been placed at the base of the Ontake-Byakubi-E (Byk-E) tephra. (b) and (c) show detail of the Byk-E tephra. The length of rule (b) and diameter of the coin (c) are 1.25 m and 2.0 cm respectively (From Kazaoka et al., 2015, fig. 12).

CHAPTER THREE

3.0 LITERATURE REVIEW

3.1 Kanto Tectonic Basin

The Kanto Tectonic Basin is a forearc basin fill that developed as a result of the west-north-westward subduction of the Pacific and Philippine plates beneath the Eurasian plate along the Japan and Izu-Bonin trenches (e.g., Seno and Takano, 1989) (see also Fig. 1c). It now forms the largest lowland (the Kanto Plain) in the Japanese archipelago, and is situated on the boundary of the Northeast and Southwest Japan arc on the Eurasian (EUR) plate. The Kanto Tectonic Basin has been active since the Middle Miocene (Hashima et al., 2016) when backarc spreading caused the Sea of Japan to open leading to the separation of Japan from the Eurasian continent (e.g., Otofuji et al., 1985; Baba et al., 2007). Evidence of subsidence from this time exists in the forearc basin because of the infilling of the Kanto plain with thick sedimentary sequences of about 3000 m (Suzuki et al., 2011) (Fig. 3 below). Most of the Kanto basin subsided except the southeast coast and the western mountainous areas (Hashima et al., 2016). Subsidence ended and uplift began in the southeastern part of the Kanto Tectonic Basin from the Middle to Late Pleistocene under the influence of glacio-eustacy (Kaizuka, 1987). Due to uplift in the southeastern margin of the Kanto Tectonic basin, the marine strata dip gently northwestward and are well exposed on land, particularly in the central Boso peninsula, which provides a rare opportunity to study an Early to Middle Pleistocene sedimentary succession on land (Kazaoka et al., 2015; Okada et al., 2017).

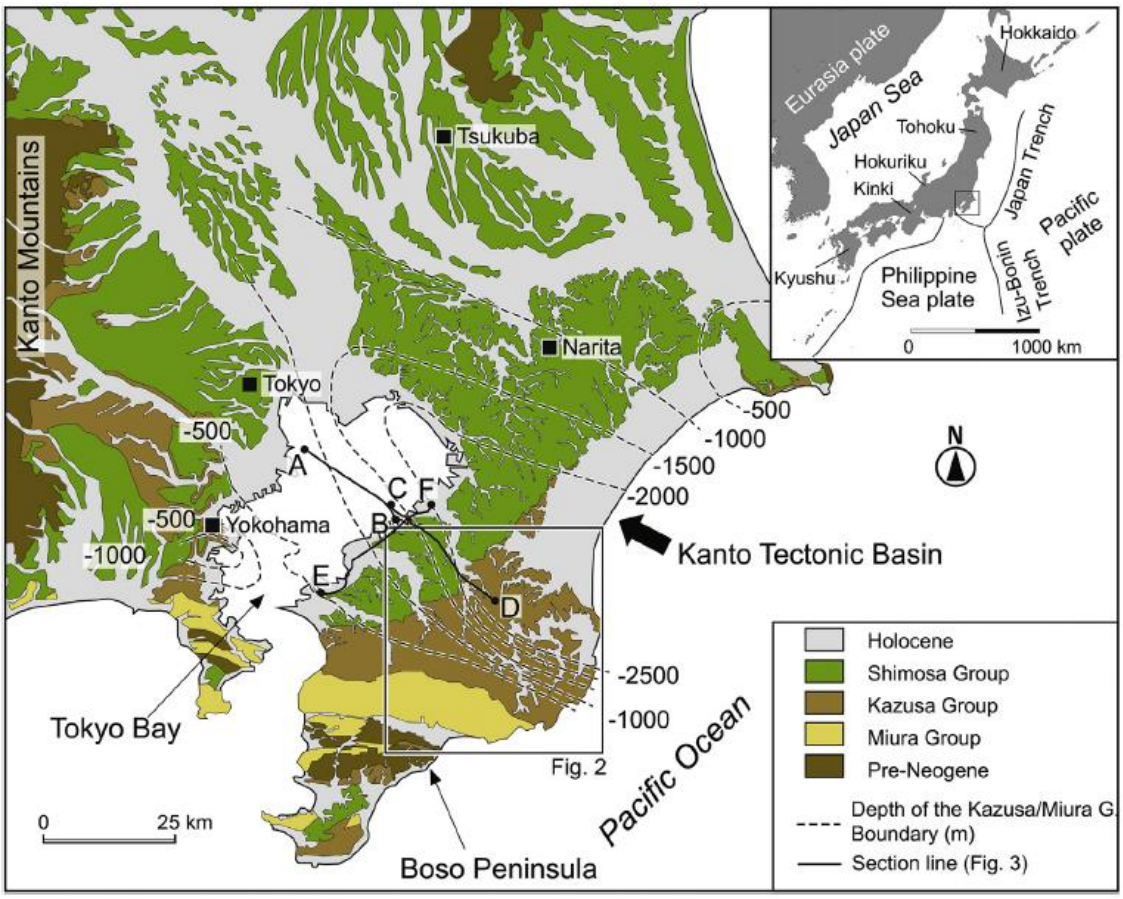

Fig. 3: Schematic map of the Kanto tectonic basin. Inset map shows the location of the study area (Kazaoka et al., 2015).

3.2 Kazusa Group and Kokumoto Formation

The Kazusa Group contains a remarkably continuous succession (Figs. 2, 4 and 5). It is mainly exposed in the middle part of the Boso Peninsula and several hills fringing the Kanto Mountains, these hilly areas being separated by Tokyo Bay (Fig. 3) (Suzuki et al., 2011). The Kazusa Group unconformably overlies the Miocene–Pliocene Miura Group, and is unconformably overlain by the Shimosa Group which was deposited during the Middle and Late Pleistocene (~0.45–0.12 Ma) and consists of shallow marine to paralic sediments (Ito, 1998; Kazaoka et al., 2015). The Kazusa Group is Early and Middle Pleistocene in age, extending from 2.4 Ma to 0.5 Ma (Kazaoka et al., 2015). The lithology predominantly

comprises sandstones and siltstones deposited in marine environments of the deep-sea basin plain, submarine-fans, continental slope, and shallow seas (Katsura, 1984; Ito and Katsura, 1992) that collectively show an upward–shallowing succession (e.g., Oyama, 1959; Kazaoka et al., 2015). The maximum thickness of this Lower and Middle Pleistocene sedimentary succession is approximately 3000 m, one of the thickest in the Japanese archipelago (e.g., Mitsunashi et al., 1959; Ito, 1998b) and well exposed along the Yoro River where numerous studies ranging from lithostratigraphy, biostratigraphy, paleomagnetic to oxygen isotope stratigraphy have been conducted. The Kazusa Group thickens from SW to NE with the deepest sedimentary succession occurring toward the NE, and it dips gently to the northwest (Fig. 2) with the angle of dip decreasing gradually from 20 degrees in the lower part of the group to several degrees in its upper part (Kazaoka et al., 2015). The Kazusa Group consists of 14 formations (Figs. 4 and 5) in the central and eastern parts of the Boso Peninsula (Mitsunashi, 1980; Tokuhashi and Endo, 1984; Kazaoka et al., 2015).

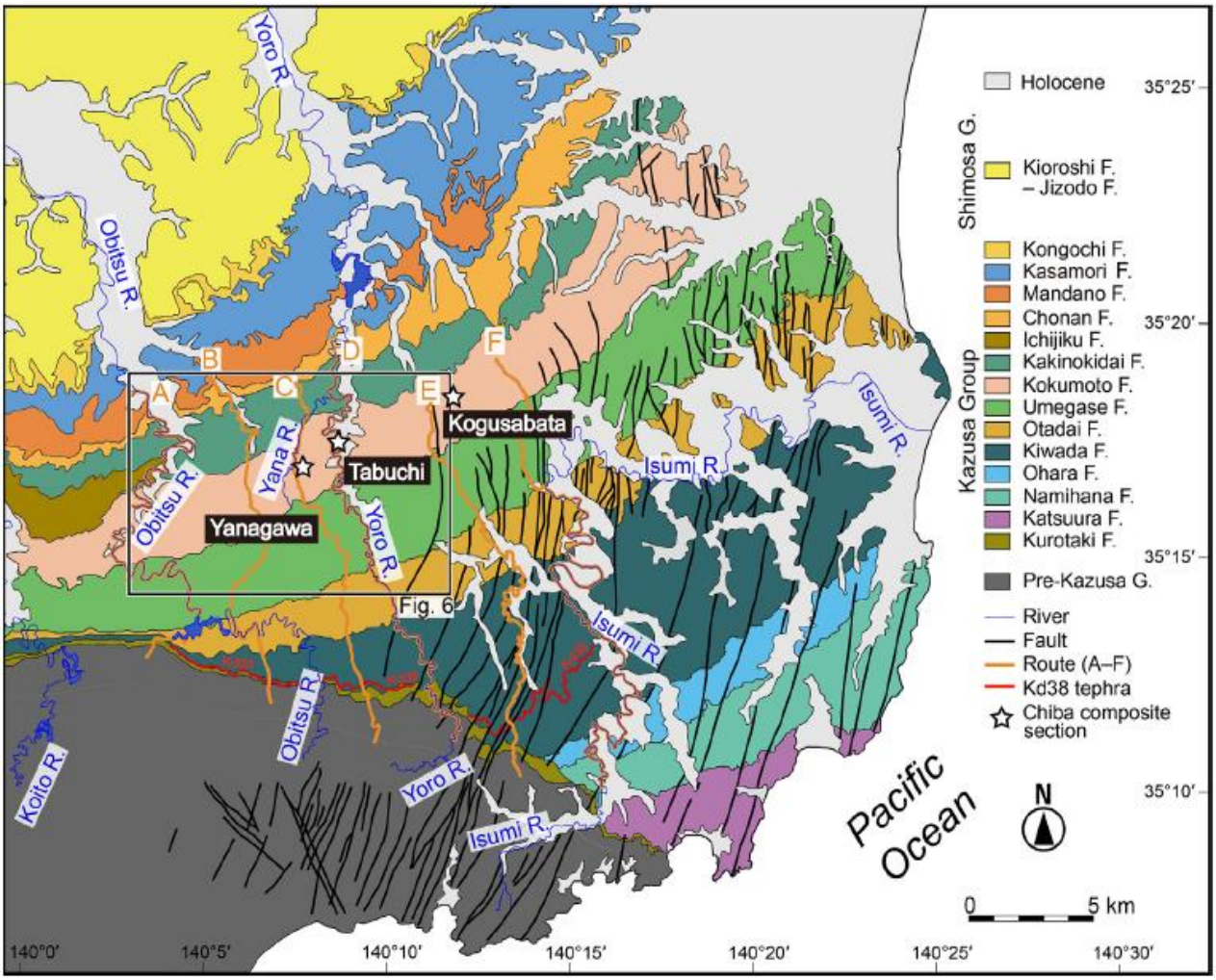

Fig. 4: Simplified geologic map of the Boso Peninsula. A–F (A: Obitsu River route, B: Kase route, C: Tsutsumori route, D: Yoro River route, E: Kamishiki route, F: Otaki route) correspond to the routes used to create the sections comprising the lithostratigraphic profile in Fig. 5 by Kazaoka et al. (2015). The box and stars indicate the Chiba composite section including the Yanagawa, Tabuchi (now Chiba), and Kogusabata sections. The Chiba section is exposed along the Yoro River (Source: Kazaoka et al., 2015).

The Kokumoto Formation occurs in the upper part of the Kazusa Group and crops out in the central Boso Peninsula. It is well exposed along the Yoro River where its thickness is approximately 350 m, although this varies between 350 and 400 m throughout the Chiba composite section (Kazaoka et al., 2015). The Kokumoto Formation spans the Early–Middle Pleistocene boundary, and represents especially at the Chiba composite section an expanded and well-exposed sedimentary succession. The formation consists of continental shelf edge to

continental slope deposits (Katsura, 1984; Ito, 1992; Ito and Katsura, 1992; Nakamura et al., 2007) intercalated with numerous tephras including the Byk-E tephra (Hyodo et al., 2016). It comprises large-scale alternations of sandstones and sandy siltstones that are laterally continuous, although in the western part, some of the sandy siltstones in the upper part of the formation grade into sandstone (Fig. 5) (Kazaoka et al., 2015). A review by Kazaoka et al. (2015) shows sandstone beds that are up to ~110 m thick, comprise fine to medium sand, and are massive or contain large-scale cross bedding. However, alternations of sand and siltstone layers which are about 5 m thick each, are embedded within these sandstone beds. Also, approximately 90-m thick alternations of sands and sandy siltstones occur at the bottom and in the upper half of the formation and bear fine to very fine grained thin (~5 cm) sandstone beds every 0.3–1.0 m (Kazaoka et al., 2015; Fig. 4). The topmost siltstone sequence 70–80 m thick is correlated with MIS 19 (Hyodo et al., 2016). Marine oxygen isotope studies reveal a continuous record from MIS 21 to MIS 18, and probably up to MIS 15, with glacial–interglacial cycles corresponding to sandstones and siltstone-dominated sections respectively (e.g. Okada and Niitsuma, 1989; Pickering et al., 1999).

Numerous tephra beds occur within the Kokumoto Formation along the Yoro River (Figs. 5 and 7) (Mitsunashi et al., 1959, 1961) and facilitate high-resolution correlation within the succesion. The Kokumoto Formation has high sedimentation rates, estimated to be 2–3 m/ky (Okada and Niitsuma, 1989), and has accordingly produced a large number of highly resolved datasets.

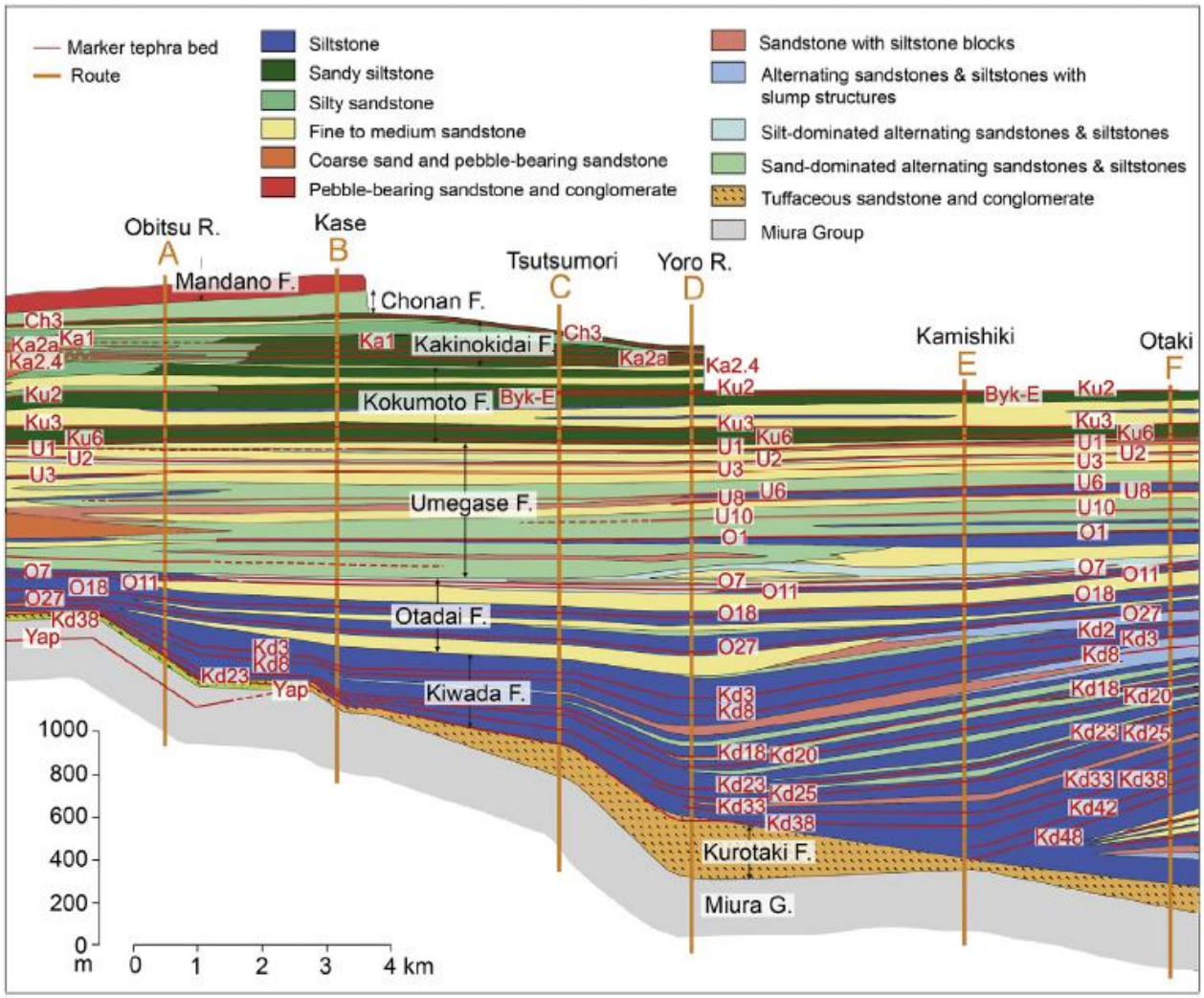

Fig. 5: Lithostratigraphic profile of the Kazusa Group showing all formations, including the Kokumoto Formation occurring near the top. A–F indicates geological routes as shown in Fig. 4 above (Source: Kazaoka et al., 2015).

3.3 Sedimentary processes of the Chiba section

The Chiba section, previously known as the Tabuchi section (vide supra) has been studied in detail because it is the site of the proposed GSSP. It forms part of the Yoro River section (Suganuma et al., 2018). It predominantly consists of silty beds that straddle the Matuyama–Brunhes boundary with minor sand beds intercalated within the silty succession, particularly in the lower part of the section (Fig. 6) (Kazoaka et al., 2015). The silty beds are

characterized by homogeneous mottled facies caused by intense bioturbation. These silty beds of the Kokumoto Formation show no evidence of unconformities and are interpreted to be hemipelagites formed by the deposition of fine-grained suspended material under quiescent bottom-water conditions. Field and laboratory evidence of intense bioturbation strongly suggest slow and continuous deposition (Nishida et al., 2016; Hyodo et al., 2016). The thickness of the silty beds is about 10–380 cm with median grain size of 10.8–15.4 μm and there is no distinctive vertical change of lithofacies, although the coarser fraction increases slightly upsection (Nishida et al., 2016). In addition to the distinct tephra layers occurring within the Chiba section, scattered pumice and scoria clasts are also present, especially in the upper part of the section (Fig. 6) (Kazaoka et al., 2015).

The sandy beds, although minor, are intercalated in some horizons in the Chiba section with the silty succession discussed above, particularly in the lower part of the Chiba section (Nishida et al., 2016). Nishida et al. (2016) classified the sandy beds into two types (type A and B) based on their thickness and internal structures. The type A sandy beds suggest turbidity and are 1–40 cm thick. They are characterized by upward fining, from fine to coarse sand at the base to sandy silt to very fine sand at the top, have faint planar laminations, cross-bedding in the lower coarser part, ripple cross-laminations in the upper finer part, mud clasts, small shell fragments at the base of some sandy beds, and an erosional basal contact of the sandy beds. Type B sandy beds are typical of debrites, 50–70 cm thick and characterized by very fine sand to fine sand, with abundant mud clasts in a poorly sorted sand matrix, a sharp base, and an irregular upper surface with the frequency and thickness of the sandy beds decreasing up-section (Nishida et al., 2016; Hyodo et al., 2016).

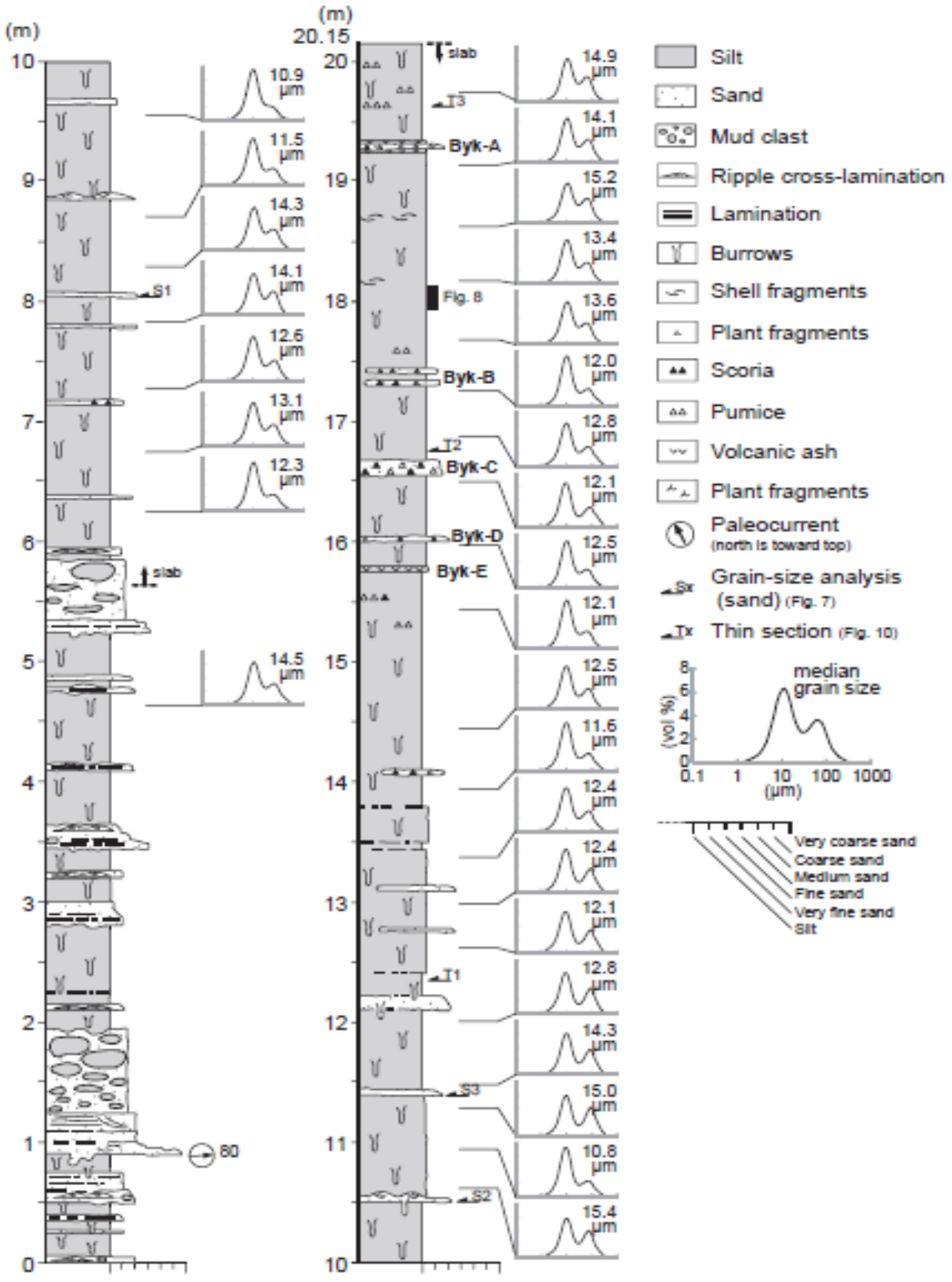

Fig. 6. Detailed stratigraphic log and grain-sizes of silty beds in the Chiba section (Nishida et al., 2016, fig. 6).

3.4 Depositional environment of the Chiba composite section

The depositional environment of the Chiba composite section is mostly shelf edge to continental slope (Ito, 1992; Ito and Katsura, 1992; Ito et al., 2006a,b; Nakamura et al., 2007). The lower part of the succession mainly represents deep-sea basin plain and submarine fan deposits, whereas the upper part consists mainly of submarine fan and slope deposits associated with minor shelf and nearshore deposits (Kazaoka et al., 2015). Nishida et al. (2016) interpreted the sedimentary environment of the Chiba composite section as continental slope due to similarities between the trace fossil associations of the Chiba section and those of Pleistocene sediments from IODP Site U1385 (the Shackleton Site) on the continental slope of the southwestern Iberian margin (Hodell et al., 2013; Rodríguez-Tovar and Dorador, 2014). High-frequency fluctuations of glacio-eustatic sea level seen in the vertical changes in the frequency and thickness of sandy beds within the silty succession suggest that the upper part of the Chiba composite section in the interval of the Matuyama–Brunhes paleomagnetic reversal was deposited in calmer, more stable conditions than the remainder of the section (Nishida et al., 2016). Similarly, Hyodo et al. (2016) also noted that the sediments in the Chiba composite section were deposited in calm environments, with the exception of the lowermost part of the section. Bathyal species of benthic foraminiferal assemblages recovered by Kamemaru (1996) from the Chiba section, including *Bulimina aculeata*, *Melonis parkerae* and *Bolivinita quadrilateral*, indicate that the sediments were deposited at a water depth of more than 200 m. Also, based on pelagic gastropod assemblages, the thick siltstones in the Chiba composite section are interpreted to have been deposited in warm oceanic conditions (Ujihira, 1986).

3.5 Matuyama–Brunhes polarity boundary

Numerous studies from the Chiba composite section have identified the Matuyama–Brunhes polarity boundary in the middle of the section, close to the rhyolitic Byk-E tephra bed (Fig. 7) (Niitsuma, 1976; Okada and Niitsuma, 1989; Aida, 1997; Tsunakawa et al., 1999; Suganuma et al., 2015). Okada et al. (2017) presented a detailed virtual geomagnetic pole (VGP) path from the Chiba section at a 10-cm sampling resolution that places the directional midpoint of the M–B boundary at 1.1 m above the Byk-E tephra, with the interval between 0.25 m and 1.95 m as the directional transition zone of the M–B boundary. Based on the latest benthic foraminiferal oxygen isotope stratigraphy for the Chiba composite section, the astronomical age of the M–B boundary in this section is 772.9 ka (directional midpoint) and the estimated duration of the transition is ~1.9 kyr (Suganuma et al., 2018).

3.6 Oxygen isotope stratigraphy

Okada and Niitsuma (1989) established an oxygen isotope stratigraphy for the Kazusa Group including the Chiba composite section (Fig. 7), assigning these deposits to MIS 35–15 with the M–B boundary correlated with MIS 19. Refinements by Pickering et al. (1999) using graphical correlation along with new astronomically tuned isotope records gave a revised range of MIS 33–16, with sub-stages in MIS 21–16 being identified. Both studies found the Chiba composite section to have a continuous record from MIS 21 through MIS 18 and noted that the glacial–interglacial cycles correspond to sandstone and siltstone dominated units, respectively (Fig. 7). A subsequent high-resolution benthic foraminiferal oxygen isotope stratigraphy assigns the Chiba composite section a late MIS 20 to early MIS 18 range, with the M–B boundary occurring in the middle of MIS 19 (Fig. 7) (Suganuma et al., 2015). The most recent oxygen isotope stratigraphy for the Chiba composite section developed by Suganuma et al. (2018) (Fig. 8) shows well defined glacial–interglacial cycles from late MIS 20 to early MIS 18, with multi-millennial- to millennial-scale changes both in Termination IX and the later part of MIS 19.

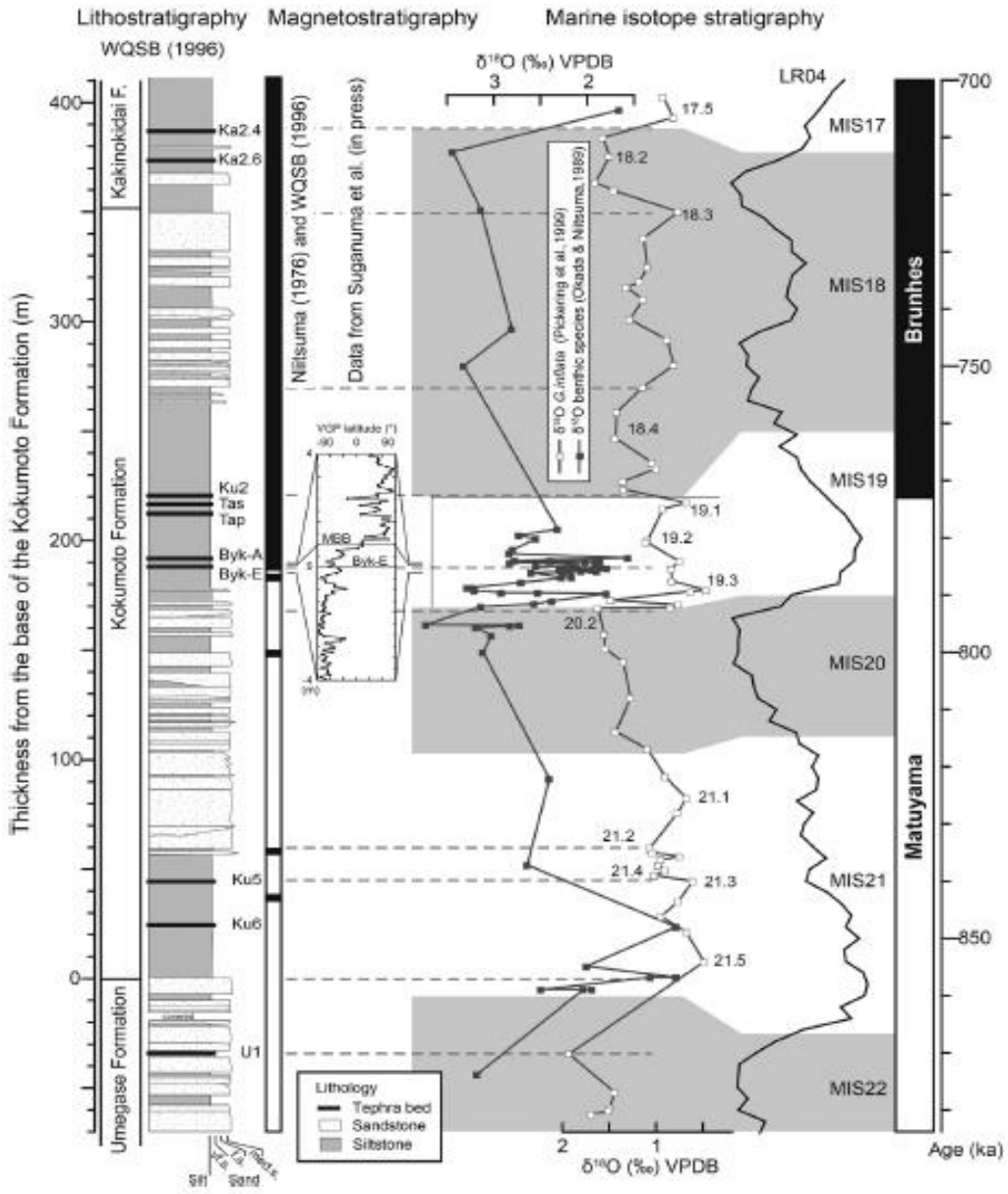

Fig. 7: The Kokumoto Formation showing magnetostratigraphy with the position of the M–B polarity boundary (Suganuma et al., 2015), oxygen isotope stratigraphy (Okada and Niistuma, 1989; Pickering et al., 1999), tephrostratigraphy, all correlated to the LR04 benthic stack (Lisiecki and Raymo, 2005). Well defined glacial–interglacial stages with identified substages by Pickering et al. (1999) are shown on the isotope curve.

3.7 Ontake–Byakubi (Byk-E) Tephra bed

The Kokumoto Formation contains widespread tephra beds (Fig. 6) that have been described and mapped in detail and serve to facilitate detailed correlation of sedimentary successions within the region (Okada and Nitsuma 1989; Kazaoka et al., 2015; Suganuma et al., 2015;

Nishida et al., 2016). They are well recognized along the Yoro River section and consist of rhyolitic volcanic ash beds with sharp bases, and normal and bioturbated tops (Kazaoka et al., 2015).

The Byakubi-E (Byk-E) tephra, now known as the Ontake–Byakubi tephra (Takeshita et al., 2016), is of particular interest as it occurs approximately 1.1 m below the M–B boundary which is the primary guide for the Early–Middle Pleistocene Boundary. It therefore serves as a regional stratigraphic marker bed for the Early–Middle Pleistocene boundary, and it is at this level in the Chiba section that the GSSP is being proposed (Kazaoka et al., 2015; Suganuma et al., 2015, 2018). The Byk-E bed is approximately 1–3 cm thick, sandwiched between layers of thick and massive dark gray sandy siltstone, and consists of fine white volcanic glass shards of pumice-type, and mafic minerals including hornblende, orthopyroxene, clinopyroxene and garnet (Takeshita et al., 2016; Nishida et al., 2016). Suganuma et al. (2015) dated the Byk-E tephra and presented a U-Pb zircon age of 772.7 ± 7.2 ka.

3.8 Biostratigraphy of the Chiba composite section

Several biostratigraphic studies conducted on the Chiba composite section provide temporal constraints. Igarashi (1996) assigned the Kokumoto Formation to planktonic foraminiferal Zone N22 of Blow (1969) based on the co-occurrences of *Globorotalia truncatulinoides* and *Globorotalia tosaensis*. The highest occurrence (HO) of *Neogloboquadrina inglei* was recorded just below the upper boundary of the Kokumoto Formation (Suganuma et al., 2017) and is estimated to be 732 ka in age based on the correlation with $\delta^{18}O$ stratigraphy of Pickering et al. (1999) in the Chiba composite section. This age is supported by the independently dated HO of *N. inglei* at 0.73 Ma for ODP Site 1150 in the Northwest Pacific Ocean (Domitsu and Oda, 2008). Cherepanova et al. (2002) identified the highest occurrence

(HO) of the diatom *Nitzschia fossilis* in the upper part of the Kokumoto Formation in the Chiba composite section and noted that the age of this datum, at 0.59 Ma, is the same in the land-based Choshi section, as well as at DSDP Sites 578, 579 and 580. This diatom datum is traceable from the subtropical to subarctic regions in the Pacific (Suganuma et al., 2018). Although no calcareous nannofossil biohorizons have been detected in the Chiba composite section, Suganuma et al. (2018) noted a likely correspondence between the increase of larger forms of *Gephyrocapsa* (larger than 4 μm) that began after late MIS 20 and the lowest occurrence of the larger form (late interval; ~0.7 – 0.5 Ma) of *Gephyrocapsa* sp. C recorded by Matsuoka and Okada (1990) in ODP Hole 709C located in the western tropical Indian Ocean. This temporal datum helps constrain the age of the Chiba composite section. In addition, and from a broader context, Sato et al. (1988) placed the Kokumoto Formation between the last appearance datum (LAD) of the calcareous nannofossil *Reticulofenestra asanoi* (0.889 ± 0.25 Ma in the Ontong Java Plateau; Berger et al., 1994) and LAD of *Pseudoemiliania lacunosa* (0.433 ± 0.20 Ma in the Ontong Java Plateau; Berger et al., 1994). This serves as the primary evidence for the age range of the Kokumoto Formation to which the Chiba composite section belongs.

3.9 Paleoenvironmental reconstructions of the Chiba Composite section

Detailed paleoenvironmental reconstructions of the Chiba composite section from late MIS 20 to early MIS 18, particularly across the M–B boundary, show significant marine and terrestrial paleoenvironmental changes. Analysis of planktonic foraminiferal assemblages from the Chiba composite section by Igarashi (1994) shows clear changes in past sea-surface currents during this time. The estimation based on the principal component analysis of these assemblages shows the oscillatory influence of major surface currents, notably the Kuroshio, Oyashio, and Tsugaru, in the region during the deposition of the Kazusa Group. The study also shows that the Subarctic Front between the subtropical Kuroshio and subarctic Oyashio

currents shifted northward just after the M–B boundary. Results obtained from the study of radiolarian assemblages on the Chiba composite section show that MIS 19 is characterized by warm water species such as *Dictyocoryne* spp., *Didymocyrtis* spp. and *Tetrapyle* spp. High abundances of these species presently occur in the Kuroshio Current where sea-surface temperatures range between 20° and 29°C (Suganuma et al., 2017). In addition, a pollen record provided by Suganuma et al. (2018) on the Chiba composite section from late MIS 20 to early MIS 18 shows strong variation in the occurrence of *Pinus*, *Picea*, *Tsuga*, and Taxodiaceae (*Metasequoia*, *Cryptomeria*), with dominance of deciduous broad-leaved trees in MIS 19. The high abundance of bisaccate pollen (e.g. pine) shows long-distance transport from the coast and hence distal sedimentation in the area, whereas *Metasequoia*, a component of the northern hemisphere flora from the Late Cretaceous to Quaternary, disappears in the middle of the Kokumoto Formation (Onishi, 1969) presumably in response to a deteriorating climate. Kamemaru (1996) and Suganuma et al. (2017) noted that the benthic foraminifera of the Chiba composite section are characterized by dominant bathyal and rare sublittoral species.

The silty beds of the Chiba composite section are characterized by homogeneous mottled facies caused by intense bioturbation. Field and laboratory studies of this bioturbation strongly suggest slow and continuous deposition (Nishida et al., 2016; Hyodo et al., 2016). Trace fossil assemblages are diverse and typical of the *Zoophycos* ichnofacies in the silty beds of the Chiba composite section. Nishida et al. (2016) identified several ichnogenera using X-ray CT-scanned images of the silty beds and these are similar to those identified by Hyodo et al. (2016). The ichnogenera recognized are *Alcyonidiopsis*, *Chondrites*, *Nereites*, *Palaeophycus*, *Phycosiphon*, *Planolites*, *Scolicia*, *Skolithos*, *Teichichnus*, *Thalassinoides*, *Trichichnus*, and *Zoophycos* and an indeterminate U-shaped burrow. Brief descriptions and photographs of these ichnogenera can be found in Nishida et al. (2016; Fig. 10). The presence

of the *Zoophycos* ichnofacies, a trace fossil not usually found in shallow settings (Löwemark and Werner, 2001), shows that the Chiba composite section is typical of a continental slope environment. Indeed, the trace fossil association of the Chiba section is similar to that of Pleistocene sediments collected at IODP Site U1385 (the Shackleton Site) on the continental slope of the southwestern Iberian margin (Hodell et al., 2013; Rodríguez-Tovar and Dorador, 2014), as mentioned above.

3.10 Application of dinoflagellate cysts in paleoceanography

Wall et al. (1977) documented the modern distributions of dinoflagellate cyst species in a range of environments in the North and South Atlantic and found that they could be classified according to a range of climatic parameters, including temperate, subtropical, and tropical regimes, and environmental parameters. Hence, relative abundance and species compositions of dinoflagellate cyst assemblages can be used to interpret surface water mass characteristics including temperature, salinity, sea-ice cover and nutrient levels, as well as turbulence and stratification (Dale, 1996; Dale et al., 2002; de Vernal et al., 2001). Process length variation of cysts of *Protoceratium reticulatum* can be used to determine salinity (e.g., Jansson et al., 2014). Temperature, salinity, nutrient level and duration of sea-ice cover can be reconstructed for each fossil assemblage using transfer functions, a method commonly applied in paleoenvironmental reconstructions in which modern relationships between palynological assemblages and climate variables are applied to fossil assemblages to infer past climate conditions. The modern analogue method in particular has been used in this way (e.g. de Vernal et al., 1994, 2001, 2013). This method assumes that both the modern dinoflagellate cyst assemblages and the fossil assemblages were deposited under the same environmental conditions (de Vernal et al., 2001). The high abundance of heterotrophic dinocysts reflects high productivity (Radi and de Vernal, 2004), and hence can be used to determine productivity and in some cases upwelling in an oceanic environment. Dinoflagellate cysts can

also serve as indicators of eutrophication in paleoenvironmental reconstructions since they reflect the trophic level of surface waters, and have been linked with nutrients such as phosphate, silica, and nitrate (Devillers and de Vernal, 2000; Radi et al., 2007). The dinoflagellates that produce the cysts may be photosynthetic, heterotrophic or mixotrophic (Marret and Zonneveld, 2003). Hence, the modern distribution of dinoflagellate cyst assemblages on the sea floor can be used to interpret fossil assemblages and thereby reconstruct paleoceanographic changes through time.

The above comments nonetheless require some qualification. Transfer functions should in many instances be considered only as an approximate quantification of paleoenvironmental parameters, especially where the calibration set does not fully represent the range of environments to be reconstructed. There are also questions concerning the propriety (Dale and Dale, 2002, p. 235–237) and statistical validity (Telford, 2006; Telford and Birks, 2009, 2011) of the best analogue method. There is also the issue of taphonomy, notably transport and preservation. It is assumed that transport paths were similar in the past to those today, which becomes increasingly doubtful with increasing geological age, when ocean currents may have had a very different configuration. This is also the case in slope settings where dinoflagellate cysts can easily be transported in mass-wasted sediments. This concern of course relates to all transfer function methods and to all planktonic microfossil groups. Differential preservation is a particular issue for dinoflagellate cysts. The organic walls of protoperidiniacean cysts are less resistant to oxidizing bottom waters than those of gonyaulacacean cysts. Because protoperidiniacean dinoflagellates are heterotrophic, the relative abundance of their cysts in sediments is often used as an indicator of biological productivity. The selective destruction of protoperidiniacean cysts (Zonneveld et al., 1997, 2001) can therefore lead to underestimated interpretations of paleoproductivity although these concerns may be overstated (Reichart and Brinkhuis, 2003).

CHAPTER FOUR

4.0 MATERIALS AND METHODS

4.1 Age Model for the Chiba composite section

The age model used in the present study follows Suganuma et al. (2018) (See Fig. 8 below). It is well developed and based on recent refinements of the oxygen isotope stratigraphy, tephrostratigraphy, and magnetostratigraphy. The historical development of this age model is discussed in Kazaoka et al. (2015) and Suganuma et al. (2018). Okada et al. (2017) and Suganuma et al. (2018) analysed benthic foraminifera from the Chiba section and the Yoro-Tabuchi section from samples taken at 10 cm intervals, and developed an ultra-high-resolution oxygen isotope stratigraphy. *Bolivinita quadrilatera* and *Cibicides* spp. were used for the benthic record, these being the dominant species, with the necessary corrections being made to normalize the $\delta^{18}O$ values for these two taxa (Okada et al., 2017). For the planktonic oxygen isotope record, *Globigerina bulloides* and *Globorotalia inflata* were used (Suganuma et al., 2018). Because of the relatively short segment analysed at high resolution for the Chiba composite section, it had been necessary in Okada et al. (2017) and Suganuma et al. (2017) to tune this record to a longer local record rather than directly to the global benthic stack of Lisiecki and Raymo (2005). Such a local record is available from the CHOSHI-1 core (Shimosa Group), situated in the easternmost part of the Boso Peninsula, which extends from MIS 24 to MIS 11 using *G. inflata* (Kameo et al., 2006). Because the planktonic isotope records of the CHOSHI-1 core and the Chiba composite section are similar even in detail, the Chiba record was tuned to the CHOSHI-1 record, and the CHOSHI-1 record was then tuned to the global benthic stack of Lisiecki and Raymo (2005) to obtain an astronomical time scale for the Chiba composite section.

As a means to refine the age model at the Chiba section, the $\delta^{18}O$ benthic foraminiferal record was extended upwards in the Chiba section by Suganuma et al. (2018) who were then able to identify the MIS 19–18 boundary directly by comparison with the eustatic proxy curve of Elderfield et al. (2012) from ODP Site 1123 in the South Pacific. Because temperature and salinity effects had been removed from the curve of Elderfield et al. (2012), it was deemed an appropriate tuning target for the Chiba section. The new age model of Suganuma et al. (2018) therefore does not require use of the CHOSHI-1 core as an intermediary. There are slight but inevitable differences between the age model of Suganuma et al. (2018), which is used in the present paper, and that of Okada et al. (2017) and Suganuma et al. (2017).

To develop a high-resolution paleomagnetic record of the Chiba composite section, Okada et al. (2017) analysed the same sample set used for the oxygen isotope record, hence at a sample spacing of 10 cm. Samples required thermal and alternating field demagnetization to remove later magnetic overprinting (Okada et al., 2017). The midpoint of the Brunhes–Matuyama directional transition was found to be approximately 1.1 m above the Byk-E tephra bed. Based on the $\delta^{18}O$ record of Suganuma et al. (2018), the astronomical age for the M–B boundary (midpoint) is estimated at 772.9 ka, with a directional transition of 1.9 kyr. This astronomically derived age is consistent with the U-Pb zircon age of 770.9 ± 7.3 ka for the Byk-E tephra (Suganuma et al., 2015). The position of the Brunhes–Matuyama boundary is supported by a drop in the geomagnetic paleointensity (Okada et al., 2017; Suganuma et al., 2017) and by a peak in the ^{10}Be record (Suganuma et al., 2017).

The present study follows the newly derived ultra-high-resolution age model of Suganuma et al. (2018) (see Fig. 8) and is based on the same set of samples as those collected for isotopes and pollen (Suganuma et al., 2015, 2017). All results and interpretations in this study are given with reference to depth from the Byk-E bed (m) in the Chiba composite section. In accordance with Suganuma et al. (2018), the ages of the MIS boundaries follow Lisiecki and

Raymo (2005), and are taken from: http://www.lorraine-lisiecki.com/LR04_MISboundaries.txt. This source gives the ages of the MIS 20–19 and 19–18 boundaries as 790 ka and 761 ka, respectively. Substage nomenclature follows Railsback et al. (2015) with substage boundary ages for MIS 19 following Suganuma et al. (2018), as 771.7 ka (MIS 19c–19b) and 766.6 ka (MIS 19b–19a).

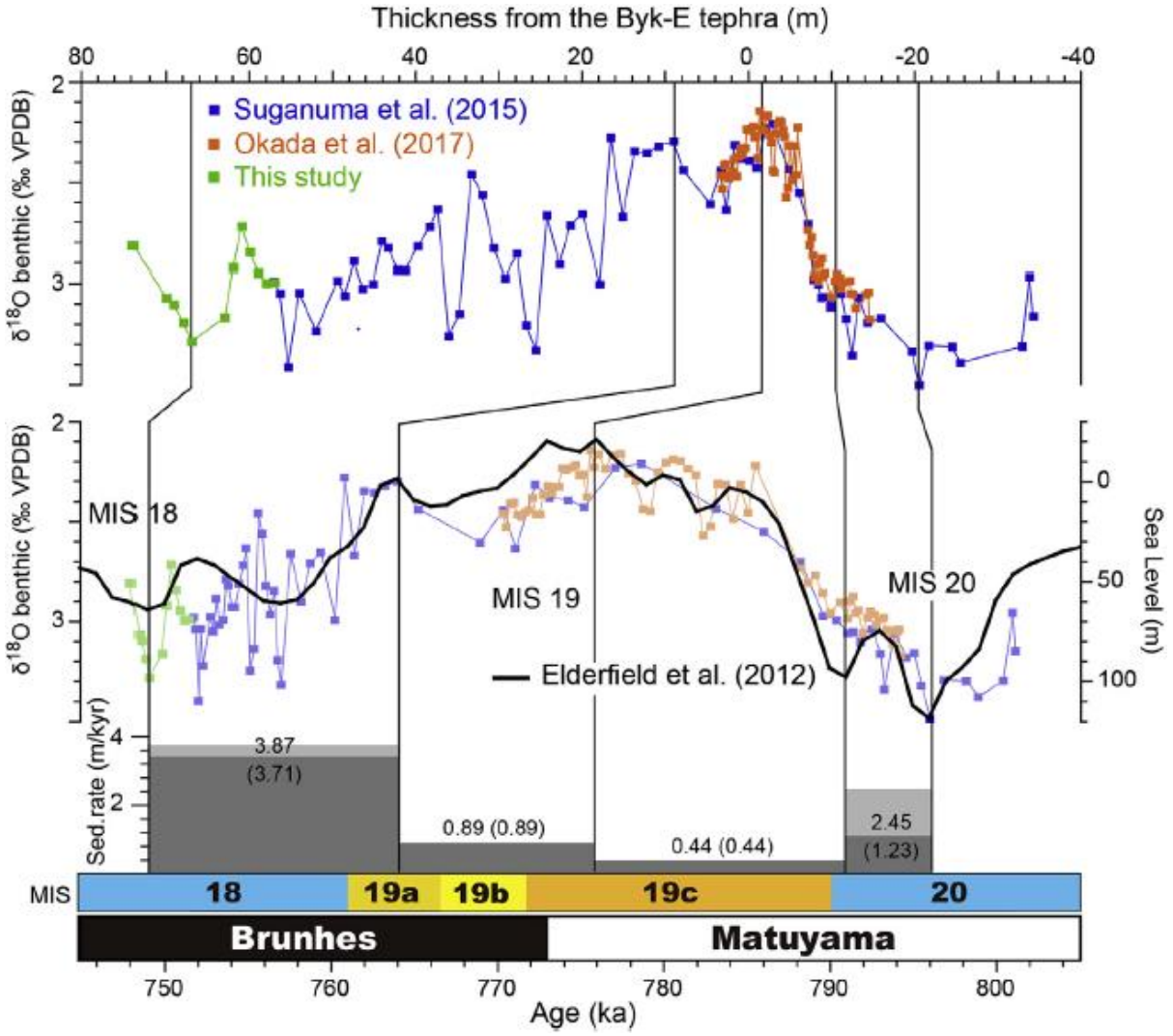

Fig. 8: Age model based on the high-resolution $\delta^{18}O$ stratigraphy from the Chiba composite section. It was developed by Suganuma et al. (2018) and is visually tuned to the eustatic curve of Elderfield et al. (2012) using major features of the $\delta^{18}O$ record, with assistance from the U-Pb age of the Byk-E tephra. The M–B boundary age is estimated at 772.9 ka based on this age model. Light grey shading represents thickness with sandstones (considered to be turbidites) and dark grey with without sandstones. There are no sandstones within the interval covered in the present study, which has an age range of 791–768 ka (latest MIS 20 to early MIS 19b) (From Suganuma et al., 2018, fig. 6).

4.2 Sample selection

In this study, 71 samples were selected from the Chiba composite section comprising the Chiba section (lower part of the Yoro River section) and the Yoro–Tabuchi section (see Figs. 9 and 10). Sample numbers are prefixed TB (Chiba section, formerly known as the Tabuchi section) or TB2 (Yoro–Tabuchi section). The samples span late MIS 20 to the lower part of MIS 19b, therefore including all of MIS 19c. Samples were collected under the direction of Prof. Makoto Okada and are subsamples of those used for foraminiferal isotope and pollen analysis (Okada et al., 2017; Suganuma et al., 2017, 2018). Samples were mostly taken at 20 cm spacing, and represent an average duration of ~324 years. The sampled interval is ~12 m long, with a depth extending from -8.5 m below the Byk-E bed to 3.5 m above the Byk-E bed and has an age range of 791–770 ka (see Table 1 in Appendix 4). Some samples within Termination IX, the interval from -8.5 m to -5.9 m below the Byk-E bed and ranging in age from 791 to 785 ka, are spaced at ~10 cm intervals to improve resolution across this important climatic transition. The sedimentation rates of the sampled interval (see Fig. 11) are generally relatively low (~0.44–1.23 m/kyr) compared to parts above and below this interval where rates of up to 3.7 m/kyr can occur (Fig. 8). The M–B boundary is in an interval with sedimentation rates of ~0.89 m/kyr. These low sedimentation rates coincide with periods of sea-level highstand during MIS 19 when the focus of sedimentation would have shifted landward (Suganuma et al., 2018). Estimated ages for samples used in the present study are listed in Table 1, appendix 4. They are mostly taken from Suganuma et al. (2018, supplementary table 2 available from the publisher's website), with the ages of remaining samples supplied by Prof. Makoto Okada, Ibaraki University). All sample ages are based on the age model of Suganuma et al. (2018).

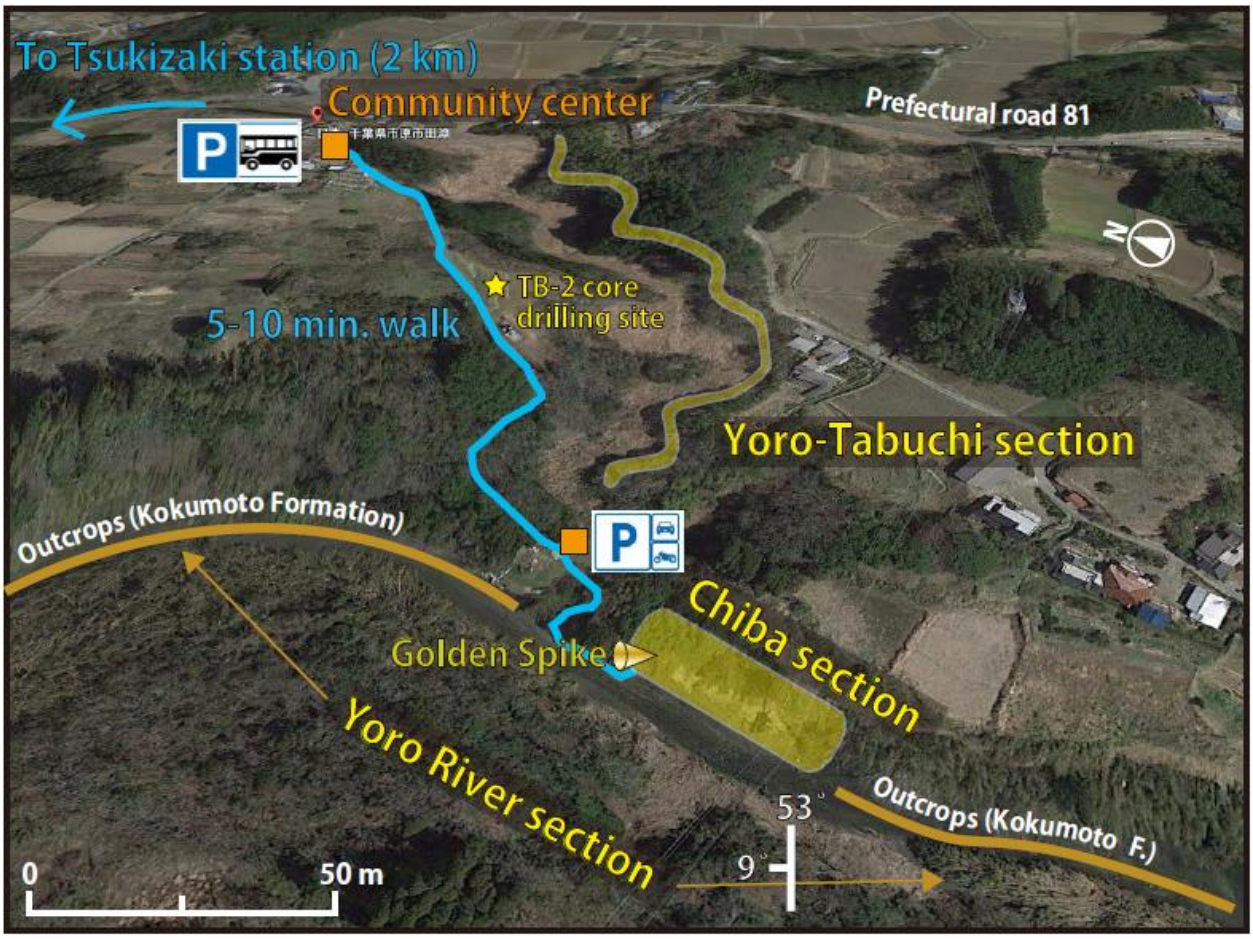

Fig. 9: Part of the Chiba composite section, here comprising the Yoro River section and the Yoro–Tabuchi section. The Golden Spike marks the proposed GSSP in the Chiba section, which is a segment of the Yoro River section. The yellow star indicates the location of the drilled TB-2 core. Samples analysed in the present study are from the Chiba section and the Yoro–Tabuchi section. (From Suganuma et al., 2017).

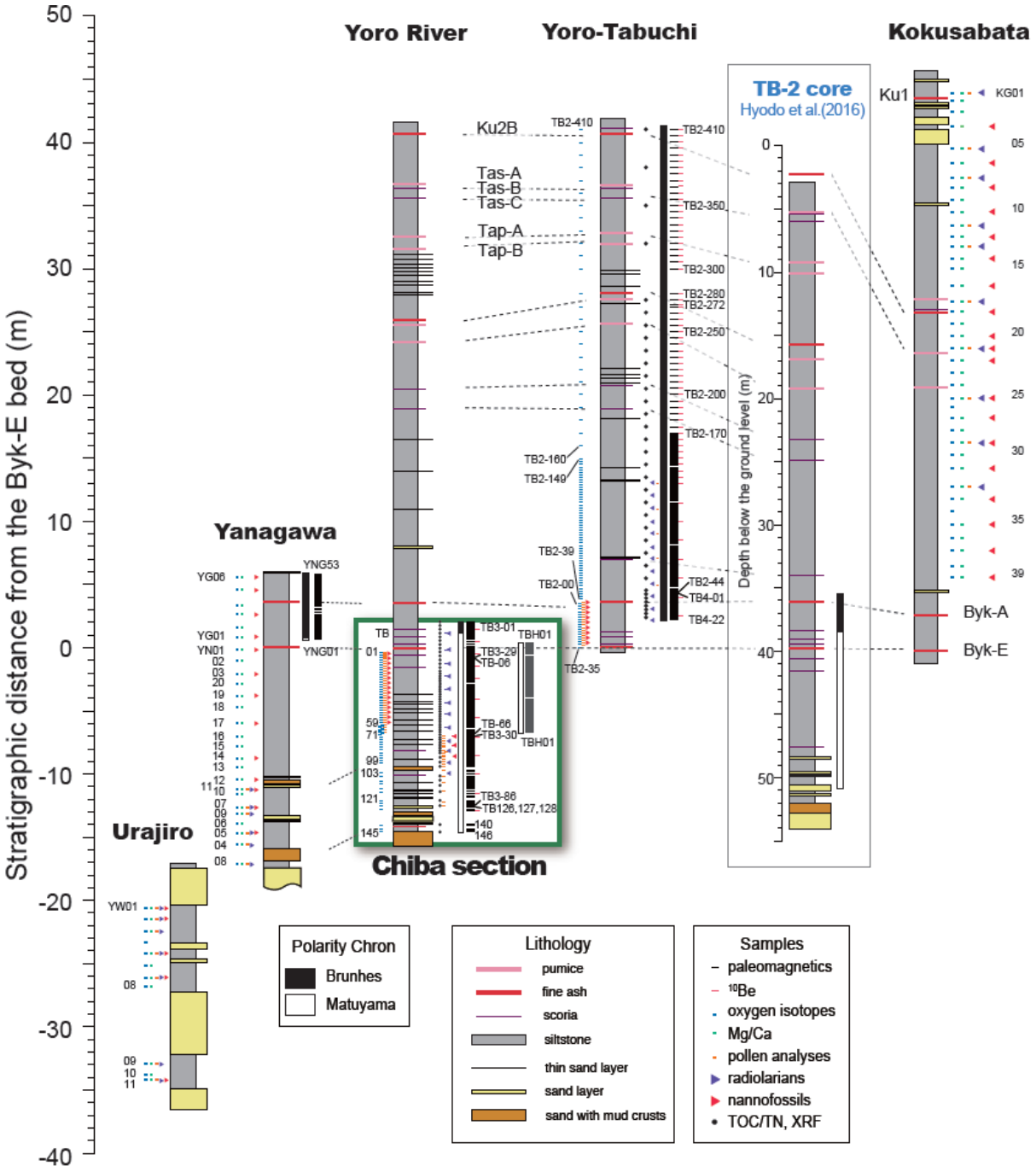

Fig. 10: Detailed stratigraphic correlations of the Chiba composite section between the Yanagawa, Yoro River, Yoro-Tabuchi, and Kokusabata sections. The stratigraphic correlations are based on lithological changes and number of marker tephra beds. Samples for paleomagnetic (thin horizontal bars) and $\delta^{18}O$ (light blue lines) measurements including previous studies (Suganuma et al., 2015; Okada et al., 2017), and pollen (orange squares) and marine microfossils (calcareous nannofossils: red squares and radiolarians: purple squares) analyses are shown. Samples used in the present study are from the oxygen isotope studies (light blue horizontal lines) of the Chiba and Yoro-Tabuchi sections. (From Suganuma et al., 2017, fig. 7). The samples used in the present study are from the Chiba section (samples TB 02–90) and Yoro-Tabuchi section (samples TB2 02–34).

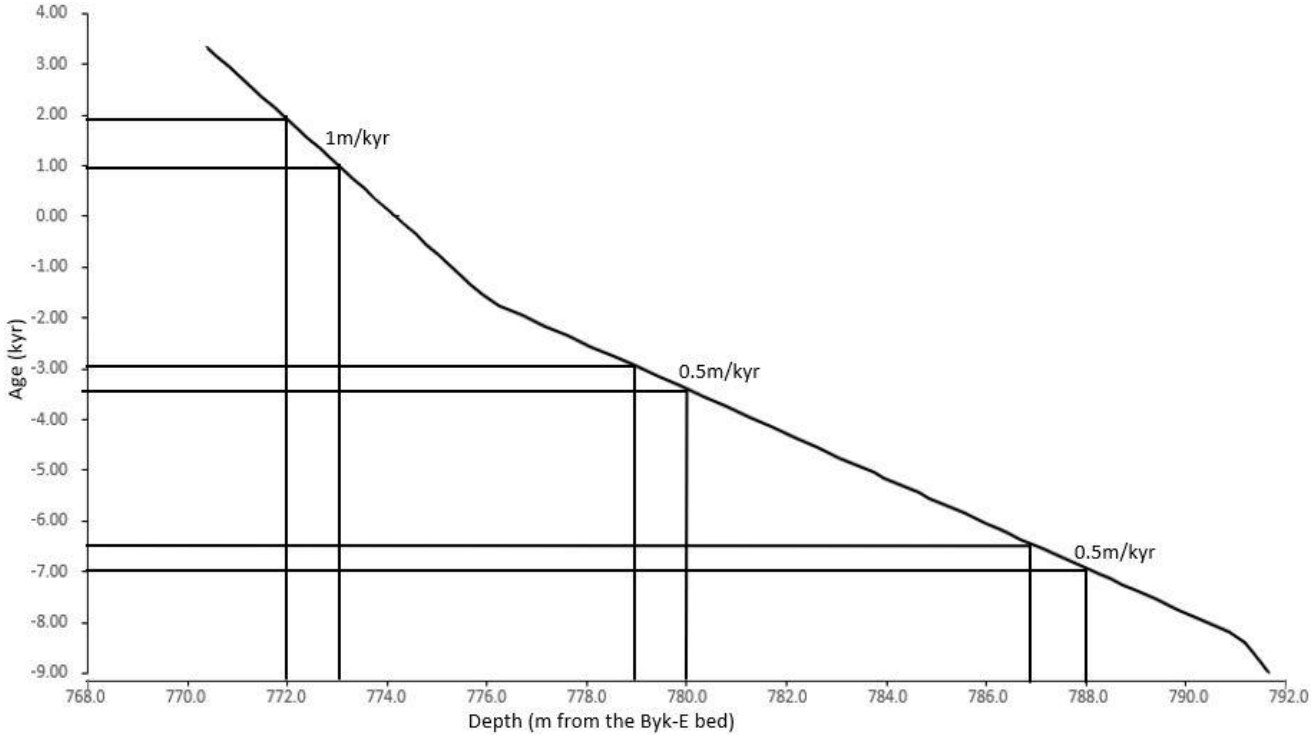

Fig. 11: Sedimentation rates for the study interval in the Chiba composite section, with sample ages based on the age model of Suganuma et al. (2018).

4.3 Palynological processing and analysis

Samples were processed in the palynology laboratory of Prof. M. J. Head, Department of Earth Sciences, Brock University, following protocols used in this lab (Appendix 3). Each sample was dried, weighed (~10 g) and placed in a 600 ml plastic beaker. HCl (20% of conc.) was added to remove carbonates and was neutralized after several hours by the addition of distilled water. After decanting, 38% HF was added to remove silicates, the sample was left to stand for ~2 days with intermittent swirling, and thereafter neutralized with distilled water. HCl was again added to the residue to remove any fluorosilicates, and neutralized. Tablets (Batch number 1031) containing spores of *Lycopodium clavatum* (20,848 spores per tablet) were added to the residue, which was vigorously mixed and sieved through a 10-µm nylon mesh. New sieving mesh was used for each sample. Residues were mounted on microscope slides using glycerine jelly. Only cold reagents were used, and no oxidation or alkali

treatments were applied. After sieving, wet preparations did not indicate the need for ultrasound. At least 3 slides were made for each sample for microscopic study. The surplus residue was stored in vials containing glycerine to which one drop of liquefied phenol had been added to prevent microbial growth.

Palynological analysis was conducted on the prepared slides by examining and counting palynomorphs on each slide using a Leica DM 2500 transmitted light microscope. During routine counting, each slide was scanned using a 40x objective lens, with the 100x oil immersion objective lens used for detailed morphological analysis and the identification of small palynomorphs, especially small acritarchs, as well as any poorly preserved and obscured specimens. Dinoflagellate cysts, being the focus of this study, were identified to species level where possible during counting. However, other palynomorph groups were also counted. They included reworked specimens, foraminiferal linings, and pollen and spores. Reworked specimens were distinguished on the basis of colour, preservation (especially compression), and stratigraphic discordance. During the analysis, only those foraminiferal linings with at least six chambers were counted, to avoid over-representation, because most of them were fragmented, appearing with single/double chambers. For the dinoflagellate cyst analysis, a minimum of 300 in-situ specimens per sample was counted for most of the samples. However, for six samples with low dinoflagellate cyst concentrations, a minimum of 200 specimens was counted; and eight samples yielded fewer than 200 counts, even after scanning up to three slides for each (see Table 1, appendix 4). An average of 500 *Lycopodium* spores was counted for each sample. The concentrations (specimens per gram dry weight) of dinoflagellate cysts and terrestrial palynomorphs were calculated using the method of Stockmarr (1971).

For each sample, at least one specimen of each species was noted using an England Finder reference number. Photogenic specimens were photographed in transmitted light using a

Leica 2500 MC microscope and Leica 170 HD digital camera. Plates illustrating all dinoflagellate cyst taxa recorded are shown in Appendix 2. Tables 1 and 2 in Appendix 4 shows the raw counts of all taxa encountered during the palynological analysis. All analyses were performed in the Department of Earth Sciences, Brock University.

4.4 Taxonomy and nomenclature

Identification of dinoflagellate cysts recorded in this study mainly uses Rochon et al. (1999) and De Schepper and Head (2008). Some specimens were identified only to genus level, either due to their poor preservation or unfavourable orientation. Dinoflagellate cyst nomenclature mostly follows Williams et al. (2017).

4.5 Statistical analysis

4.5.1 Modern analogue technique

An attempt is made to reconstruct past sea-surface temperature and salinity from the Chiba dinoflagellate cyst record by means of the Modern Analogue Technique (MAT). This method has been used frequently in paleoenvironmental reconstructions for the Quaternary, especially in the North Atlantic (e.g. de Vernal et al., 1994, 2001). In this method, modern relationships between palynological assemblages and climate variables are applied to fossil assemblages to infer past climate conditions. This requires the use of a data set that contains a record of modern dinoflagellate cyst assemblages from sea-floor surface sediments and has relationship with modern water mass parameters (especially sea-surface temperature and salinity). These parameters are taken from the World Ocean Atlas 2013. The modern dinoflagellate cyst assemblages and the fossil assemblages are assumed to have been deposited under the same environmental conditions. Extensive modern dinoflagellate cyst assemblages forming a reference data set that represents a wide range of sea-surface conditions must be available for comparison (de Vernal et al., 1993). Various approaches are

possible, so a validation test must be conducted to determine the reliability and accuracy of each one, allowing the best method to be chosen (e.g., de Vernal et al., 1998, 2000, 2005a).

Unfortunately, no modern dinoflagellate cyst data set is available for the western North Pacific that represents the range of environmental variables that might be expected of the Chiba record. A modern dinoflagellate cyst data set for the eastern North Pacific does exist (Radi and de Vernal, 2008a) but the east and west North Pacific margins have very different hydrographic regimes. Hence, the modern Northern Hemisphere dinoflagellate cyst database (n=1207) compiled by Radi and de Vernal (2008) was used for the quantitative reconstruction because it has more similar assemblages to those recovered from the Chiba composite section. To avoid having negative values during logarithmic transformation when running the MAT, the relative abundances of all dinoflagellate cysts from the Northern Hemisphere database and Chiba section were converted to per-thousand rather than percent. The logarithmic transformation of dinoflagellate cyst abundances usually helps to give more relevance to species with lower occurrences, an important consideration because these species tend to cover a narrower range of environmental conditions than those that are abundant (e.g. de Vernal et al., 2001, 2005; Verleye and Louwye, 2010). Samples at depths of -1.55, -4.15, -4.35, -5.25, -7.94, -8.31 m were removed from the MAT because they lacked a modern analogue.

With the support of scripts adapted from GEOTOP (http://www.geotop.uqam.ca), the software R (R Core Team, 2012) was chosen to run the transfer function using the modern data set covering the Northern Hemisphere (n=1207) against the dinoflagellate cyst assemblages in this study. This modern data set contains assemblage information on 1207 sea-floor surface samples located across the Northern Hemisphere. The locations of surface samples used in the modern data set are shown in Fig. 11, sourced from de Vernal et al. (2013a, b), an update of the data sets published by de Vernal et al. (1997, 2001, 2005), Radi

and de Vernal (2008), and Bonnet et al. (2010). Reconstructions for February and August sea surface temperature and salinity are given, and represent winter and summer conditions respectively. After running the MAT on the Chiba dinoflagellate cyst assemblages against the Northern Hemisphere data set, all the samples produced reconstructed values except six samples that yielded a 'no analogue' (N/A) result (see Table 1). The acritarch *Nannobarbophora walldalei* and the reworked dinoflagellate cyst *Cleistosphaeridium placacanthum* were excluded because they are extinct. For validation and calculation of the Root Mean Square Error (RMSE), the leave-one-out method, which uses 1/6th of the calibration data for verification purposes of the reconstruction, was used. The list of taxa used for the MAT reconstruction can be seen in Table 2.

Sample Number	**Depth (m from Byk-E bed)**	**Age (ka)**	**MAT results**	**MIS**
TB 16	-1.55	776	N/A	MIS 19
TB 42	-4.15	781	N/A	MIS 19
TB 44	-4.35	782	N/A	MIS 19
TB 52	-5.25	784	N/A	MIS 19
TB 84	-7.94	792	N/A	MIS 20
TB 88	-8.31	792	N/A	MIS 20

Table 1: The six samples that yielded "no analogue" (N/A) results using MAT for the reconstruction.

Taxa used for MAT reconstruction	**Abbreviations**	**Note**		
Achomosphaera spp. total	ACHO			
Brigantedinium spp. total	BSPP			
Cyst of *Scrippsiella trifida*	ALEX			
Impagidinium paradoxum	APAR			
Impagidinium patulum	APAT			
Impagidinium sphaericum	ISPH			
Impagidinium spp. indet.	ISPP			
Lingulodinium machaerophorum	LMAC			
Nematosphaeropsis labyrinthus	NLAB			
Operculodinium centrocarpum sensu Wall and Dale 1966	OCEN			
Operculodinium centrocarpum	OISR			
Protoperidinioids	PERI			
Pyxidinopsis reticulata	PRET			
Selenopemphix nephroides	SNEP			
Selenopemphix quanta	SQUA			
Spiniferites mirabilis	SMIR	Grouped together		
Spiniferites hyperacanthus	SMIR			
Spiniferites spp. indet.	SSPP			
Tuberculodinium vancampoae	TVAM			
Xandarodinium xanthum	XAND			

Table 2: Dinoflagellate cyst taxa used in the MAT analysis. Abbreviations of their names and grouping used in the MAT analysis are shown.

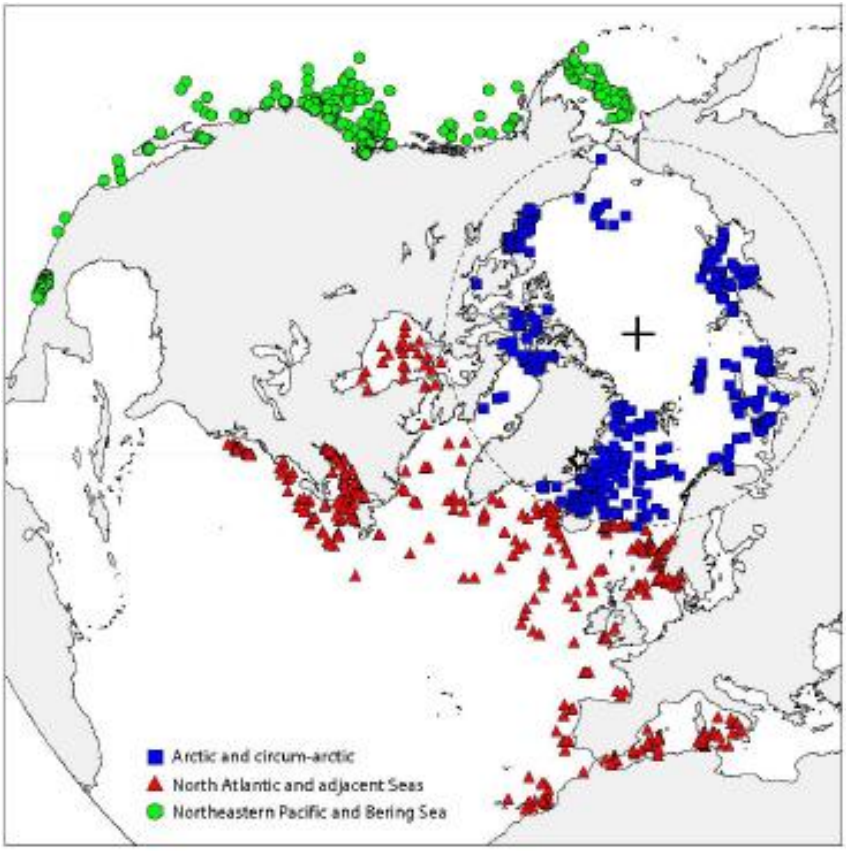

Fig. 12: Northern Hemisphere data set of modern dinoflagellate cyst assemblages used for the present MAT reconstructions of the Chiba section (from Radi and de Vernal, 2008a, fig. 4a).

4.5.2 Constrained cluster analysis

Constrained cluster analysis (CCA) was also used. It is often performed on palynological data (e.g. Versteegh, 1995; McCarthy et al., 2000a; Hammer et al., 2001; Dale and Dale, 2002a; Hennissen et al., 2017) because of its importance in understanding the ecological response of palynomorphs by comparing the results directly to known paleoecological parameters (Hennissen et al., 2017). Constrained Cluster Analysis in this study was performed exclusively on the dinoflagellate cyst assemblages.

CCA involves the collection of individual samples with similar features into larger groups in hierarchical order, while at the same time preserving the local similarity or the stratigraphic

position of the samples, which is more important than the larger differences (Dale and Dale, 2002a). The constrained cluster analysis was performed using “R” statistical software based on the presence or absence of each species in all the samples (Ryan et al., 1995; Hammer et al., 2009). Both presence/absence and abundance of each species was prepared separately on an Excel spreadsheet as a file, which was then entered separately into “R” statistical software and allowed to run on the program. Both generated the same result, but the result derived from presence/absence was eventually used. This was done in order to subdivide the palynological record into biozones or groups of similar species composition (Fig. 18). The agglomeration algorithm used is called "coniss", which is explained in Grimm (1987). It involves using an incremental sum of squares to determine the similarity while maintaining stratigraphic order. All 71 samples were used for the analysis. Foraminiferal linings (belonging to benthic foraminifera) and reworked dinoflagellate cysts were excluded from the biozonation as these do not carry the same ecological signals as the in-situ dinoflagellate cysts.

4.5.3 Species richness

The species richness of a sample is simply the total number of species recorded in that sample. It is an important factor in measuring diversity. However, it does not take into account the proportion and distribution of each species in the sample (De Schepper, 2006; Gotelli and Chao, 2013). The number of dinoflagellate cyst taxa recorded in the 300 specimen count for each sample was used to determine its species richness: the more species, the higher the species richness.

4.5.4 Species evenness

Species evenness quantifies how equal species are numerically in a sample. It is an index for diversity and takes into consideration the proportion and distribution of each species in each

sample. Greatest evenness is where all species in a sample share the same abundance. Various metrics are available for calculating evenness. A common index is the Simpson D index which is one of the most meaningful and robust diversity measures available (Magurran, 2004). The measure ranges from 0 to 1 and is not sensitive to species richness. The higher the value, the more even the species.

First, we derive Simpson's D: $(1/\sum p_i^2)$. Then, evenness (E) = D/D_{max}

Where:

p_i is the proportion of each species in a sample = Number of individual species/Total number of all species present in a sample.

D known as the Simpson's D is a measure of diversity.

D_{max} is the number of species recorded in a sample.

CHAPTER FIVE

5.0 RESULTS

5.1 Dinoflagellate cyst assemblages

Moderately preserved dinoflagellate cyst assemblages were recorded in all 71 samples analysed. A total of 14 genera and 29 species were registered (see Table 1 in Appendix 4). The assemblages consist of both protoperidinoid and gonyaulacoid dinoflagellate cysts representing heterotrophic and autotrophic dinoflagellates respectively, and primarily reflect neritic environments (see Appendix 2). The protoperidinoid/gonyaulacoid ratio varies throughout the studied interval in response to paleoceanographic and perhaps taphonomic changes. Dinoflagellate cysts recorded from the Chiba composite section include the protoperidinoid taxa *Brigantedinium* spp. (0.3–92%), cysts of *Protoperidium nudum* (0.3–22%), *Selenopemphix nephroides* (0–6%), and *Xandarodinium xanthum* (0–2%). The gonyaulacoids are represented by the neritic taxa *Lingulodinium machaerophorum* (0.3–47%), *Operculodinium israelianum* (0.2–3.6%), cysts of *Protoceratium reticulatum* (3–93%), *Spiniferites mirabilis*/*hyperacanthus* (0.3–22%), *Achomosphaera*/*Spiniferites* spp. (0.3–47%), *Pyxidinopsis reticulata* (0–1%), *Scrippsiella trifida* (0.2–2.2%), and *Tuberculodinium vancampoae* (0–4%), as well as the outer neritic to oceanic *Nematosphaeropsis labyrinthus* (0.2–7%), which are also found in estuaries (Pospelova et al., 2005) and the oceanic genus *Impagidinium* (0.2–1%) comprising *I. aculeatum*, *I. paradoxum*, *I. patulum*, and *I. sphaericum.* Their relative abundances and stratigraphic distributions are shown in Fig. 13. Most of the species recorded occur throughout the interval except for a few, such as *Pyxidinopsis reticulata*, *Scrippsiella trifida*, *Impagidinium aculeatum, I. paradoxum, I. patulum*, and *I. sphaericum*, that occur only in MIS 19c.

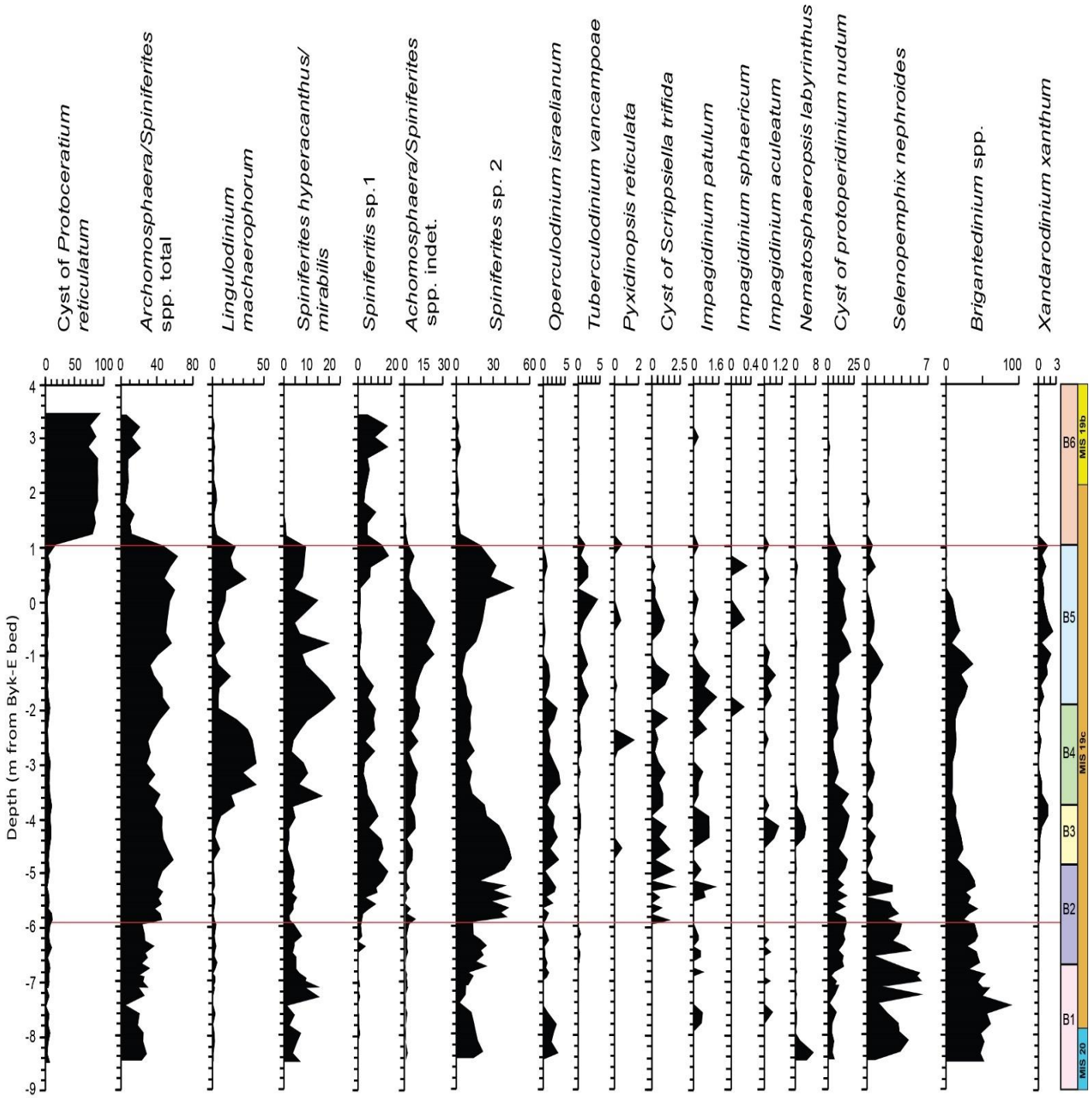

Fig. 13: Stratigraphic distribution and relative abundances of all important dinocyst taxa recorded from the Chiba composite section plotted against depth. The red lines indicate horizons of significant paleoceanographic change during MIS 19c in the dinoflagellate cyst record. Biozones B1–B6 are based on constrained cluster analysis (See Fig. 18). MIS stages and substages are from Suganuma et al. (2018).

5.1.1 Dinoflagellate cyst concentrations

Dinoflagellate cyst concentrations (cysts per gram of dry sediment) are shown in Fig. 14. Through most of the study interval (-8.5–1.0 m; 791–773 ka), concentrations are generally rather low and stable, ranging between ~1000 and ~5000 cysts/g, with an average of ~3000 cysts/g. A sharp increase occurs at exactly 1.0 m (773 ka) just above the Byk-E tephra bed where concentrations increase to ~62,000 cysts/g and drop slightly thereafter, fluctuating between ~20,000 and ~50,000 cysts/g at about 1.4–2.4 m before increasing again. At ~2.6 m, concentrations peak at ~156,000–316,000 cysts/g before decreasing significantly to ~27,000 cyst/g in the uppermost part of the interval (~3 m above the Byk-E bed). The increase in dinoflagellate cyst concentrations toward the top of the interval, between 1 m and 3 m above the Byk-E bed (773–770 ka), is particularly conspicuous, and the sudden increase at 1.0 m corresponds to the position of the M–B boundary at 1.1 m above the Byk-E bed (Okada et al., 2017) which is dated to 772.9 ka (Suganuma et al., 2018). This increase is largely due to the sharp increase in the abundance of cyst *Protoceratium reticulatum* which comprises up to ~93 % of the total dinoflagellate cyst assemblages at the top of the studied interval.

5.1.2 Heterotrophic dinoflagellate cysts

The heterotrophic dinoflagellates are represented in the Chiba composite section by protoperinoids, their cysts including *Brigantedinium* spp., cyst of *Protoperidinium nudum*, *Selenopemphix nephroides* and *Xandarodinium xanthum* (see Fig. 13). These dinoflagellate cysts occur throughout the interval except *Xandarodinium xanthum*, a temperate to tropical species (Harland, 1983; Marret and Zonneveld, 2003), which occurs in low abundances (0–2%) exclusively in MIS 19c (Fig. 13). Due to the crumpling and degradation of *Brigantedinium* specimens throughout the interval, their identification to species level was not possible. They were therefore grouped as *Brigantedinium* spp.

Among the heterotrophic species recovered from the Chiba section, *Brigantedinium* spp. is the most abundant (Fig. 14), with relative abundances ranging from 0.3 to 92% through the interval, followed by cysts of *Protoperidinium nudum* (0.3–22%) and *Selenopemphix nephroides* (0–6%).

5.1.3 Autotrophic dinoflagellate cysts

Most cysts recorded from the interval belong to gonyaulacoid and autotrophic dinoflagellates. They occur in high abundance throughout the peak of MIS 19, beginning at the end of termination IX (-6 m, 785 ka) and extending to the top of the interval (3.4 m, 770 ka) (Fig. 14). They represent both neritic and oceanic environments, and include cyst *Protoceratium reticulatum* (3–93%), *Lingulodinium machaerophorum* (0.3–47%), *Operculodinium israelianum* (0.2–3.6%), *Nematosphaeropsis labyrinthus* (0.2–7%), *Spiniferites mirabilis/hyperacanthus* (0.3–22%), *Achomosphaera/Spiniferites* spp. (0.3–47%), *Pyxidinopsis reticulata* (0–1%), cysts of *Scrippsiella trifida* (0.2–2.2%), *Tuberculodinium vancampoae* (0–4%), and the genus *Impagidinium* (0.2–1.0%) represented by *I. aculeatum*, *I. paradoxum*, *I. patulum*, and *I. sphaericum* (see Fig. 13). Most of these species occur throughout the interval except that *Pyxidinopsis reticulata*, cysts of *Scrippsiella trifida*, and the genus *Impagidinium* were recorded only in MIS 19c, in low abundance.

Protoceratium reticulatum is a cosmopolitan species ranging today from the tropics to high latitudes, but is particularly abundant in regions with cool/temperate nutrient-enriched surface waters such as the North Atlantic Current (Rochon et al., 1999; Zonneveld et al., 2013; Hennissen et al., 2014, 2015, 2017).

Lingulodinium machaerophorum occurs mostly in coastal regions and is tolerant of a wide range of salinities and temperatures in nearshore environments (Rochon et al., 1999). It is usually found in temperate to equatorial regions of both the Northern and Southern

Hemisphere with temperatures of 10°C in summer and 0°C in winter. High relative abundances occur in the vicinity of active upwelling cells and near river mouths (Zonneveld et al., 2013). This species has been linked to elevated nutrient levels (Dale, 1996). Reduced process length in *Lingulodinium machaerophorum* is known to be related to low salinity (Zonneveld et al., 2013).

Operculodinium israelianum is regarded as a mild-temperate to equatorial species and has been recorded from coastal and open oceanic sites, although down-slope transport must be considered for these deeper-water occurrences. This species is associated with high salinity and regions where bottom waters are well ventilated. It can be abundant in regions where SSTs exceed 14.3°C in winter and 24.2°C in summer (Head, 1996; Zonneveld et al., 2013).

Nematosphaeropsis labyrinthus is mostly found in fully marine settings with a distribution extending from the Arctic to the equator (Pospelova et al., 2005). It has been recorded with high relative abundances in both eutrophic and oligotrophic environments (Zonneveld et al., 2013). Studies of the Pliocene–Pleistocene boundary in the North Atlantic show an association with transitional climatic conditions during changes in water mass composition (Hennissen et al., 2017).

Spiniferites mirabilis and *Spiniferites hyperacanthus* were grouped together because the antapical flange that is characteristic of *Spiniferites mirabilis* may not be visible if the orientation of the specimen is unfavourable. *Spiniferites mirabilis/hyperacanthus* occurs in high abundances during MIS 19c. It is known to be a temperate to tropical species, usually found today where winter temperatures are greater than 13°C, and specimens can dominate associations in both oligotrophic and eutrophic environments (Harland, 1983; Edwards and Andrle, 1992; Head, 1996; Rochon et al., 1999; Zonneveld et al. 2013). This taxon is found in

neritic and oceanic environments. In the present study, relative abundances fluctuate from 0 to 22% with the highest abundances occurring during MIS 19c.

Achomosphaera/Spiniferites spp. total consists of all cysts of the genera *Achomosphaera* and *Spiniferites*, including those identified to species level (see Fig. 13). Today, members of these genera are most common on the continental shelves (Zonneveld et al. 2013). During the MIS 20/19 transition (termination IX), *Achomosphaera/Spiniferites* spp. total increased in abundance from ~18% to ~60% and maintained a stable occurrence through the peak of MIS 19, although it decreased toward the top of the interval just above the Byk-E bed due to an increased dominance of *Protoceratum reticulatum* (Fig. 13).

Tuberculodinium vancampoae is the cyst of *Pyrophacus steinii* whose motile cell occurs in warm-temperate to tropical environments today (Faust, 1998; Head et al., 2005; Zonneveld et al., 2013). It is often found in subtropical to equatorial coastal regions and in regions with enhanced or reduced SSS (Wall et al., 1977; Bradford and Wall, 1984; Lee and Yoo, 1991; Martinez-Hernandez and Hernandez-Campos, 1991; McMinn, 1991; Dale, 1996). In this study, *Tuberculodinium vancampoae* has its highest relative abundance of 4.6% at around the Byk-E bed, although during the peak of MIS 19 it was recorded mostly with low abundance (0–4%). Its distribution is shown in Fig. 10.

Impagidinium aculeatum, *I. paradoxum*, *I. patulum*, and *I. sphaericum* were recorded in very low abundances (0–1%) and occur mainly during MIS 19c (Fig. 13). They are referred by Rochon et al. (1999) to their "warm water suite of species". Most notably, these species are reliable indicators of oligotrophic, oceanic water masses even when occurring in low numbers (Dale, 1996).

Finally, it is observed that autotrophs, particularly cysts of the genera *Achomosphaera* and *Spiniferites*, increase in relative abundance upsection from the MIS 20/19 transition and

through MIS 19c, while the heterotrophs decreased significantly from the MIS 20/19 transition with the exception of a small rise at about 1m (775 ka) followed by a steady decline to very low values at 1.2 m (772 ka) (Fig. 14).

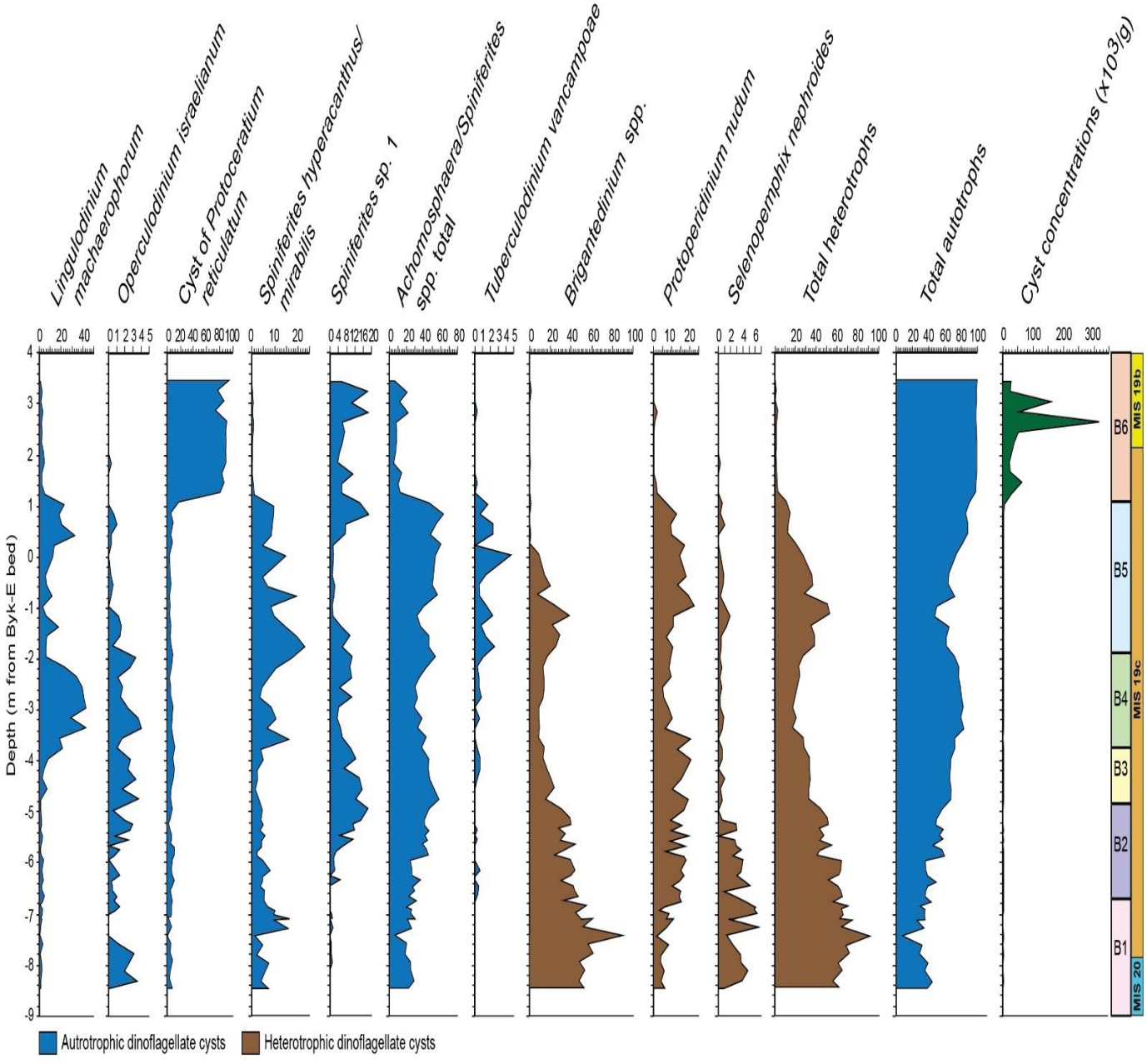

Fig. 14: Relative abundances of the main dinoflagellate cyst taxa and dinoflagellate cyst concentrations, including total autotrophs and heterotrophs through the study interval, reflecting paleoceanographic changes in the western Pacific Ocean during MIS 19. Plotted against depth. Biozones B1–B6 are based on constrained cluster analysis (this study). MIS stages and substages are from Suganuma et al. (2018).

5.2 Other palynomorphs

5.2.1 Terrestrial palynomorphs

Pollen and spores were also counted during the analysis and are included in this study (Table 2 in Appendix 4, Fig. 15) to ascertain the extent of terrestrial influence at the Chiba site during MIS 19. No attempt was made to identify pollen and spores to species level, although a detailed genus/species-level study of the pollen and spores has been conducted by Suganuma et al. (2018). Terrestrial palynomorphs recorded in this study include bisaccate pollen, monosaccate pollen (*Tsuga*), angiosperm pollen, and spores. Note that fern and bryophyte spores and fungal spores are grouped together as spores. These spores in general appeared somewhat flattened/compressed in all the samples and may suggest reworking since the bisaccate pollen and *Tsuga* appear less compressed. Preservation of the sporomorphs is otherwise generally good to moderate. The relative abundances are shown in Fig. 15. The palynoflora largely consists of bisaccate pollen ranging from 15% to 67%. The relative abundance of bisaccate pollen changes through the section, with maxima at the base and at ~-6.5 m, -2.0 m, ~0 m, and ~3.0 m, and minima at ~-4.5 m and ~-1.0 m. *Tsuga* decreases upsection in abundance (from 55 to 5%) at the MIS 20/19 transition (Termination IX) and remains consistently low (5–15%) throughout MIS 19c. It increases again at ~2.5 m in MIS 19b (Fig. 15). On the other hand, angiosperm pollen (*Quercus*, *Fagus*, *Alnus*, *Juglans*, etc.) shows high abundance during MIS 19c. It increases conspicuously from 10% to 65% at ~-6.0 m low in MIS 19c and remains high throughout MIS 19c, decreasing sharply again from 55% to 3% at MIS 19b (Fig. 15). The abundance of spores fluctuates between 5% and 10% for much of the interval, although it shows increases at ~-7.0–-5.0 m in the lower part of MIS 19c and again toward the top of the interval at ~2.0 m near the MIS 19c/b transition (Fig. 15).

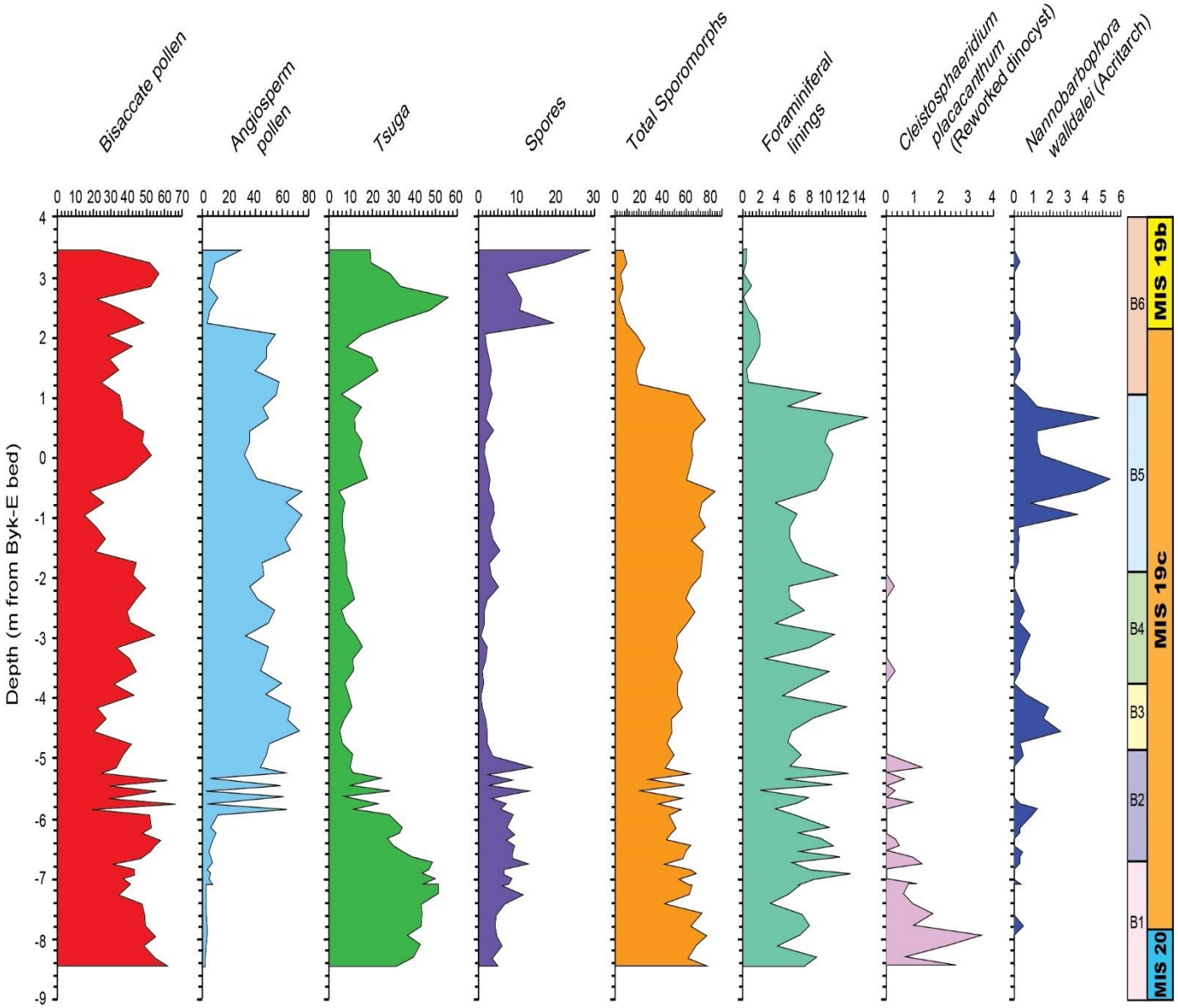

Fig. 15: Relative abundances of pollen and spores (based on total spores and pollen) recorded from the Chiba composite section showing terrestrial influence during MIS 19. Plotted against depth. Relative abundances of foraminiferal linings, *Cleistosphaeridium placacanthum* (reworked dinoflagellate cysts) and *Nannobarbophora walldalei* (acritarch) plotted as a percentage of the total in-situ dinoflagellate cysts (e.g., foraminiferal linings / foraminiferal linings + in-situ dinoflagellate cysts). Biozones 1–6 are based on constrained cluster analysis (this study). MIS stages and substages are from Suganuma et al. (2018).

5.2.2 Acritarchs and foraminiferal linings

The only acritarch recorded is *Nannobarbophora walldalei*, a species not known to range higher than the lowermost Middle Pleistocene (see Fig. 15). It was formally described by Head (1996) from the Lower Pleistocene (Gelasian) of the Norwegian Sea, and has been reported from the Lower Pleistocene (Gelasian) of eastern England (as cf. *N. barbata*, in Head, 1994, and as *Nannobarbophora* sp. in Head, 1996, 1998), Lower Pleistocene (Gelasian) of the North Sea (Head et al., 2004), Lower Pleistocene (Gelasian) of Italy (as Acritarch sp. B in Versteegh, 1994, 1995; Versteegh and Zonneveld, 1994), Upper Miocene of Morocco (as *Impletosphaeridium acropora* in Warny and Wrenn, 1997); Lower Pliocene through lowermost Middle Pleistocene of DSDP Hole 610A, eastern North Atlantic (De Schepper and Head, 2009); Upper Miocene through lowermost Middle Pleistocene of DSDP Hole 603C (M. J. Head, unpublished data); and Lower Pleistocene (early Gelasian) of the Bahamas (Head and Westphal, 1999). The previously reported range of *Nannobarbophora walldelei* is therefore Upper Miocene through lowermost Middle Pleistocene. This species is associated with tropical to warm/mild-temperate conditions (Head and Westphal, 1999) and is associated with warmer MISs in the Mediterranean (as Acritarch sp. B in Versteegh, 1994, 1995; Versteegh and Zonneveld, 1994). *Nannobarbophora walldelei* was found fairly consistently through the study interval but with very low relative abundances (0–4%), most specimens appearing crumpled and of similar preservation to most of the dinocysts. The relative abundances of *Nannobarbophora walldelei* was derived as a percentage of the total dinoflagellate cysts.

Foraminiferal linings were also registered throughout the interval. Their relative abundances based on the total dinoflagellate cysts are shown in Figure 15 above. They ranged from 3 to 14% between depths of -8.5 to 1.0 m before dropping to 0–1% just above 1.0 m. They are common in all samples and appear similar to the range of morphotypes illustrated in Traverse

and Ginsburg (1966) and Head and Westphal (1999). Foraminiferal linings are mostly produced from calcareous benthic foraminifera (Stancliffe, 1989), an affinity confirmed by de Vernal et al. (1992a) who demonstrated late Quaternary lining-producing foraminifera from the northwest North Atlantic to be exclusively benthic. Although few studies exist that contain details of the ecology and distribution of foraminiferal linings, it is known that increased abundances relate well to nutrient-rich waters and shallow depositional environments (Stancliffe, 1989; Head, 1993b).

5.2.3 Reworked dinocysts

Little obvious reworking was recorded in the present study, although its influence must be assumed given the continental slope setting of the deposits. The rare presence of the reworked dinoflagellate cyst *Cleistosphaeridium placacanthum* (see Fig. 15), which has a range of Middle Eocene to Late Miocene (Eaton et al., 2001), attests to the limited reworking of pre-Quaternary marine deposits. Low abundances of *Cleistosphaeridium placacanthum* were recorded based on total dinoflagellate cysts, with relative abundances of 0–3% between depths of -8.5 and -2 m. It has a highest occurrence at a depth of -2 m.

5.3 Statistical analysis

5.3.1 SST and SSS reconstruction using Modern Analogue Technique (MAT)

The MAT was conducted using a calibration dataset from the Northern Hemisphere (Radi and de Vernal, 2008), for reasons given in the Methods section. Samples at depths of -1.55, -4.15, -4.35, -5.25, -7.94, and -8.31 m were removed from the MAT because they lacked a modern analogue.

Results of the validation tests are shown in Fig. 16. The reconstruction in Fig. 16 shows that February SST ranges from -1 to 15 °C whereas August SST ranges from 4 to 25 °C. February and August SSS ranges from 28 to 38 psu. The obtained coefficients of correlation (r^2) for each parameter show significant accuracy between the predicted and reconstructed data. The best reconstruction corresponds to the February SSTs (Fig. 16a) with r^2 higher than 0.97 and a root mean square error (RMSE) of 1.04ºC.

The MAT-based SSTs and SSSs for the Chiba composite section are shown in Figure 17 below. Both SSTs and SSSs show high values during the peak of MIS 19. The MAT-based sea-surface temperatures for both February (SST_F) and August (SST_A) show significant warming (increase in temperatures) as expected during the MIS 20/19 transition (Termination IX). SST_F increases up to ~10–15°C while SST_A rises to ~18–21°C. It is noteworthy that this warming is interrupted by sudden but brief cooling (~-1°C) that is somewhat reminiscent of the Younger Dryas event during Termination I just prior to the Holocene. During MIS 19c, SSS for February fluctuates between 28 and 36 psu while SSS for August fluctuates between 27 and 32 psu. The transition from MIS 19c to MIS 19b is marked by decreases in both February and August SSTs and SSSs.

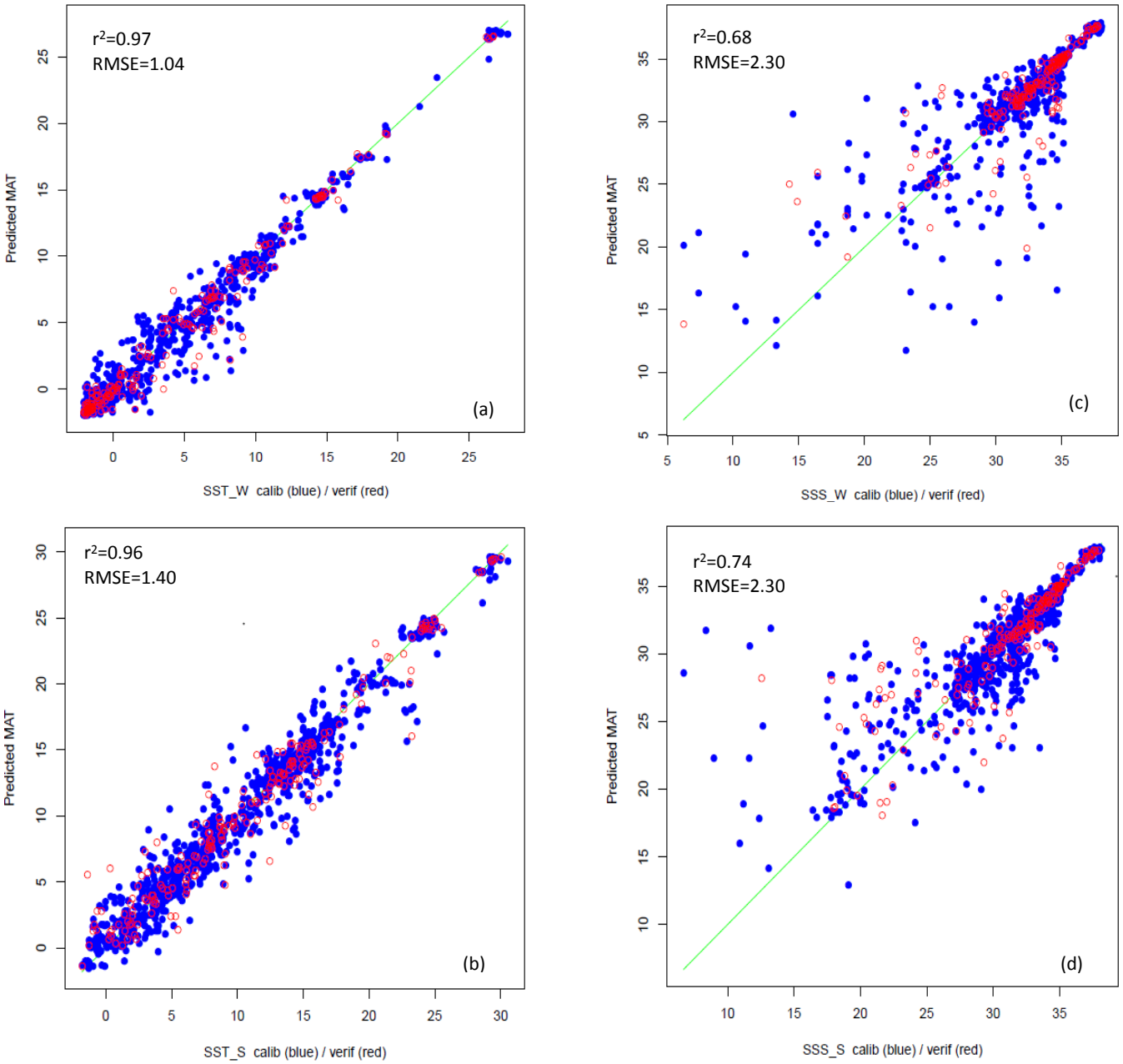

Fig. 16: Validation test results using MAT. These show winter and summer sea-surface temperatures (SSTs) (a, b) and sea-surface salinities (SSSs) (c, d) for the Chiba composite section. Calibration datasets are plotted as blue dots. Validation datasets plotted as red circles.

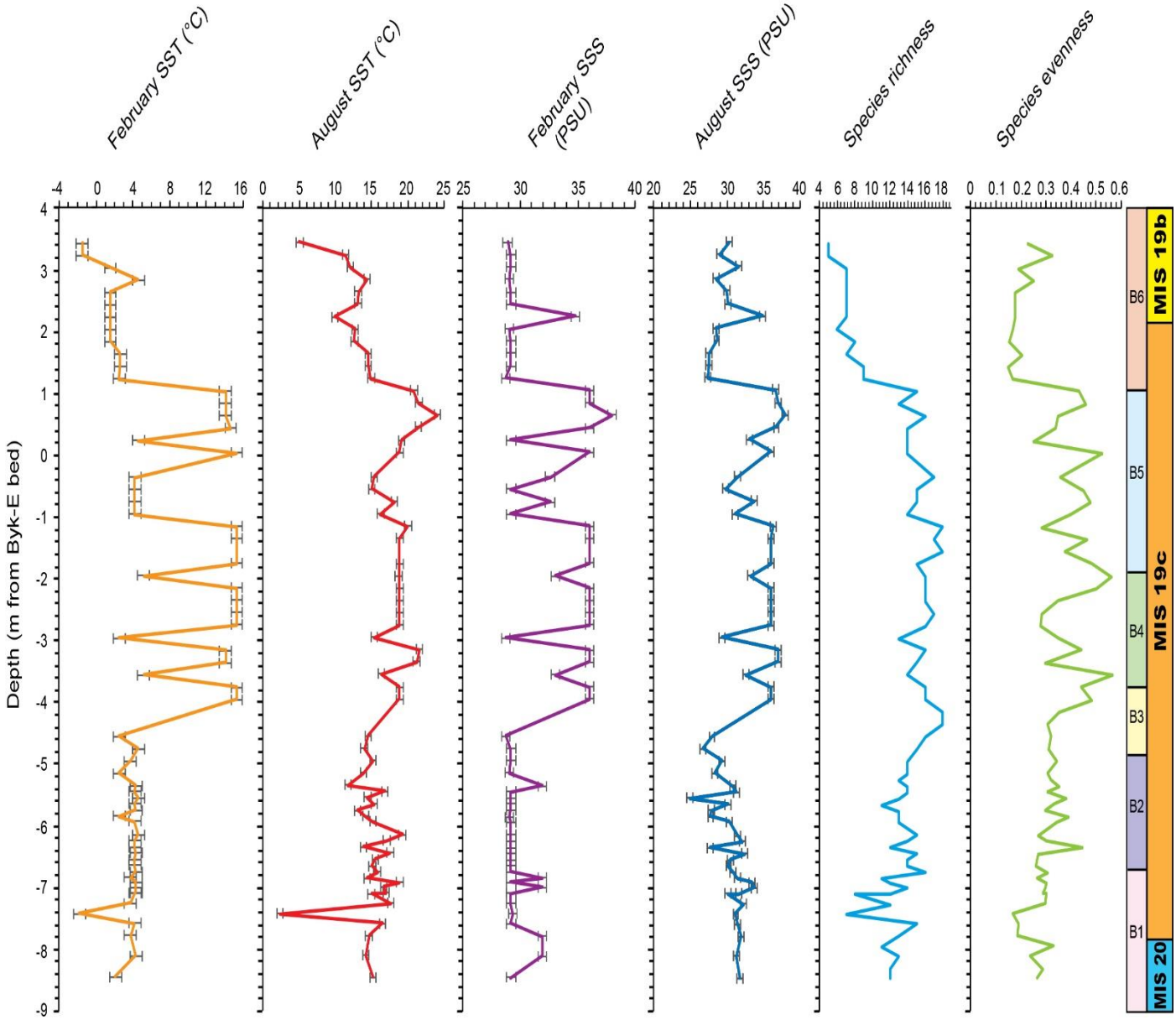

Fig. 17: MAT-based sea-surface temperature (SST) in °C and salinity (SSS) in psu for months of February and August based on dinoflagellate cysts from the Chiba composite section (this study), plotted against depth. The error bars are explained in Chapter 4. Species richness and evenness shows number of taxa and their distribution per sample respectively. Biozones 1–6 are based on constrained cluster analysis (this study). MIS stages and substages are from Suganuma et al. (2018).

5.3.2 Species richness and evenness

Species richness is the number of species occurring in each sample. From -8.5 m to -4.5 m below the Byk-E bed, where Termination 19 occurs, species richness steadily increases upsection from 12 to 18 taxa/sample, although with a brief decrease to ~7–8 taxa/sample at about -7 m before increasing again. The average species richness for the entire interval is 15 taxa/sample. The highest species richness was recorded in MIS 19c with a maximum of 18 taxa (Fig. 17). There is an abrupt dramatic decrease in species richness (5–9 taxa/sample) at about 1 m above the Byk-E bed, which is notably due to a sharp increase and sustained rise in the abundance/dominance of *Protoceratium reticulatum*.

This study also considers how even the dinoflagellate cyst taxa are distributed in each sample (Fig. 17). This is known as species evenness. It takes into account the proportion and distribution of each species in a sample with no sensitivity to species richness. High species evenness occurs in a sample when all taxa share the same abundance and are equally distributed. The higher the values in a sample, the more even the dinoflagellate cyst taxa in the sample. Further explanation and measurement metrics of evenness is presented in chapter 4 above. None of the samples yielded species evenness of 1, which is generally known as the highest possible value that can be attained. Starting from the bottom of the interval at a depth of -8 m, species evenness gradually increases from 0.26 to a maximum of 0.56 at -3.55 m below the Byk-E bed, although with a brief drop to 0.19 at about -7 m before rebounding. The greatest evenness recorded, ranging from 0.30 to 0.56, coincides with the peak of MIS 19. However, it decreases to 0.16–0.22 at the top of the interval starting from ~1 m above the Byk-E bed.

5.3.3 Cluster analysis and dinocyst assemblage biozonation

Constrained cluster analysis based on presence/absence was used to produce a dinoflagellate cyst (dinocyst) assemblage biozonation for descriptive and biostratigraphic purposes. Six biozones, numbered in ascending order, are recognized from the dendrogram and shown in Fig. 18. These biozones are shown also relative to the species compositions of each sample (Fig. 10). The biozonation shows some correspondence to the concentration of dinocysts, which is therefore included in the description of the biozones. The dinocyst assemblage biozones are described below.

1. **Dinocyst assemblage biozone 1: TB 90–70 (-8.45 to -6.85 m; 791–787 ka)**

This biozone correlates with Termination IX and is significant because of the dominance of *Brigantedinium* spp. (43–92%). Its highest relative abundance is recorded in this biozone. *Achomosphaera*/*Spiniferites* spp. total, *Spiniferites hyperacanthus*/*mirabilis* and *Spiniferites* sp. 2 increases significantly, ranging from 3 to 29%. This increase is briefly interrupted by a sudden decrease in the abundance of both taxa at -7.5 m. The other species recorded here remain relatively stable in abundance. They include *Protoperidinium nudum* (1–10%), *Selenopemphix nephroides* (1–6%), and the neritic autotrophs such as *Spiniferites* sp. 1 (0–1%), *Achomosphaera*/*Spiniferites* spp. indet. (0–2%), cysts of *Protoceratum reticulatum* (0–7%), *Lingulodinium machaerophorum* (0–2%), *Operculodinium israelianum* (0–3%), *Nematosphaeropsis labyrinthus* (0–0.6%), and oceanic water-mass indicators including *Impagidinium patulum,* and *I. aculeatum,* (0–0.6%). Note that *Tuberculodinium vancampoae, Pyxidinopsis reticulata*, *Xandarodinium xanthum*, cysts of *Scrippsiella trifida* and *I. sphaericum* are absent from this biozone. Dinocyst concentrations fluctuate from ~1000 to 3000 cysts/g.

2. Dinocyst assemblage biozone 2: TB 66–50 (-6.75 to -4.95 m; 787–783 ka)

Brigantedinium spp. (25–46%), *Achomosphaera*/*Spiniferites* spp. total (22–67%) and *Spiniferites* sp. 1 (14–45%) record high abundances in this biozone. *Achomosphaera*/*Spiniferites* spp. total and *Spiniferites* sp. 2 steadily increase upsection while *Brigantedinium* spp. on the other hand decreases, as shown in Fig. 15. It is noteworthy that *Tuberculodinium vancampoae* (0–0.6%) and cysts of *Scrippsiella trifida* (0–2%) have their lowest occurrences in this biozone. Other species recorded in this biozone include: cysts of *Protoperidinium nudum* (6–18%), *Selenopemphix nephroides* (1–6%), and the autotrophs *Spiniferites hyperacanthus*/*mirabilis* (2–9%), *Spiniferites* sp. 1 (1–18%), *Spiniferites* sp. 2 (14–45%), *Achomosphaera*/*Spiniferites* spp. indet. (0–12%), cysts of *Protoceratum reticulatum* (4–14%), *Lingulodinium machaerophorum* (0.3–3%), *Operculodinium israelianum* (0–2.9%), *Nematosphaeropsis labyrinthus* (0–0.6%), *Impagidinium patulum*, and *I. aculeatum*, (0–1%). Note that *Pyxidinopsis reticulata*, *Xandarodinium xanthum* and *I. sphaericum* are absent from this biozone. Dinocyst concentrations fluctuate from ~500 to 4000 cysts/g.

3. Dinocyst assemblage biozone 3: TB 48–40 (-4.75 to -3.95 m; 783–781 ka)

Although this biozone has the shortest range of all the biozones, it bears the highest relative abundance of *Achomosphaera*/*Spiniferites* spp. indet. (24–45%) and *Spiniferites* sp. 2 (14–45%) taxa. The lowest occurrence of *Pyxidinopsis reticulata* (0.6%) and *Xandarodinium xanthum* (0.3–1.6%) occurs in this biozone. *Brigantedinium* spp. continue to decrease in this biozone upsection, recording slightly lower abundances (17–34%) than for Biozones 1 and 2. However, the other dinocysts recorded here are somewhat stable and do not change much in their relative abundance. They include cysts of *Protoperidinium nudum* (10–20%), *Selenopemphix nephroides* (0–1%), and the autotrophs *Spiniferites hyperacanthus*/*mirabilis*

(2–5%), *Spiniferites* sp. 1 (1–18%), *Protoceratum reticulatum* (5–11%), *Operculodinium israelianum* (1–3%), *Tuberculodinium vancampoae* (0–0.6%), *Nematosphaeropsis labyrinthus* (0–4.3%), *Impagidinium patulum, I. aculeatum,* (0–0.9%), and the cysts of *Scrippsiella trifida* (0–1.6%). *I. sphaericum* is absent from this biozone. Here *Achomosphaera*/*Spiniferites* spp. total slightly decreases in abundance (65–46%) and the sudden increase in the relative abundance of *Lingulodinium machaerophorum* begins in this biozone. Dinocyst concentrations remain stable in this zone at ~1000–2000 cysts/g.

4. Dinocyst assemblage biozone 4: TB 38–22 (-3.75 to -2.15 m; 780–777 ka)

It is noteworthy that *Lingulodinium machaerophorum*, which shows a sudden increase in Biozone 3, peaks in this biozone, rising up to 47% from 19% before decreasing to 5% at about -2 m. This sudden but brief increase in *Lingulodinium machaerophorum* makes this biozone very significant. While *Lingulodinium machaerophorum* is dominant in this biozone, there is a corresponding decrease in the abundance of *Achomosphaera*/*Spiniferites* spp. total (28%), *Spiniferites* sp. 2 (8%) and the cysts of *Protoperidinium nudum* (5%). This biozone also consists of *Brigantedinium* spp. (8–15%), *Selenopemphix nephroides* (0–0.9%), *Xandarodinium xanthum* (0–1%) and the autotrophs *Spiniferites hyperacanthus*/*mirabilis* (3–18%), *Spiniferites* sp. 1 (3–10%), *Achomosphaera*/*Spiniferites* spp. indet. (3–10%), *Protoceratum reticulatum* (4–12%), *Operculodinium israelianum* (1–4%), *Tuberculodinium vancampoae* (0–0.8%), *Nematosphaeropsis labyrinthus* (0–1%), *Impagidinium patulum, I. aculeatum* (0–0.8%), *Pyxidinopsis reticulata* (0–1%), and the cysts of *Scrippsiella trifida* (0.2–1%). *I. sphaericum* is absent from this biozone. Generally, the abundance of most of the dinocysts in this biozone is relatively stable. The dinocyst concentration ranges from ~1000 to 2000 cysts/g.

5. Dinocyst assemblage biozone 5: TB 20 – TB2 26 (-1.95 to 1.0 m; 776–773 ka)

Almost all species recovered are represented in this biozone. This biozone is characterized by increase in the abundance of *Achomosphaera*/*Spiniferites* spp. total (32–63%), *Spiniferites* sp. 2 (16–47%), *Lingulodinium machaerophorum* (12–33%) and *Brigantedinium* spp. (14–37%). Other species occurring in this biozone are: heterotrophs including cysts of *Protoperidinium nudum* (2–22%), *Selenopemphix nephroides* (0–1.8%), and *Xandarodinium xanthum* (0.4–2.2%); and the autotrophs *Spiniferites hyperacanthus*/*mirabilis* (4–19%), *Spiniferites* sp. 1 (1–18%), *Achomosphaera*/*Spiniferites* spp. indet. (3–24%), *Operculodinium israelianum* (0–3%), *Tuberculodinium vancampoae* (0–4%), *Nematosphaeropsis labyrinthus* (0.3–0.6%), *Impagidinium patulum, I. aculeatum, I. sphaericum* (0.3–1%), *Pyxidinopsis reticulata* (0–0.5%), and cysts of *Scrippsiella trifida* (0–1%). The end of this biozone marks a dramatic decrease in species richness due to a decrease in relative abundance of almost all the species at the end of the zone and the highest occurrences of such species as *Pyxidinopsis reticulata*, *Scrippsiella trifida*, and *Impagidinium aculeatum*. *Impagidinium sphaericum* occurs only in this biozone. Dinocyst concentrations range from ~1000 to 4000 cyst/g. It is noteworthy that the Byk-E bed falls within this biozone.

6. Dinocyst assemblage biozone 6: TB2 24 – TB2 02 (1.2–3.4 m; 772–770 ka)

This biozone is characterized by high abundances of *Protoceratium reticulatum* (81–93%). The beginning of this biozone marks a sharp decrease in species richness. This is because the relative abundance of *Protoceratum reticulatum* increases drastically from ~17% to ~93%. Accordingly, many species are either not recorded in this biozone or found in low abundances due to the dominance of *Protoceratium reticulatum* (Fig. 17). Other species recorded in this biozone, although in low abundances include; *Brigantedinium* spp. (0–0.9%), cysts of *Protoperidinium nudum* (0–2%), *Selenopemphix nephroides* (0.3%), *Spiniferites hyperacanthus*/*mirabilis* (0–1%), *Spiniferites* sp. 1 (3–18%), *Spiniferites* sp. 2 (0–4%),

Achomosphaera/*Spiniferites* spp. indet. (0–1%), *Lingulodinium machaerophorum* (0.3–4.6%), *Tuberculodinium vancampoae* (0.3%), *Achomosphaera*/*Spiniferites* spp. total (4–21%), *Nematosphaeropsis labyrinthus* (0.3–0.6%), and *Impagidinium patulum* (0.3%). This zone records the highest cyst concentrations (26,000–315,000 cysts/gram), mainly because of the exceptionally high abundance of *Protoceratum reticulatum*. This zone is significant because its base occurs ~1 m above the Byk-E bed and almost exactly coincident with the Matuyama–Brunhes boundary.

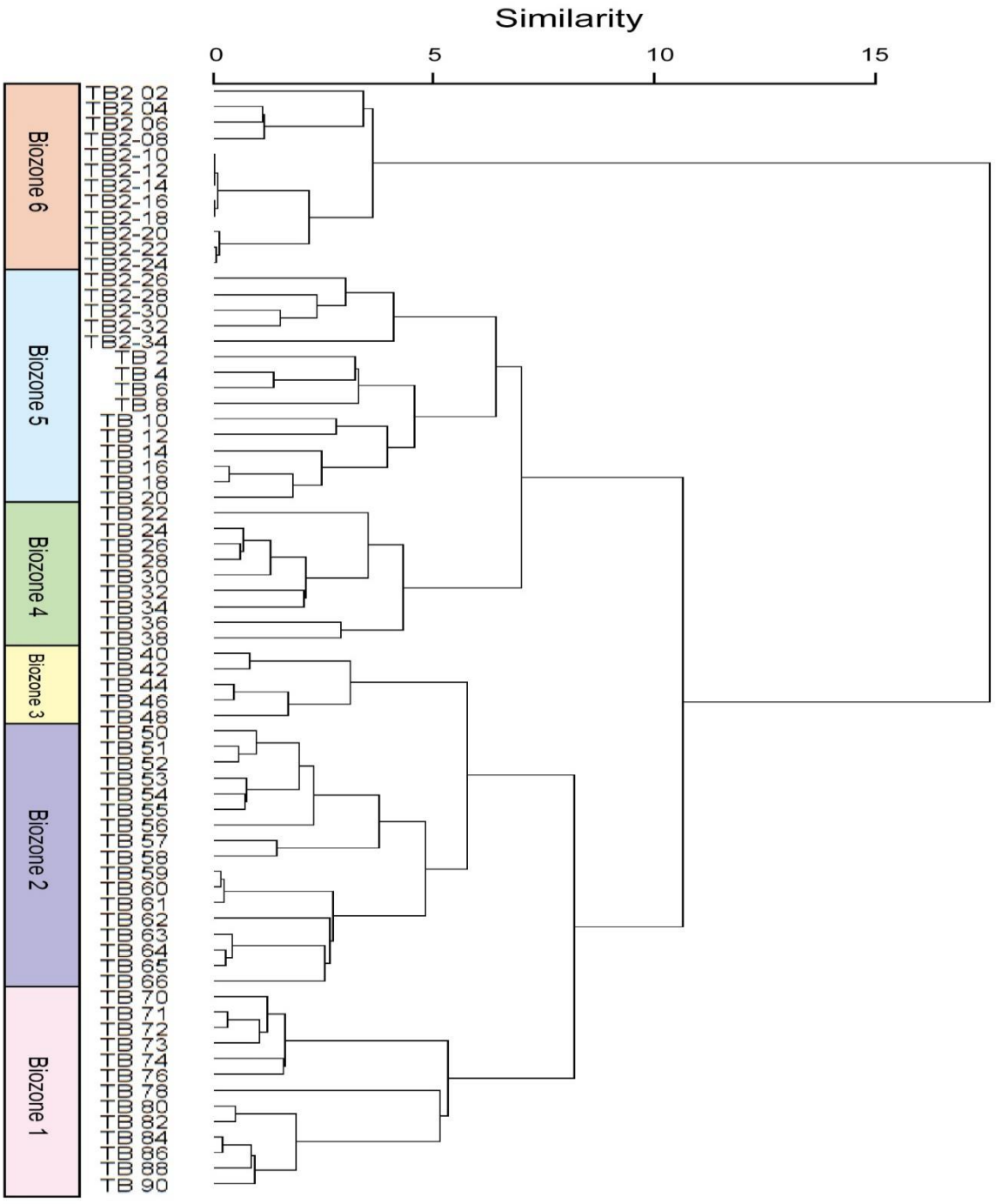

Fig. 18: Dendrogram from constrained cluster analysis, based on the presence/absence of taxa, showing six dinocyst assemblage biozones from the study interval in the Chiba composite section.

CHAPTER SIX

6.0 DISCUSSION

6.1 Paleoceanographic and paleoclimatic history of the Chiba section

The focus of this study is to examine in detail paleoceanographic changes in the western Pacific Ocean during MIS 19 in the Chiba section. Studies conducted in the Boso Peninsula using benthic and planktonic foraminifera, radiolarians, diatoms, and stable isotopes from late MIS 20 to early MIS 18 (e.g. Suganuma et al., 2017; 2018 and references therein) reveal paleoceanographic instability influenced by the oscillation of the Kuroshio and Oyashio currents. Examining the dinocyst record enhances our understanding of paleoceanographic changes in the western Pacific Ocean. To this end, the dinocyst record reflects changes in the surface waters. The dinocyst record is here calibrated to the age model of Suganuma et al. (2018) and is discussed relative to the six assemblage biozones described in Chapter 5. The ranges of important species plotted using the Suganuma et al. (2018) age model are given in Figures 19, 20, and 21.

Biozone 1 (791–787 ka) spans Termination IX and shows high abundances of heterotrophic (protoperidinoid) cysts, particularly *Brigantedinium* spp. (60–95%) although *Selenopemphix nephroides* attains its highest abundance in this biozone with a maximum of 12%, suggesting relatively high productivity and nutrient levels at this time. It is noteworthy that both *Brigantedinium* spp. and *Selenopemphix nephroides* begin to decline in abundance in the middle of the zone around 789 ka with a corresponding increase in the abundance of autotrophic taxa including *Spiniferites hyperacanthus*/*mirabilis*, *Spiniferites* sp. 2, and total *Achomosphaera*/*Spiniferites* spp. This suggests a gradual slight decline in nutrient levels in the surface waters during Termination IX. It also shows the onset of warm conditions (deglaciation) and a transition from the cold, nutrient-enriched waters of MIS 20 to warm

conditions in MIS 19. Cysts produced by heterotrophic dinoflagellates, particularly of the genus *Protoperidinium*, usually dominate dinocyst assemblages in high productivity areas (e.g., Dale, 1996; de Vernal et al., 2007; Devillers and de Vernal., 2000), and changes in the relative abundances of dinocysts produced by heterotrophic dinoflagellates have been used to estimate primary production associated with changing nutrient conditions lower in the Quaternary (e.g., Lewis et al., 1990; Radi et al., 2007; Kim et al., 2010). In the present study, their decline and particularly that of *Brigantedinium* spp., seems to signal a gradual displacement of the cold nutrient-rich Oyashio Current by the warm nutrient-poor Kuroshio Current. Notably, the steady increase in the relative abundance of total *Achomosphaera*/*Spiniferites* spp., *Spiniferites hyperacanthus*/*mirabilis*, and *Spiniferites* spp. 2 in this biozone (MIS 20/19 transition) is interrupted by a sudden but brief drop in their relative abundance to about 1–4%. Although based on a single sample, this suggests that the gradual warming was interrupted by a sudden but brief cooling during Termination IX at about 790 ka (Figs. 19 and 20). This brief drop in relative abundance might also be a result of taphonomic influence on the single sample that likely represent an event, a moment in time, rather than a sustained change in the hydrography. In this case, care should be taken when interpreting because it is safer not to put too much emphasis on a single sample that could be the result of some taphonomic processeses. This cooling event is also captured by the MAT-based dinocyst SST (February and August) reconstruction where temperatures dropped to -2°C in February and 2°C in August at ~790 ka (Fig. 19). This cooling event occurs 1 kyr after a Younger-Dryas-like event as registered in the pollen record (drop in broadleaved/arboreal pollen ratio) and in heavier benthic isotopes from the same sample set (Suganuma et al., 2018). Analysis of this interval at higher sampling resolution would be needed to fully resolve this delay, although the dinocyst record seems to reflect oceanographic instability during the transition from MIS 20 to 19. More generally, the

benthic and planktonic foraminiferal $\delta^{18}O$ signals, planktonic foraminiferal abundance, *Florisphaera profunda* abundance, Mg/Ca temperatures based on *Globorotalia inflata*, and the concentration of radiolarians, all provide evidence of changing oceanography during the MIS 20/19 transition (Termination IX) (see Figs. 19 and 20). In particular, cold-water radiolarian species (e.g. *Lithomelissa setosa* and *Stylochlamydium venustum*) registering temperatures between 12° and 18°C were found to decrease in abundance during Termination IX as warm-water species increased, reflecting a weakening of the Oyashio (cold) current at the Chiba site at this time (Suganuma et al., 2018). The deglaciation that marks the MIS 20/19 transition is best explained by an increase in June insolation (Suganuma et al., 2018; Fig. 20).

The start of **Biozone 2 (787–783 ka)** marks the onset of full interglacial conditions as indicated by the pollen record (Suganuma et al., 2018). There is a continued progressive decline in the relative abundance of *Brigantedinium* spp. and total heterotrophs, which presumably signals a continued weakening of the Oyashio (cold) current and northward migration of a strengthened subtropical Kuroshio Current. Otherwise, there is neither an obvious warming signal within the dinocyst assemblages nor an increase in the MAT reconstructed temperature for August. It appears that the cyst record is not particularly sensitive to the changes that were evidently occurring during the interval of time represented by Biozone 2 including the onset of full interglacial conditions at ~787 ka. Annual mean sea surface temperature (SST) reconstructed by Suganuma et al. (2017) for the Chiba section using planktonic foraminiferal transfer function PFJ-125 (Takemoto and Oda, 1997) shows temperature ranging from 16.8 to 21.5 °C for MIS 19c. This compares with August SST estimates of around 16°C based on the dinocyst MAT.

Biozone 3 (783–780 ka) is marked at its base by a rise in *Lingulodinium machaerophorum* (Fig. 19, 20) that coincides with a brief but prominent drop in broadleaved trees reported by

Suganuma et al. (2018) in the middle of MIS 19c in the Chiba composite section (see Fig. 20). It suggests a hydrological change related to brief cooling on land. It is not until the middle of Biozone B3 (~781 ka) that increases in species richness, evenness, August SST and August SSS reach maximum interglacial levels, and these are maintained to the top of Biozone 5 (773 ka). The onset of full interglacial conditions as reflected in the dinocyst record at ~781 ka is therefore delayed relative to the onset at ~787 ka based on the pollen record.

Lingulodinium machaerophorum reaches a peak of ~43% in **Biozone 4 (780–776 ka)** after the recovery of broadleaved trees and a return to fully interglacial conditions. Because *Lingulodinium machaerophorum* today is related to elevated nutrient levels (Dale, 1996), this probably explains also its abundance in Biozone 4. Towards the end of Biozone 4, *Lingulodinium machaerophorum* declines and *Spiniferites hyperacanthus/mirabilis* increases, suggesting a slight rise in summer SST that might be related to the lightest benthic isotopic values recorded in MIS 19c and occurring just before the end of fully interglacial conditions. *Spiniferites hyperacanthus/mirabilis* reaches peak abundances of just over 20% at the start of **Biozone 5 (776–773 ka),** reflecting the prevalence of full interglacial conditions and influence of the warm Kuroshio Current at the Chiba site during MIS 19c. Notably, the dinocyst August SSTs based on MAT (Fig. 20) reached values of around 19°C in the early part of this biozone. The radiolarian sea-surface temperature index (Tr ratio) derived by Suganuma et al. (2018) (see Fig. 20) and based on the ratio of warm- to cold-water radiolarian species, and a reliable proxy for the Kuroshio (high value) and Oyashio (low value) currents at this site, attains its peak (high value) at this same point. This provides strong indication that the Kuroshio Current persisted at the Chiba site at least until around 775 ka after which *Spiniferites hyperacanthus/mirabilis* declined at the end of full interglacial conditions as determined from the pollen record. Suganuma et al. (2017) also recorded high

abundances of warm-water radiolarian species including *Dictyocoryne* spp., *Didymocyrtis* spp. and *Tetrapyle* spp. during MIS 19c in the Chiba composite section. Matsuzaki and Itaki (in press) noted that higher abundances of these groups of radiolarian species occur presently in the Kuroshio Current where sea-surface temperatures range between 20° and 29°C, further supporting the evidence deduced from the dinocyst record.

Biozone 6 (773–770 ka), which spans the MIS 19c/b transition, is marked by a striking change at its base that coincides with the Matuyama–Brunhes boundary at 772.9 ka. There is a sharp decrease in species richness and evenness, and an abrupt and sustained rise to dominance of *Protoceratium reticulatum* (Figs. 19–21). This sudden rise of *Protoceratium reticulatum* to dominance coincides with a dramatic increase in dinocyst concentrations as shown in Fig. 19. The increase in dinocyst concentrations reflects a rise in surface-water productivity, and the dominance of *Protoceratium reticulatum* cysts is of particular significance. This is an extant cosmopolitan species that tolerates a wide range of temperatures and salinities (Rochon et al., 1999; Zonneveld et al., 2013) but is particularly associated with the North Atlantic Current (Hennissen et al., 2017) which is characterised by unstable surface waters and moderately elevated nutrient levels. This species is also common today at the convergence of oceanic and neritic water masses (Dale and Dale, 2002), and highest abundances today (up to 91%) are found in the temperate to subpolar North Atlantic (as *Operculodinium centrocarpum* in Zonneveld et al., 2013). Today around Japan, *Protoceratium reticulatum* cysts typically occur with abundances of less than ~20%, and the nearest location where this value is exceeded is the Bering Sea, where abundances of 40–60% are recorded (Zonneveld et al., 2013). MAT reconstructions give August SSTs around 24–20°C at the top of Biozone 5, dropping to just 5°C at the top of Biozone 5, with a brief warming to ~14°C at ~771 ka. Reconstructed salinities similarly show a sharp drop from 37 psu at the top of Biozone 5 to just 27 psu at the base of Biozone 6 (Chapter 5). These

estimates are based on a Northern Hemisphere calibration set that is weighted towards higher latitude sites (Chapter 4). While August SSTs as low as 5°C for the top of Biozone 6 are probably not realistic, an overall signal of cooling and reduced salinity for Biozone 6 seems plausible.

The rapid rise to an overwhelming dominance of *Protoceratium reticulatum* is interpreted to represent an abrupt southward shift of the Subarctic Front leading to the predominant influence of the subarctic Oyashio Current at the Chiba site. This was a major paleoceanographic shift, and while it occurred about 1000 years after the end of full interglacial conditions as determined by the broadleaved/arboreal pollen index, it does correspond to a brief sharp drop in this index (and also the *Quercus*/AP index of Suganuma et al., 2018, fig. 13) and hence a decline in terrestrial temperatures (Fig. 20). This sharp signal is not conspicuous in other marine proxies, although few have the high sampling resolution of the present study. Nonetheless, general trends across this interval are seen, for example, in a decline in Mg/Ca-based (*Globorotalia inflata*) SST and a shift to heavier isotopic values for the cool-temperate planktonic foraminifera *Globigerina bulloides* and *G. inflata*. Interestingly, planktonic foraminiferal assemblage data show a decline in the abundance of the warm-temperate *Globigerinoides ruber* and *Pulleniatina obliquiloculata*, followed by rise in the factor loading associated with the subtropical Kuroshio Current at ~770 ka which occurs just after the end of the dinoflagellate cyst record. High factor loadings for the subtropical Kuroshio Current continue for the remainder of MIS 19 and into MIS 18 (Fig. 21; Suganuma et al., 2018, fig. 9). Suganuma et al. (2018) interpreted the foraminiferal data as evidence of a northward shift of the subtropical Kuroshio Current at ~770 ka which they attributed to a weakening of the East Asian Winter Monsoon. If correct, this would reduce the duration of influence of the subarctic Oyashio Current to a brief interlude between 773 and ~770 ka. It is not possible to test this hypothesis in the present study because the

dinoflagellate data do not extend to 770 ka. However, a northward shift of the Kuroshio Current would presumably reverse the dominance of *Protoceratium reticulatum*, so could be easily tested. Future investigations extending the dinocyst record a few metres above the studied interval, into early MIS 18, are needed to provide a better understanding of the paleoceanography of this part of the Chiba composite section.

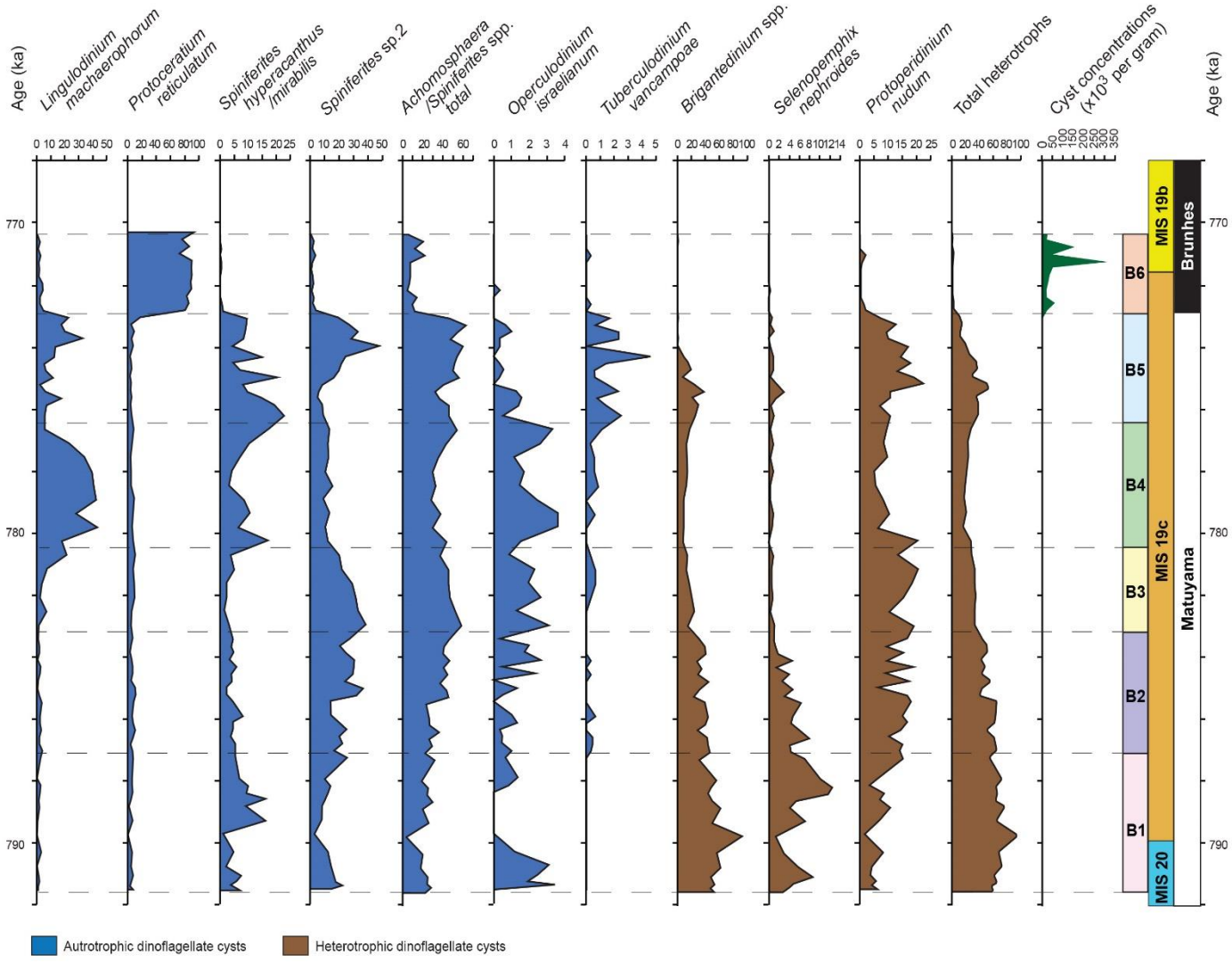

Fig. 19: Relative abundance of important autotrophic and heterotrophic dinoflagellate cyst species with total heterotrophs and cyst concentration, all reflecting changes in the surface waters of the western Pacific Ocean. The ages, MIS stages, and substages all follow

Suganuma et al. (2018). The six assemblage biozones are based on constrained cluster analysis (Chapter 5), each reflecting significant changes as discussed in the text.

6.2 Taphonomy

Terrestrial spores and pollen in marine sediments provide taphonomic information, and may be useful for reconstructing terrestrial vegetation. In the present study, pollen and spores were attributed only to a few broad taxonomic groups (Fig. 22), yet the results show distinct paleoclimatic changes and a strong terrestrial influence in the Chiba section throughout MIS 19. In particular, the total sporomorphs have a strong influence in MIS 19c, with a maximum of 83% of the total palynomorphs registered at 774 ka. However, there is slight decrease at ~784 and a sharp drop at 773 ka. They reflect transport from the coast, since their source is mostly coastal vegetation and fluvial input (McCarthy et al., 2003). The entire interval is dominated by bisaccate pollen (*Pinus*, *Picea*, *Abies*; up to 67% of the total sporomorphs) with no significant changes throughout the interval (Fig. 15). *Pinus* is likely to be taphonomically overrepresented, as is often the case in open marine settings, reflecting long distance transport from the coast and hence distal sedimentation at this site (Onishi, 1969; Okuda et al., 2006). It is known to be predominant in deep-sea sediments off the Japanese archipelago today (Heusser, 1990). Although the pollen in the present study was assigned only to broad taxonomic groups and distinctive taxa, results agree with the detailed stratigraphic distributions reported in Okuda et al. (2006) and Suganuma et al. (2018). In particular, the sharp decrease in the abundance of *Tsuga* and the corresponding increase in angiosperm pollen (deciduous broadleaved trees) at Termination IX (~791–786 ka) (Fig. 15 and 22) shows a transition from glacial MIS 20 to interglacial MIS 19 while the rebounding of *Tsuga* to higher abundance at MIS19b possibly points to the onset of MIS 18 glacial conditions. MIS 19c consist of high abundance of arboreal angiosperm pollen (*Quercus*, *Fagus*, *Juglans,* etc.) with corresponding low occurrence of *Tsuga*, a period marked by vegetation of warm-

temperate deciduous broadleaved forest, which is presently dominant in the northeastern part of the Japanese archipelago (Fig. 1c).

Among the dinocysts, it must be assumed given the continental slope setting that some long-distance transport occurred, although little evidence of reworking or long-distance transport was in fact observed. Protoperidiniacean taxa are particularly susceptible to oxidation and therefore underrepresentated (Zonneveld et al., 2001; Versteegh and Zonneveld 2002), although the presence of pale, partially oxidised specimens usually provides some indication of loss. No evidence of oxidation was seen in the present study.

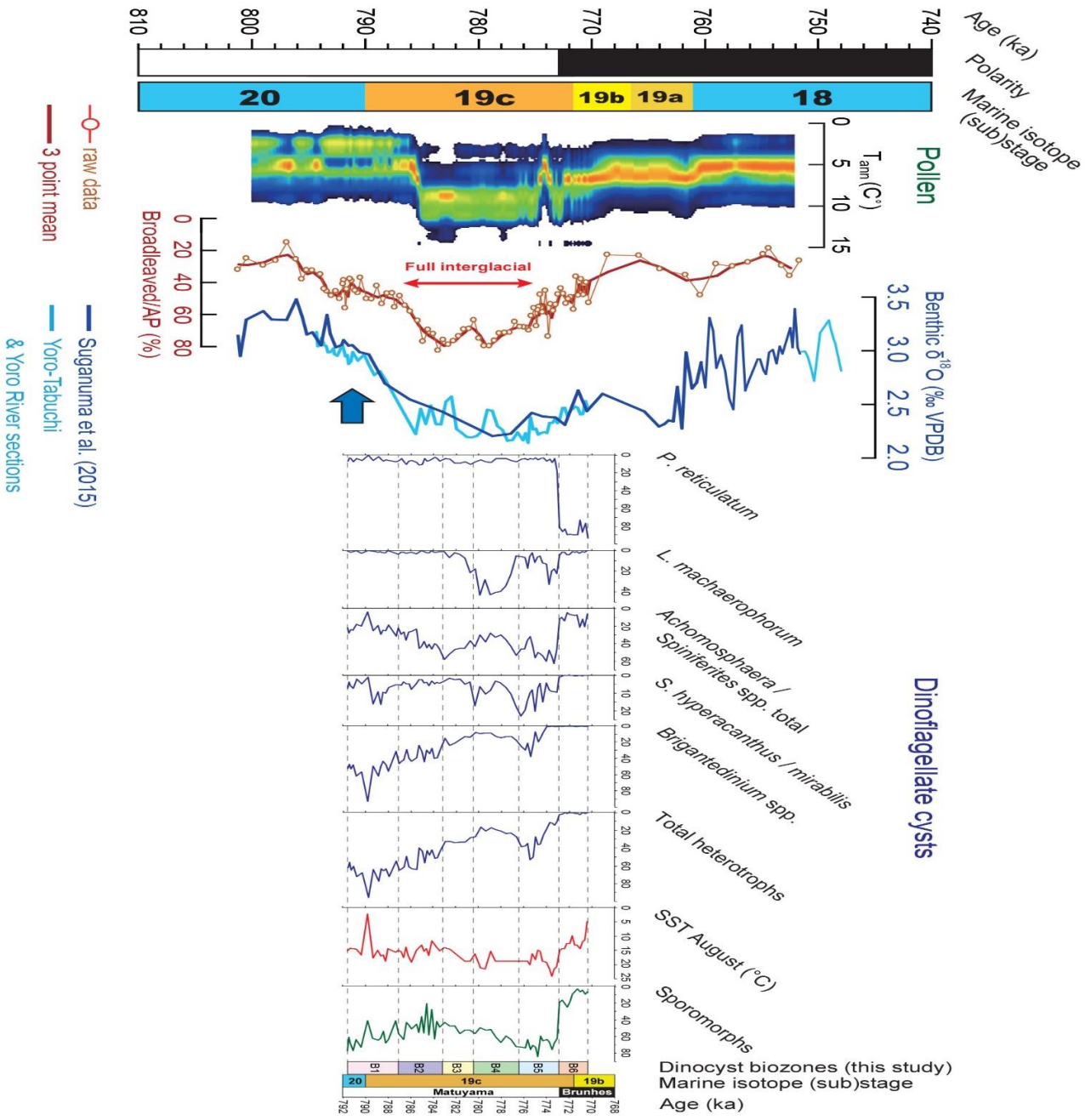

Fig. 20: Chiba composite section showing relative abundances of selected dinoflagellate cyst taxa and total heterotrophs as percentages of the total dinocyst count, and August sea surface temperatures reconstructed from the dinocyst record (MAT) (this study). Sporomorph abundances are expressed as percentages of the total palynoporphs (this study). These results are compared with records from Suganuma et al. (2018, fig. 11) showing benthic $\delta^{18}O$, Broadleaved/AP, and Pollen T_{ann}(°C). Dinocyst biozones 1–6 are based on constrained cluster analysis (Chapter 5). Blue arrow marks the suggested position of the Younger Dryas-type cooling event. Age and MISs are from Suganuma et al. (2018). The duration of full interglacial conditions is from Suganuma et al. (2018) and based on pollen assemblage composition.

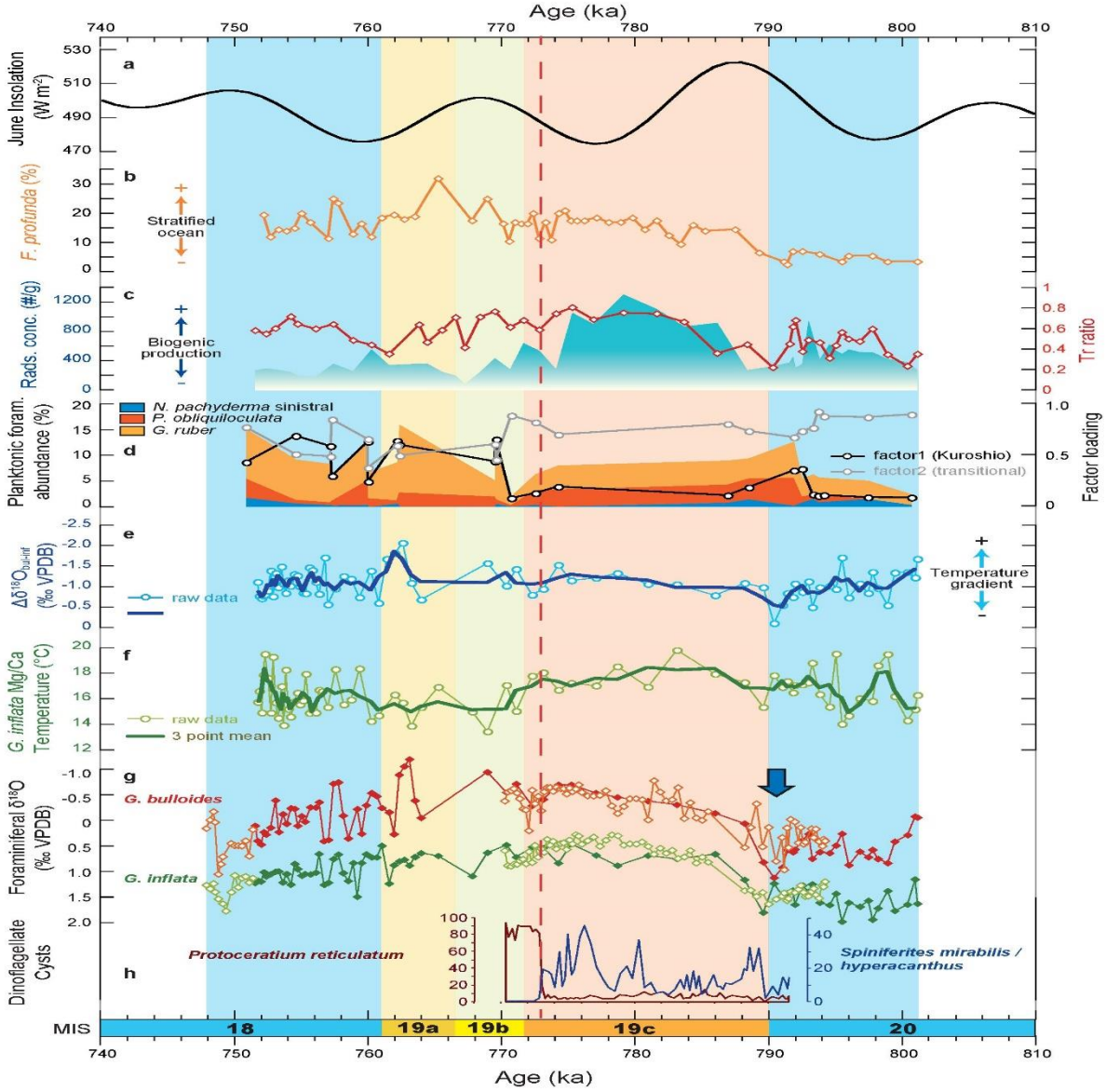

Fig. 21: Various paleoclimatic/paleoceanographic proxies from the Chiba composite section. (a) 65°N insolation in June. (b) Relative abundance of *Florisphaera profunda*. (c) Radiolarian concentrations and radiolarian sea-surface temperature index (Tr ratio). (d) Relative abundance of planktonic foraminifera and factor loadings. (e) $\Delta\delta^{18}O_{G.\ bulloides\_G.\ inflata}$ (bul-inf), temperature gradient for surface and subsurface waters. (f) Mg/Ca paleotemperature for *Globorotalia inflata* (T_{inf}). (g) planktonic $\delta^{18}O$ records (*Globigerina bulloides* and *Globorotalia inflata*). (from Suganuma et al., 2018, fig. 13). (h) Selected dinoflagellate cyst data (this study, as a percentage of the total dinocysts) showing the drop in the abundance of *Spiniferites mirabilis*/*hyperacanthus* at ~790 ka just following the Younger Dryas-type cooling event (indicated by blue arrow), and a dramatic rise dominance of *Protoceratium reticulatum* at 773 ka. Age model is from Suganuma et al. (2018).

6.3 Lead-lag relationships and duration of full interglacial conditions in the Chiba section

It is important to examine different proxies in a section because each has its own response to environmental/climate change. The duration of full interglacial conditions is particularly significant for MIS 19 because of its similarities to the present interglacial (Tzedakis et al. 2012). The onset of full interglacial conditions in the Chiba composite section can be measured in different ways. The benthic foraminiferal $\delta^{18}O$ record is orbitally tuned with MIS 19 (and hence MIS 19c) beginning at 790 ka. Planktonic foraminiferal $\delta^{18}O$ values for both *Globigerina bulloides* and *Globorotalia inflata*, Mg/Ca temperatures based on *Globorotalia inflata*, and increasing radiolarian production, all indicate a significant increase in sea surface temperature between 788 and 786 ka, which coincides with the peak in insolation for June at 65°N (Suganuma et al., 2018; Fig. 21). An increase in the abundance of *F. profunda* also signifies an increase in stratification of the water column at this time.

The onset of full interglacial conditions in the terrestrial record has been dated at 785.0 ka based on the pollen record (Suganuma et al., 2018; Fig. 20). The terrestrial threshold to interglacial conditions is therefore reached about 1–2 kyr after the rapid warming (788–786 ka) indicated by marine proxies.

The dinocyst record reflects the onset of full interglacial conditions somewhat gradationally. An increase in *Spiniferites mirabilis/hyperacanthus* at ~790 ka seems to be one response to warming of surface waters with the onset of MIS 19c. However, species richness and evenness and MAT-based August SST and SSS (Fig. 17), all show a synchronous stepped increase in the upper part of biozone 3 (~782 ka) that persists to the top of Biozone 5 (~773 ka). The dinoflagellates therefore seem to have responded to different thresholds than other marine proxies for the onset of full interglacial conditions.

Regarding the termination of full interglacial conditions, the dinocyst record seems to be unambiguous and is marked by a clear break to cooler conditions at the beginning of Biozone 6 at ~772 ka., in coincidence with a drop in Mg/Ca temperatures based on *G. inflata* and with the end of MIS 19c (Suganuma et al. 2018). The pollen record gives a slightly earlier termination at 775.1 ka according to Suganuma et al. (2018) although the termination is somewhat gradational (Fig. 20).

The duration of full interglacial conditions at the Chiba composite section is around 15 kyr (787–772 ka) based on marine proxies, and ~10 kyr (785.0–775.1 ka) based on the vegetational (pollen) record (Suganuma et al., 2018). These estimates compare favourably with the duration of full interglacial conditions elsewhere including between 14 and 20 kyr at the Montalbano Jonico site in Italy (Marino et al., 2015; Maiorano et al., 2016), and a ~11–12 ka duration for interglacial conditions at IODP Site U1313 in the central North Atlantic (Ferretti et al., 2015; Emanuele et al., 2015).

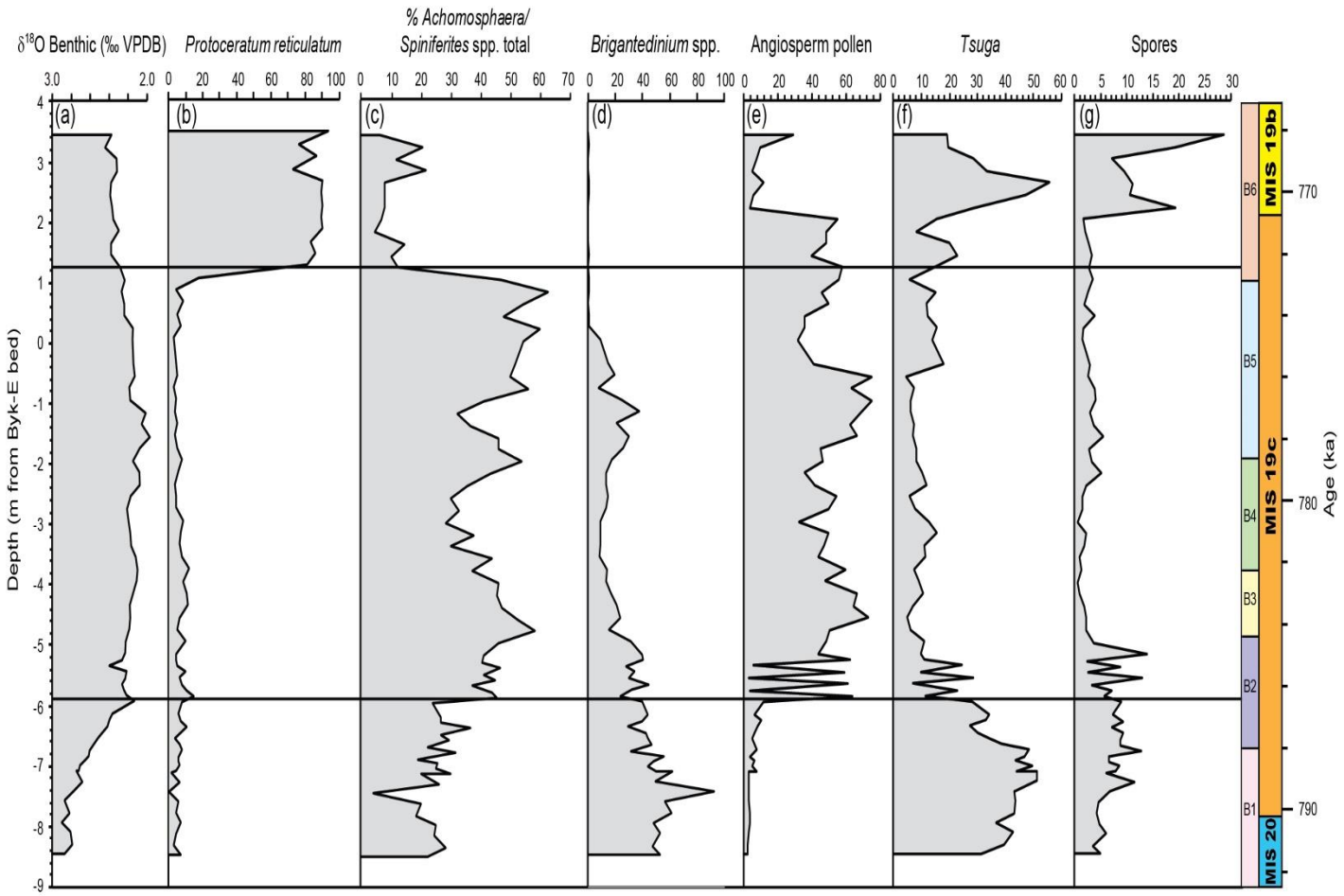

Fig. 22: Comparison between dinocysts, pollen, spores (this study) and the foraminiferal benthic $\delta^{18}O$ record (from Suganuma et al., 2018). All curves showing paleoclimatic changes during the peak of MIS 19c. (a) Benthic $\delta^{18}O$ (b) *Protoceratium reticulatum* (c) *Achomosphaera*/*Spiniferites* total (d) *Brigantedinium* spp. (e) Angiosperm pollen (f) *Tsuga* (g) Spores. The dinocyst taxa are expressed as percentages of the total dinocysts, and the pollen and spores are expressed as percentages of the total palynomorphs.

6.4 Northern Hemisphere climatic drivers and teleconnections during MIS 19

Some paleoceanographic changes observed in the Chiba composite section during MIS 19 likely reflect events that are not limited to the region but exist throughout East Asia, the Northern Hemisphere and indeed globally. It is important to examine the factors that drive changes in ocean currents in the western North Pacific and by extension the entire Northern Hemisphere. Interactions between the tropics and high latitudes play a key role in climatic

changes and ocean circulation in the Northern Hemisphere (Sun et al., 2010). A clear link, for example, has been established between changes in Northern Hemisphere ice sheet growth and the East Asian Monsoon System. Orbital changes in summer insolation at high northern latitudes drive the melting and growth of ice sheets in the Northern Hemisphere which eventually influence the dynamics of the East Asian Monsoon System (Hao et al., 2012). When a less-severe summer insolation minimum at 65° N suppresses ice and snow accumulation, it leads to a contraction of ice sheets and hence a weak Siberian High. A resulting weakened East Asian Winter Monsoon (EAWM) leads to warm conditions in East Asia and the northern North Pacific (Hao et al., 2012). Suganuma et al. (2018) proposed that enhanced winter insolation at 50° N may also lead to a weak Siberian High, and consequently a weak EAWM under ice-free conditions. The relatively small thermal contrast between Siberia and the northwestern Pacific Ocean will then cause a northward shift of the Subarctic Front and a more stratified nearsurface water column (Suganuma et al., 2018). The northward migration of the Kuroshio Current and the Subarctic Front in the latter part of MIS 19c may therefore be explained by the weakening of the EAWM which is influenced by low thermal contrasts between the North Pacific Siberian High and Aleutian Low. This is because the EAWM strength controls wind-driven ocean mixing, and north–south migration of the Subarctic Front (Chiba proposal, 2018, Fig. 15). Evidence for this is given in Suganuma et al. (2018) where the strengthening of the Kuroshio Current and the northward shift of the subtropical gyre during the later part of MIS 19, inferred from the increase in tropical and subtropical species of planktonic foraminiferal, coincided with the weakening of the EAWM, thereby conveying heat northward. Grain size variations in loess-paleosol sequences on the Chinese Loess Plateau provide evidence of this weaker EAWM (Sun et al., 2006, 2010). Insolation driven by orbital forcing largely controls the Northern Hemisphere ice sheet

growth which consequently drives changes in ocean temperatures and currents (Hays et al., 1976; Berger, 1988).

The dinocyst record contributes to the evaluation of teleconnections between the Chiba section and the global dataset. The sharp decrease in species richness and evenness, the abrupt and sustained rise to dominance of *Protoceratium reticulatum*, and a corresponding increase in dinocyst concentrations at 773 ka, the beginning of Biozone 6 (Fig. 19), all indicate changes in water mass characteristics and a strong rise in productivity, which is interpreted here as as reflecting a southward shift in the Subarctic Front. A sharp increase to heavier planktonic foraminiferal isotopes in the Chiba section corroborates a decline in sea-surface temperatures consistent with this southward shift and is supported by the drop in August SST (2°C) based on the dinocyst MAT. It is best explained by a southward movement of the Oyashio Current, starting at 773 ka. This event corresponds with the end of MIS 19c at ~772 in the EDC3 chronology from an Antarctic ice core, where the growth of ice sheets and first appearance of ice-rafted detritus during MIS 19 began at ~772.5 kyr BP, leading to the onset of bi-polar-seesaw variability (Jouzel et al., 2007). This event also coincides with the beginning of cooler conditions at ~773 ka in the benthic $\delta^{18}O$ record in ODP Site 983 in the Gardar Drift, North Atlantic (Channell and Kleiven, 2000; Kleiven et al., 2011; Channell et al., 2010). Emanuele et al. (2015) similarly showed the arrival of cold waters and a southward shift of the Subpolar Front, as indicated by higher abundance of cold species *Coccolithus pelagicus pelagicus*, at central North Atlantic Site U1313 toward the end of MIS 19c.

Nonetheless, a sharp rise in productivity (increase in biogenic silica) is seen in Lake Baikal (Prokopenko et al., 2006; Suganuma et al., 2017, fig. 13) at ~772 ka, signalling warming conditions. Similarly, at ~773 ka in the Chiba composite section, Suganuma et al. (2018) recorded several minima in the planktonic $\delta^{18}O$ record of *G. bulloides*, increased abundance of *G. ruber* and increased factor loading for the Kuroshio Current in the later part

of MIS 19 (beyond 770 ka), suggesting high SST events occurring against a global cooling trend toward MIS 18 (as evidenced above), also noting that the lightest planktonic $\delta^{18}O$ values for *G. bulloides* and highest relative abundance of *G. ruber* occur after the peak temperatures of MIS 19c (Fig. 21). These warmer SSTs during the later part of MIS 19 must correspond to a northward shift of the Subarctic Front off Japan, bringing the subtropical Kuroshio Current over the position of the Chiba section. Balancing this interpretation with the evidence from dinocysts implies a rapid southward shift of the Subpolar Front at 773 ka followed by a second deflection northward, and hence warming, around 770 ka which might then correspond with warming registered at Lake Baikal. Future work to extend the dinocyst record beyond 770 ka would provide a strong test of this hypothesised sequence of events. If the Subpolar Front does indeed shift northward at 770 ka, this should be reflected in a simultaneous decline in *Protoceratium reticulatum*.

6.5 Hypothetical timing for the next glacial inception of the present interglacial

Discussion over the hypothetical "natural" timing for the next glacial inception continue to arise and various approaches have been employed to provide answers (e.g. Ruddiman, 2007; Tzedakis et al., 2012; Ganopolski et al., 2016). Past interglacials can be used to draw analogies with the present, provided their duration is known (Tzedakis et al., 2012; Giaccio et al., 2015). MIS 19 interglacial has been suggested to be the closest orbital analogue for the present interglacial since the paleoclimatic signal and astronomical signature of MIS 19 and MIS 1 (Holocene) are analogous and align well (Pol et al., 2010; Tzedakis, 2010; Tzedakis et al., 2012, Yin and Berger, 2012), although MIS 19 has much lower CO_2 levels than the Holocene (Ganopolski et al., 2016) (Fig. 23). The phasing of the obliquity maximum and the precession minimum are similar in both MIS 19 and MIS 1, including the similar weak precession-eccentricity forcing in both stages (see Fig. 23). Based on these astronomical characteristics of MIS 19, Tzedakis (2010) noted that today corresponds to ~777 kyr BP.

It has been established in Section 6.3 above that the dinocyst record does not give a clear signal of the start of marine interglacial conditions, although it does show an unambiguous and a clear termination of full interglacial conditions at the beginning of Biozone 6 (~773 ka). Hence, the dinocyst record may not be the best proxy to determine the next glacial inception. As stated earlier, the duration of full interglacial conditions at the Chiba composite section is around 15 kyr (787–772 ka) based on marine proxies, and ~10 kyr (785.0–775.1 ka) based on the vegetational (pollen) record (Suganuma et al., 2018). Since the duration of MIS 19c is 15–10 kyr according to the marine and terrestrial proxies and MIS 1 is already ~11.5 kyr old since its inception (Tzedakis et al., 2012). Therefore, the next glacial inception could occur within the next 3500 years, if the atmospheric CO_2 concentration did not exceed 240 ± 5ppmv as was the case at the end of MIS 19c (Fig. 23). The duration of full interglacial conditions during MIS 19 does of course provide a useful baseline in climate modelling studies, but it is human-induced changes to the climate system that will keep us in a full interglacial state for thousands of years to come.

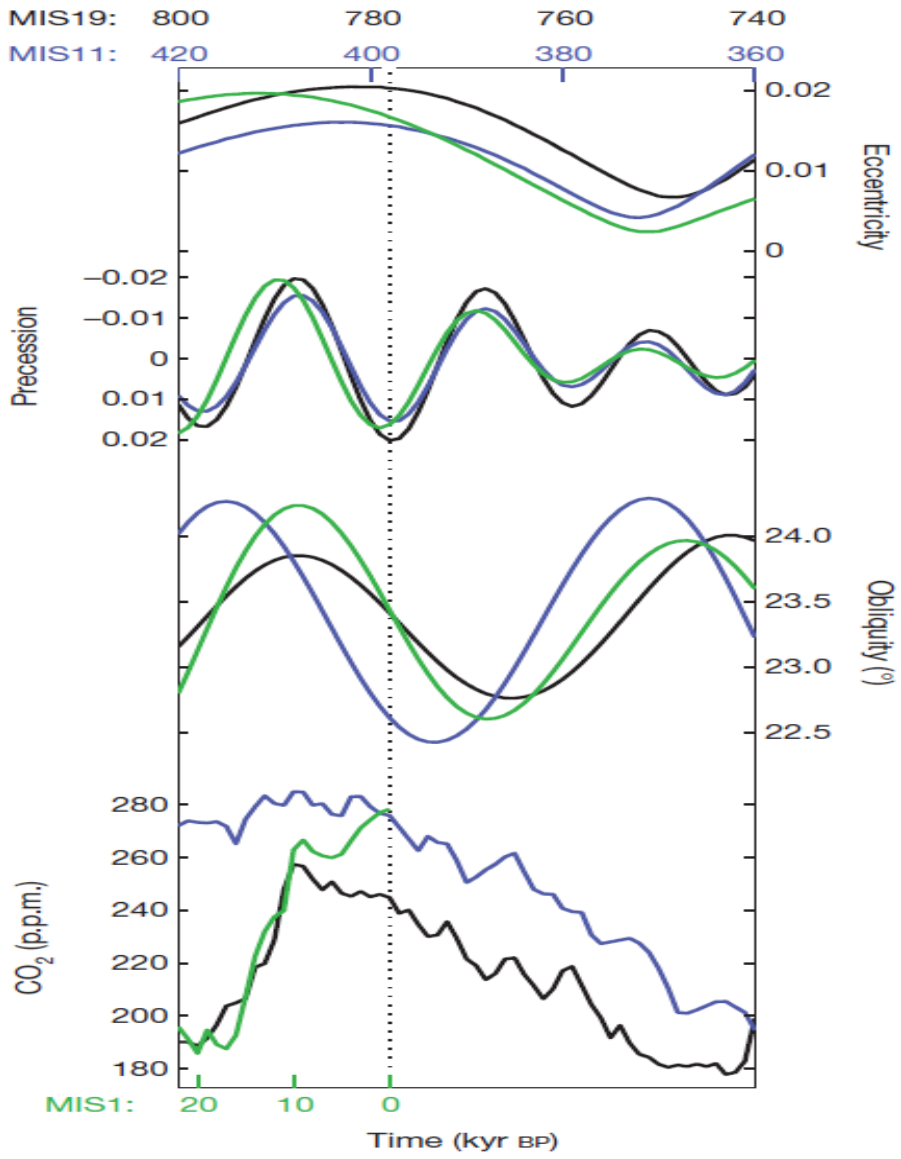

Fig. 23: Comparison between MIS 1 (green), MIS 11 (blue) and MIS 19 (black) orbital parameters and CO_2 concentrations. MIS 19 and MIS 1 align almost perfectly, although their CO_2 levels diverge. This suggests that MIS 19 is the closest analogue for the present interglacial. The vertical dashed line corresponds to the present day for MIS 1 and the minima of the precessional component of insolation for MIS 11 and MIS 19 (Source: Ganopolski et al., 2016, fig. 1).

CONCLUSIONS

The study reveals paleoceanographic changes during MIS 19 from the record of dinoflagellate cyst assemblages in the Chiba composite section, east-central Japanese archipelago, a candidate stratotype for the Early–Middle Pleistocene subseries boundary. The Chiba section is a well-exposed and continuous sedimentary sequence that contains marine and terrestrial records of climatic change with well-developed chronological control. Although the Chiba composite section has been comprehensively studied for pollen, foraminiferal oxygen isotopes, biostratigraphy, lithostratigraphy and magnetostratigraphy, the present study is the first to report on the dinocysts, and the resulting assemblage data provide new paleoceanographic and paleoclimatic details for the interval (791–770 ka).

During Termination IX, the dinoflagellate cyst record shows decrease in heterotrophic *Protoperidinium* species (e.g. *Brigantedinium* spp. *Selenopemphix nephroides*) and corresponding increase in warm-water autotrophs (e.g. *Spiniferites hyperacanthus*/*mirabilis*, *Achomosphaera*/*Spiniferites* spp., *Lingulodinium machaerophorum*). This clearly reflects a progressive decline in productivity, upwelling and nutrient levels in the surface-waters corresponding to deglaciation and transition from the cold, nutrient-enriched waters of MIS 20 to warm conditions in MIS 19. The peak of MIS 19 is characterized by high abundance of warm-water autotrophic dinocysts such as *Spiniferites hyperacanthus*/*mirabilis*, *Achomosphaera*/*Spiniferites* spp. total., *Lingulodinium machaerophorum*, *Operculodinium isrealianum*, and *Tuberculodinium vancampoae*. This shows that warm conditions prevailed during the peak of MIS 19 as the warm Kuroshio Current migrated northward while the cold Oyashio current weakened. The Kuroshio Current usually transports warm surface water northwards, causing a northward shift of the Subarctic Front. This northward migration of the

Kuroshio Current during the peak of MIS 19, influenced by the North Pacific–Siberian pressure contrasts, is probably due to the weakening of the East Asian winter monsoon (EAWM).

Towards the end of MIS 19c, species richness and evenness decreased drastically with a sudden shift to dominance of *Protoceratum reticulatum*, which along with increasing cyst concentrations indicates a rise in surface water productivity. This interpreted to represent the increased influence of the cold Oyashio Current and hence the southward shift of the Subpolar Front. This paleoceanographic feature has not been reported previously but aligns with a brief cooling as interpreted from as shift to heavier oxygen isotopes in the planktonic foraminieral record. It also compares approximately with a decline in temperatures on land as determined from the pollen record (Suganuma et al., 2018). It corresponds to the M–B boundary at ~772.9 ka in the Chiba section. The dinocyst SST and SSS reconstructions, using a modern Northern Hemisphere calibration dataset, indicate winter SSTs ranging from -1 to 15 °C and summer SSTs ranging from 4 to 25 °C. The winter and summer SSS ranges from 28 to 38 psu. SST and SSS was much higher during the peak of MIS 19. The dinocyst record is consistent with the $\delta^{18}O$ glacial–interglacial cycle. Comparisons between the dinocyst record and that of the benthic $\delta^{18}O$ show no evident leads or lags. The dinocyst record helps define the duration of full interglacial conditions in the marine realm at ~15 kyr. This compares with ~10 kyr based on the pollen record (Suganuma et al., 2018). MIS 19 is considered a closer analogue for the present interglacial than MIS 11 because the phasing of the obliquity maximum and the precession minimum are more similar, with comparable weak precession-eccentricity forcing for both stages. Detailed characterization of MIS 19 from the Chiba composite section based on a range of proxies including the dinocyst record reveals a

hypothetical timing of ~3500 kyr for the onset of the next glaciation, although human influences obviously negate such predictions.

REFERENCES

Aida, N., 1997. Paleomagnetic stratigraphy of the type section (proposed site) for the Lower/Middle Pleistocene Boundary Kokumoto Formation. In: Kawamura, M., Oka, T., Kondo, T. (Eds.), Commemorative Volume for Professor Makoto Kato, pp. 275-282 (in Japanese with English abstract).

Baba, A.K., Matsuda, T., Itaya, T., Wada, Y., Hori, N., Yokoyama, M., Eto, N., Kamei, R., Zaman, H., Kidane, T., Otofuji, Y., 2007. New age constraints on counter-clockwise rotation of NE Japan. Geophys. J. Int. 171, 1325–1341.

Berger, W.H., Bickert, T., Jansen, E., Wefer, G., Yasuda, M., 1994. The central mystery of the Quaternary ice age: a view from the South Pacific. Oceanus 36 (4), 53–56.

Berger, A., 1988. Milankovitch Theory and climate. Reviews of geophysics. 26, 4, 624–657. https://doi.org/10.1029/RG026i004p00624.

Blow, W.H., 1969. Late middle Eocene to recent planktonic foraminiferal biostratigraphy. In: Bronnimann, P., Renz, H.H. (Eds.), Proceedings of the First International Conference on Planktonic Microfossils, Geneva, 1967, 1, E.J. Brill, Leiden, pp. 199–422.

Bonnet, S., de Vernal, A., Hillaire-Marcel, C., 2010. Variability of sea-surface temperature and sea-ice cover in the Fram Strait over the last two millennia. Mar. Micropaleontol. 74, 59–74.

Channell, J.E.T., Curtis, J.H. & Flower, B.P. 2004. The Matuyama–Brunhes boundary interval (500–900 ka) in North Atlantic drift sediments. Geophysical Journal International, 158, 489–505.

Channell, J.E.T., Hodell, D.A., Singer, B.S., and Xuan, C., 2010, Reconciling astrochronological and $^{40}Ar/^{39}Ar$ ages for the Matuyama-Brunhes boundary and late Matuyama Chron: Geochemistry Geophysics Geosystems, v. 11, Q0AA12, doi:10.1029/2010GC003203.

Channell, J.E.T., Kleiven, H.F., 2000. Geomagnetic paleointensities and astrochronological ages from the Matuyama-Brunhes boundaries and the boundaries of Jaramillo Subchron: paleomagnetic and isotope records from ODP Site 983. Philosophical Transaction of Royal Society of London 358, 1027–1047.

Cherepanova, M.V., Pushkar, V.S., Razjigaeva, N., Kumai, H., Koizumi, I., 2002. Diatom biostratigraphy of the Kazusa Group, Boso Peninsula, Honshu, Japan. The Quaternary Research (Daiyonki Kenkyu) 41, 1-10.

Dale, B., 1996. Dinoflagellate cyst ecology: Modeling and geological applications. In: J. Jansonius, & D. C. McGregor (Eds), Palynology: Principles and applications (Vol. 3, pp. 1249–1275). Salt Lake City, UT: American Association of Stratigraphic Palynologist.

Dale, B., Dale, A. 2002. Environmental application of dinoflagellate cysts and acritarchs, p. 207–239. In: S. K. Haslett (Editor), Quaternary Environmental Micropalaeontology, Arnold, London.

Dale, B., Dale, A.L., Jansen, J.H.F., 2002. Dinoflagellate cysts as environmental indicators in surface sediments from the Congo deep-sea fan and adjacent regions. Palaeogeography, Palaeoclimatology, Palaeoecology, 185(3–4), 309–338.

De Schepper, S., 2006. Plio-Pleistocene dinoflagellate cyst biostratigraphy and palaeoecology of the eastern North Atlantic and southern North Sea Basin. PhD dissertation, Wolfson College, University of Cambridge.

De Schepper, S., and Head, M.J., 2008, New dinoflagellate cyst and acritarch taxa from the Pliocene and Pleistocene of the eastern North Atlantic (DSDP Site 610): Journal of Systematic Palaeontology, v. 6, no. 1, p. 101–117, doi:10.1017/S1477201907002167.

De Schepper, S. and Head, M. J. 2009. Pliocene and Pleistocene Dinoflagellate Cyst and Acritarch Zonation of DSDP Hole 610A, Eastern North Atlantic. *Palynology*, 33: 179–218.

de Vernal, A., Bilodeau, G., Hillaire-Marcel, C., Kassou, N., 1992a. Quantitative assessment of carbonate dissolution in marine sediments from foraminifer linings vs. shell ratios: Davis Strait, northwest North Atlantic. Geology, 20:527-530.

de Vernal, A., Rochon, A., Turon, J-L., Matthiessen J., 1998. Organic-walled dinoflagellate cysts: Palynological tracers of sea-surface conditions in middle to high latitude marine environments. Geobios 30, 7, 905-920.

de Vernal, A., Eynaud, F., Henry, M., Hillaire-Marcel, C., Londeix, L., Mangin, S., Matthiessen, J., Marret, F., Radi, T., Rochon, A., Solignac, S., Turon, J., 2005a. Reconstruction of sea-surface conditions at middle to high latitudes of the Northern Hemisphere during the Last Glacial Maximum (LGM) based on dinoflagellate cyst assemblages. Quaternary Science Reviews, 24(7–9), 897–924.

de Vernal, A., Guiot, J., Turon, J.L., 1993. Postglacial evolution of environments in the Gulf of St. Lawrence: Palynological evidence. Ge´ographie physique et Quaternaire, 47, 167–180.

de Vernal, A., Henry, M., Matthiessen, J., Mudie, P., Rochon, A., Boessenkool, K., Eynaud, F., Grøsfjeld, K., Guiot, J., Hamel, D., Harland, R., Head, M., Kunz-Pirrung, M., Levac, E., Loucheur, V., Peyron, O., Pospelova, V., Radi, T., Turon, J.L., Voronina, E., 2001. Dinoflagellate cyst assemblages as tracers of sea-surface conditions in the northern North Atlantic, Arctic and sub-Arctic seas: the new "n = 677" data base and its application for quantitative palaeoceanographic reconstruction. J. Quat. Sci. 16, 681–698.

de Vernal, A., Hillaire-Marcel, C., Turon, J.L., Matthiessen, J., 2000. Reconstruction of sea surface temperature, salinity, and sea-ice cover in the northern North Atlantic during the last glacial maximum based on dinocyst assemblages. Can. J. Earth Sci. 37, 725–750.

de Vernal, A., Rochon, A., Radi, T., 2007. Dinoflagellates. In: Elias, S.A. (Ed.), Encyclopaedia of Quaternary Science, pp. 1652–1667. Reichart, G.J., Brinkhuis, H., 2003. Late Quaternary Protoperidinium cysts as indicators of paleoproductivity in the northern Arabian Sea, Mar. Micropaleontol., 49(4), 303– 315.

de Vernal, A., Turon, J.L., Guiot, J., 1994. Dinoflagellate cyst distribution in high latitude marine environments and quantitative reconstruction of sea-surface salinity, temperature, and seasonality. Canadian Journal of Earth Sciences, 31(1), 48–62.

de Vernal, A., Hillaire-Marcel, C., Rochon, A., Fréchette, B., Henry, M., Solignac, S., Bonnet, S., 2013. Dinocyst-based reconstructions of sea ice cover concentration during the Holocene in the Arctic Ocean, the northern North Atlantic Ocean and its adjacent seas. Quaternary Science Reviews. 79. 111-121. 10.1016/j.quascirev.2013.07.006.

Devillers, R., de Vernal, A., 2000. Distribution of dinoflagellate cysts in surface sediments of the northern North Atlantic in relation to nutrient content and productivity in surface waters. Marine Geology, 166, 103–124.

Domitsu H., Oda M., 2008. Holocene influx of the Tsushima Current into the Japan Sea signalled by spatial and temporal changes in Neogloboquadrina incompta distribution. SAGE Journal. 18, 2, p. 345–352.

Eaton, G.L., Fensome, R.A., Riding, J.B., Williams, G.L., 2001. Re-evaluation of the status of the dinoflagellate cyst genus *Cleistosphaeridium*. N. Jb. Geol. Paläont., Abh.; 219; 171-205; Stuttgart.

Edwards, L. E. and Adrle, V. A. S. 1992. Distribution of selected dinoflagellate cysts in modern marine sediments, p. 259–288. *In*: Head, M. J., and Wrenn, J. H. (Eds.), 1992, *Neogene and Quaternary Dinoflagellate Cysts and Acritarchs*: American Association of Stratigraphic Palynologists Foundation, Dallas.

Elderfield, H., Ferretti, P., Greaves, M., Crowhurst, S., McCave, I.N., Hodell, D., Piotrowski, A.M., 2012. Evolution of ocean temperature and ice volume through the mid-Pleistocene climate transition. Science 337, 704–709. doi:10.1126/science.1221294.

Emanuele, D., Ferretti, P., Palumbo, E., Amore, F.O., 2015. Sea-surface dynamics and palaeoenvironmental changes in the North Atlantic Ocean (IODP Site U1313) during Marine Isotope Stage 19 inferred from coccolithophore assemblages. Palaeogeography, Palaeoclimatology, Palaeoecology 430, 104–117.

Favorite, F., Dodimead, A. J., Nasu, K., 1976. Oceanography of the subarctic Pacific region, 1962–72. Bull. Int. North Pac. Fish. Comm. 33, 1–187.

Ferretti, P., Crowhurst, S.J., Naafs, B.D.A., Barbante, C., 2015. The Marine Isotope Stage 19 in the mid-latitude North Atlantic Ocean: astronomical signature and intra-interglacial variability. Quat. Sci. Rev. 108, 95–110. http://dx.doi.org/10.1016/j.quascirev.2014.10.024.

Ganopolski1, A., Winkelmann, R., Schellnhuber, H.J., 2016. Critical insolation–CO_2 relation for diagnosing past and future glacial inception. Nature. Vol. 529. 200-203.

Giaccio1, B., Regattieri1, E., Zanchetta, G., Nomade, S., Renne, P.R., Sprain, C.J., Drysdale, R.N., Tzedakis, P.C., Messina, P., Scardia, G., Sposato, A., Bassinot, F., 2015. Duration and dynamics of the best orbital analogue to the present interglacial. Geological Society of America. V. 43; No. 7; P. 603–606 doi:10.1130/G36677.1.

Gotelli N. J., and Chao A., 2013. Measuring and Estimating Species Richness, Species Diversity, and Biotic Similarity from Sampling Data. In: Levin S.A. (ed.) Encyclopedia

of Biodiversity, second edition, Volume 5, pp. 195-211. Waltham, MA: Academic Press.

Grimm E.C., 1986. Coniss: a fortran 77 program for stratigraphically Constrained cluster analysis by the method of Incremental sum of squares. Computers and Geosciences Vol. 13. No. I. pp. 13-35.

Hammer, Ø., Harper, D.A.T., and Ryan, P.D., 2001, Past: Paleontological statistics software package for education and data analysis: Paleontologia Electronica, v. 4 (1), p. 1–9.

Hao, Q.,Wang, L., Oldfield, F., Peng, S., Qin, L., Song, Y., Xu, B., Qiao, Y., Bloemendal, J., Guo, Z., 2012. Delayed build-up of Arctic ice sheets during 400,000-year minima in insolation variability. Nature 490, 393–396. https://doi.org/10.1038/nature11493.

Hays, J.D., Imbrie, J., and Shackleton, N.J., 1976, Variations in the Earth's orbit: pacemaker of the Ice Ages: Science, v. 194, no. 4270, p. 1121–1132.

Harland, R., 1983, Distribution maps of recent dinoflagellate cysts in bottom sediments from the North Atlantic Ocean and adjacent seas: Paleontology, v. 26, p. 321–387.

Hashima, A., Sato, T., Sato, H., Asao, K., Furuya, H., Yamamoto, S., Kameo, K., Miyauchi, T., Ito, T., Tsumura, N., Kaneda, H., 2016. Simulation of tectonic evolution of the Kanto Basin of Japan since 1 Ma due to subduction of the Pacific and Philippine Sea plates and the collision of the Izu-Bonin arc. Tectonophysics 679, 1–14.

Head, M.J., and Gibbard, P.L., 2015a. Formal subdivision of the Quaternary System/Period: Past, present, and future. Quaternary International, 383: 4–35.

Head, M.J, Gibbard, P.L., 2015b. Early–Middle Pleistocene transitions: Linking terrestrial and marine realms. Quaternary International 389 (2015) 7–46.

Head, M.J., 1993b. Dinoflagellate cysts, sporomorphs, and other palynomorphs from the upper Pliocene St. Erth Beds of Cornwall, southwestern England. Paleontological Society Memoir 31 (Journal of Paleontology, 67(3) Supplement), 62 p.

Head, M.J., 1994. Morphology and paleoenvironmental significance of the Cenozoic dinoflagellate genera *Habibacysta* and *Tectatodinium*. Micropaleontology, 40:289–321.

Head, M.J., 1996. Late Cenozoic dinoflagellates from the Royal Society borehole at Ludham, Norfolk, Eastern England. Journal of Paleontology, Vol. 70, No. 4, pp. 543-570.

Head, M.J., 1996. Modern dinoflagellate cysts and their biological affinities. In: J. Jansonius, D. C. McGregor (Eds), Palynology: Principles and applications (Vol. 3, pp. 1197–1248). Salt Lake City, UT: American Association of Stratigraphic Palynologists

Foundation.

Head, M.J., 1998. Marine environmental change in the Pliocene and early Pleistocene of eastern England: the dinoflagellate evidence reviewed. *In* T. Van Kolfschoten and P. Gibbard (eds.), The Dawn of the Quaternary. Mededelingen Nederlands Instituut voor Toegepaste Geowetenschappen TNO, 60:199–225.

Head, M.J., Gibbard, P.L., 2005. Early–Middle Pleistocene transitions: an overview and recommendation for the defining boundary. In: Head, M.J., Gibbard, P.L. (Eds.), Early–Middle Pleistocene Transitions: The Land–ocean Evidence, Special Publications, 247. Geological Society, London, pp. 1–18.

Head, M.J., Riding, J.B., Eidvin, T., Chadwick, R.A., 2004. Palynological and foraminiferal biostratigraphy of (Upper Pliocene) Nordland Group mudstones at Sleipner, northern North Sea. Marine and Petroleum Geology, Volume 21, Issue 3, March 2004, Pages 277-297. https://doi.org/10.1016/j.marpetgeo.2003.12.002.

Head, M.J., H., Westphal., 1999. Palynology and paleoenvironments of a Pliocene carbonate platform: the Clino Core, Bahamas. Journal of Paleontology, 73:1–25.

Head, M.J., Pillans, B., Farquhar, S., 2008. The Early–Middle Pleistocene Transition: characterization and proposed guide for the defining boundary. Episodes 31 (2), 255-259.

Hennissen, J.A.I., Head, M.J., De Schepper, S., and Groeneveld, J., 2014. Palynological evidence for a southward shift of the North Atlantic Current at ~2.6 Ma during the intensification of late Cenozoic Northern Hemisphere glaciation. Paleoceanography, 28, doi: 10.1002/ 2013PA002543.

Hennissen, J.A.I., Head, M.J., De Schepper, S., and Groeneveld, J., 2015. Increased seasonality during the intensification of Northern Hemisphere glaciation at the Pliocene–Pleistocene boundary ~2.6 Ma. Quaternary Science Reviews, 129: 321–332.

Hennissen, J.A.I., Head, M.J., De Schepper, S., and Groeneveld, J., 2017. Dinoflagellate cyst paleoecology during the Pliocene–Pleistocene climatic transition in the North Atlantic. Palaeogeography, Palaeoclimatology, Palaeoecology 470: 81–108.

Heusser, L.E., 1990. Northeast Asian pollen records for the last 150,000 years from deep-sea cores V28-304 and RC14-99 taken off the Pacific coast of Japan. Rev. Palaeobot. Palynol. 65, 1–8. doi: 10.1016/0034-6667(90)90050-S.

Hodell, D.A., Lourens, L., Stow, D.A.V., Hern_andez-Molina, J., Alvarez Zarikian, C.A., Shackleton Site Project Members, 2013. The “Shackleton Site” (IODP Site U1385) on the Iberian margin. Scientific Drilling 16, 13-19.

Hyodo, M., Katoh, S., Kitamura, A., Takasaki, K., Matsushita, H., Kitaba, I., Tanaka, I., Nara, M., Matsuzaki, T., Dettman, D.L., Okada, M., 2016. High resolution stratigraphy across the early–middle Pleistocene boundary from a core of the Kokumoto Formation at Tabuchi, Chiba Prefecture, Japan. Quat. Int. 397, 16–26. doi:http://dx.doi.org/10.1016/j.quaint.2015.03.031.

Igarashi, A., 1994. Paleoceanographhic changes during the deposition of the middle Pleistocene Kazusa Group, central Japan: Estimation based on the principal components analysis of planktonic foraminifera. Jour. Geol. Soc. Japan 100, 348–359 (in Japanese with English abstract).

Igarashi, A., 1996. Biostratigraphy of the Chiba section of the Boso Peninsula toward establishing the Lower-Middle Pleistocene boundary stratotype based on planktonic foraminiferal analyses. Proceedings on the research of stratotype for the Lower-Middle Pleistocene boundary, 36–45.

Ito, M., 1992. High-frequency depositional sequences of the upper part of the Kazusa Group, a middle Pleistocene forearc basin fill in Boso Peninsula, Japan. Sedimentary Geology 76, 155-175.

Ito, M., 1998b. Submarine fan sequences of the lower Kazusa Group, a Plio-Pleistocene forearc basin fill in the Boso Peninsula, Japan. Sedimentary Geology 122, 69-93.

Ito, M., 1998. Contemporaneity of component units of the lowstand systems tract: an example from the Pleistocene Kazusa forearc basin, Boso Peninsula, Japan. Geology, 26, 939‑942.

Ito, M., Kameo, K., Satoguchi, Y., Masuda, F., Hiroki, Y., Takano, O., Nakajima, T., Suzuki, N., 2016. Neogene–Quaternary sedimentary successions. In: Moreno et al. (Eds.), The Geology of Japan, Geological Society, London, Geology of Series, pp. 309–337.

Ito, M., Katsura, Y., 1992. Inferred glacio-eustatic control for high-frequency depositional sequences of the Plio-Pleistocene Kazusa Group, a forearc basin fill in Boso Peninsula, Japan. Sedimentary Geology 80, 67-75.

Ito, M., Nishida, N., Otake, S., Saito, T., Okazaki, H., Nishikawa, T., 2006a. Glacioeustatic signals and sequence architecture of the Pliocene–Pleistocene forearc basin-fill

successions on the Boso Peninsula, central Japan. In: Ito, M., Yagishita, K., Ikehara, K., Matsuda, H. (Eds.), Field Excursion Guidebook, 17th International Sedimentological Congress. Sedimentological Society of Japan, FEA4, Fukuoka, Japan, pp. 1-30.

Ito, M., Takao, A., Ishikawa, K., Himeno, O., 2006b. A new avenue of sedimentological study of deep-water successions: reorganization of the lowstand depositional model. Journal of the Japanese Association for Petroleum Technology 71, 21-33 (in Japanese with English abstract).

Jansson, I.-M., Mertens, K.N., Head, M.J., with contributions from de Vernal, A., Londeix, L., Marret, F., Matthiessen, J., Sangiorgi, F., 2014. Statistically assessing the correlation between salinity and morphology in cysts produced by the dinoflagellate Protoceratium reticulatum from surface sediments of the North Atlantic Ocean, Mediterranean–Marmara–Black Sea region, and Baltic–Kattegat–Skagerrak estuarine system. Palaeogeography, Palaeoclimatology, Palaeoecology, 399: 202–213.

Jouzel, J. et al., 2007. Orbital and millennial antarctic climate variability over the past 800,000 years. Science 317, 793-796.

Kaizuka, K., 1987. Quaternary crustal movements in Kanto, Japan. Journal of Geography 96, 223-240 (in Japanese with English abstract).

Kameo, K., Okada, M., El-Masry, M., Hisamitsu, T., Saito, S., Nakazato, H., Ohkouchi, N., Ikehara, M., Yasuda, H., Kitazato, H., Taira, A., 2006. Age model, physical properties and paleoceanographic implications of the middle Pleistocene core sediments in the Choshi area, central Japan. Island. Arc 15, 366–377. https://doi.org/10.1111/j.1440-1738.2006.00535.x.

Kamemaru, A., 1996. Biostratigraphy of the Chiba section of the Boso Peninsula toward establishing the LowereMiddle Pleistocene boundary stratotype based on benthic foraminiferal evidence. In: Proceedings on the Research of Stratotype for the LowereMiddle Pleistocene Boundary. Internal Research Group for the LowereMiddle, Middle-Upper Pleistocene Boundary. Japan Association for Quaternary Research, pp. 46-54.

Katsura, Y., 1984. Depositional Environments of the Plio-Pleistocene Kazusa Group, Boso Peninsula, Japan. Science Reports of the Institute of Geoscience. In: University of Tsukuba, Section B, Geological Sciences 5, pp. 69-104.

Kazaoka, O., Suganuma, Y., Okada, M., Kameo, K., Head, M.J., Yoshida, T., Kameyama, S.,

Nirei, H., Aida, N., Kumai, H. 2015. Stratigraphy of the Kazusa Group, Central Japan: a high-resolution marine sedimentary sequence from the Lower to Middle Pleistocene. Quaternary International, 383, 116–135.

Kim, S.Y., Scourse, J., Marret, F., Lim, D.I., 2010. A 26,000-year integrated record of marine and terrestrial environmental change off Gabon, west equatorial Africa. Palaeogeography, Palaeoclimatology, Palaeoecology 297, 428–438.

Kleiven, H.F., Hall, I.R., McCave, I.N., Knorr, G., Jansen, E., 2011. Coupled deep-water flow and climate variability in the middle Pleistocene North Atlantic. Geological Society of America.v. 39; no. 4; p. 343–346; doi: 10.1130/G31651.1.

Lewis, J., Dodge, J.D., Powell, A.J., 1990. Quaternary dinoflagellate cysts from the upwelling system offshore Peru, Hole 686B, ODP LEG 112. In: E. Suess, R. von Huene, et al. (Eds), Proceedings of the Ocean Drilling Program, Scientific Results, Vol. 112, pp. 323-327.

Lisiecki, L.E., Raymo, M.E., 2005. A Pliocene-Pleistocene stack of 57 globally distributed benthic $\delta^{18}O$ records. Paleoceanography 20, PA1003. http://dx.doi.org/10.1029/2004PA001071.

Löwemark, L., Werner, F., 2001. Dating errors in high-resolution stratigraphy: a detailed X-ray radiograph and AMS-14C study of Zoophycos burrows. Mar. Geol. 177, 191–198.

Maiorano, P., Bertini, A., Capolongo, D., Eramo, G., Gallicchio, S., Girone, A., Pinto, D., Toti, F., Ventruti, G., Marino, M., 2016. Climate signatures through Marine Isotope Stage 19 in the Montalbano Jonico section (southern Italy): a landesea perspective. Palaeogeogr. Palaeoclimatol. Palaeoecol. 461, 341–361. https:// doi.org/10.1016/j.palaeo.2016.08.029.

Marino, M., Bertini, A., Ciaranfi, N., Aiello, G., Barra, D., Gallicchio, S., Girone, A., La Perna, R., Lirer, F., Maiorano, P., Petrosino, P., Toti, F., 2015. Paleoenvironmental and climatostratigraphic insights for Marine Isotope Stage 19 (Pleistocene) at the Montalbano Jonico succession, South Italy. Quaternary International 383, 104–115.

Marret, F., Zonneveld, K.A.F., 2003. Atlas of modern organic-walled dinoflagellate cyst distribution: Review of Palaeobotany and Palynology, v. 125, p. 1–200, doi: 10.1016/S0034-6667(02)00229-4.

Matsuoka, H., Okada, H., 1990. Time-progressive morphometric changes of the genus Gephyrocapsa in the Quaternary sequence of the tropical Indian Ocean, Site 709. In:

Dundan, R.A., Backman, J., Peterson, L.C., et al. (Eds.), Proc. ODP, Sci. Res., 115: College Station, TX, pp. 255–270 (Ocean Drilling Program).

Matsuzaki, K.M., Itaki, T., 2017. New northwest Pacific radiolarian data as a tool to estimate past sea surface and intermediate water temperatures. Paleoceanography 32, 218–245. https://doi.org/10.1002/2017PA003087.

McCarthy, F. M. G., Gostlin, K. E., Mudie, P. J. and Scott, D. B. 2000a. Synchronous palynological changes in early Pleistocene sediments off New Jersey and Iberia, and a possible paleoceanographic explanation. *Palynology*, 24: 63–77.

McCarthy, F.M.G., Gostlin, K.E., Mudie, P.J., Hopkins, J.A., 2003. Terrestrial and marine palynomorphs as sea-level proxies: an example from Quaternary sediments on the New Jersey margin, U.S.A, p. 119–129. In Olson, H.C., Leckie, R.M. (Eds.). Micropaleontologic proxies for sea-level change and stratigraphic discontinuities. Society for Sedimentary Geology, Special Publication No. 75.Tulsa, Oklahama, U.S.A.

Mitsunashi, T., 1980. Geologic Map Sheet, 1:200, 000. Geological Survey of Japan, Otaki.

Mitsunashi, T., Yasukuni, N., Shinada, Y., 1959. Stratigraphical section of the Kazusa Group along the shores of the Rivers Yoro and Obitsu. Bulletin of the Geological Survey of Japan 10, 83-98 (in Japanese).

Mitsunashi, T., Yazaki, K., Kageyama, K., Shimada, T., Ono, E., Yasukuni, N., Makino, T., Shinada, Y., Fujiwara, K., Kamata, S., 1961. Geological Maps of the Oil and Gas Field of Japan No. 4, Futtsu-Otaki, 1:50,000. Geological Survey of Japan.

Mugurran, A.E., 2004. Measuring biological diversity. Blackwell publishing company.

Nakamura, K., Takao, A., Ito, M., 2007. Geometry and internal organization of hyperpycnites associated with a shelf-margin delta, the Middle Pleistocene Kokumoto Formation on the Boso Peninsula of Japan. Journal of the Sedimentological Society of Japan 64, 65-68 (in Japanese with English abstract).

Niitsuma, N., 1976. Magnetic stratigraphy in the Boso Peninsula. Journal of the Geological Society of Japan 82, 163–181 (in Japanese with English abstract).

Nishida, N., Kazaoka, O., Izumi, K., Suganuma, Y., Okada, M., Yoshida, T., Ogitsu, I., Nakazato, H., Kameyama, S., Kagawa, A., Morisaki, M., Nirei, H., 2016. Sedimentary processes and depositional environments of a continuous marine succession across the Lower–Middle Pleistocene boundary: Kokumoto Formation, Kazusa Group, central Japan. Quaternary International 397, 3–15.

Okada, M., Niitsuma, N., 1989. Detailed paleomagnetic records during the Brunhes-Matuyama geomagnetic reversal and a direct determination of depth lag for magnetization in marine sediments. Physics of the Earth and Planetary Interiors 56, 133-150.

Okada, M., Suganuma, Y., Haneda, Y., Kazaoka, O., 2017. Paleomagnetic direction and paleointensity variations during the Matuyama-Brunhes polarity transition from a marine succession in the Chiba composite section of the Boso Peninsula, central Japan. Earth, Planets and Space, in press.

Okuda, M., Nakazato, H., Miyoshi, N., Nakagawa, T., Okazaki, H., Saito, S., Taira, A., 2006. MIS11-19 pollen stratigraphy from the 250-m Choshi core, northeast Boso Peninsula, central Japan: Implications for the early/mid-Brunhes (400-780 ka) climate signals. Isl. Arc 15, 338–354. doi:10.1111/j.1440-1738.2006.00533.x

Oliveira, D., Desprat, S., Yin Qiuzhen, Naughton, F., Trigo, R., Rodrigues, T., Abrantes, F., Sánchez Goñi, M.F., 2017. Unraveling the forcings controlling the vegetation and climate of the best orbital analogues for the present interglacial in SW Europe. Climate Dynamics, 20 pp, DOI 10.1007/s00382-017-3948-7.

Onishi, I., 1969. Pollen flora of the Kazusa Group in the Boso Peninsula, Japan. Earth Science (Chikyu Kagaku) 24, 222–224 (in Japanese with English abstract).

Otofuji, Y.,Matsuda, T., Nohda, S., 1985. Opening mode of the Japan Sea inferred from the palaeomagnetism of the Japan Arc. Nature 317, 603–604.

Oyama, K., 1959. Fossil molluscan succession of Lower Pleistocene in Chiba Prefecture. Bulletin of the Geological Survey of Japan 10, 99-102 (in Japanese).

Pickering, K.T., Souter, C., Oba, T., Taira, A., Schaaf, M., Platzman, E., 1999. Glacioeustatic control on deep-marine clastic forearc sedimentation, Plioceneemid- Pleistocene (c. 1180-600 ka) Kazusa Group. SE Japan. Journal of the Geological Society, London 156, 125-136.

Pillans, B. 2003. Subdividing the Pleistocene using the Matuyama–Brunhes boundary (MBB): an Australian perspective. Quaternary Science Reviews, 22, 1569–1577.

Pol, K., Masson-Delmotte, V., Johnsen, S., Bigler, M., Cattani, O., Durand, G., Falourd, S., Jouzel, J., Minster, B., Parrenin, F., Ritz, C., Steen-Larsen, H.C., Stenni, B., 2010. New MIS 19 EPICA Dome C high resolution deuterium data: Hints for a problematic

preservation of climate variability at sub-millennial scale in the “oldest ice.” Earth Planet. Sci. Lett. 298, 95–103. doi:10.1016/j.epsl.2010.07.030.

Pospelova, V. (2005), Dinoflagellate cysts in surface sediments across the northeast Pacific continental shelf in relation to sea-surface temperature, salinity, productivity, and coastal upwelling, paper presented at First International Workshop on Taxonomy of Modern Dinoflagellates in the Pacific, Inst. for East China Sea Res., Nagasaki Univ., Nagasaki, Japan.

Prokopenko, A.A., Hinnov, L.A., Williams, D.F., Kuzmin, M.I., 2006. Orbital forcing of continental climate during the Pleistocene: a complete astronomically tuned climatic record from Lake Baikal, SE Siberia. Quat. Sci. Rev. 25, 3431–3457. doi:10.1016/j.quascirev.2006.10.002

Radi, T., de Vernal, A., 2004. Dinocyst distribution in surface sediments from the northeastern Pacific margin (40–601N) in relation to hydrographic conditions, productivity and upwelling. Review of Palaeobotany and Palynology, 128(1–2), 169.

Radi, T., Pospelova, V., de Vernal, A., Barrie, J.V., 2007. Dinoflagellate cysts as indicators of water quality and productivity in British Columbia estuarine environments. Marine Micropaleontology 62 (4), 269–297.

Radi, T., and de Vernal, A., 2008a, Last Glacial Maximum (LGM) primary productivity in the northern North Atlantic Ocean: Canadian Journal of Earth Sciences, v. 45, p. 1299-1316, doi: 10.1139/E08-059.

Radi, T., and de Vernal, A., 2008b, Dinocysts as proxy of primary productivity in mid–high latitudes of the Northern Hemisphere: Marine Micropaleontology, v. 68, p. 84–114, doi: 10.1016/j.marmicro.2008.01.012.

Railsback, L.B., Gibbard, P.L., Head, M.J., Voarintsoa, N.R.G., Toucanne, S., 2015. An optimized scheme of lettered marine isotope substages for the last 1.0 million years, and the climatostratigraphic nature of isotope stages and substages. Quat. Sci. Rev. 111, 94–106. https://doi.org/10.1016/j.quascirev.2015.01.012.

Reichart, G.J., and Brinkhuis, H., 2003, Late Quaternary *Protoperidinium* cysts as indicators of paleoproductivity in the northern Arabian Sea: Marine Micropaleontology, v. 937, p. 1–13.

Reid, P.C., 1977. Peridiniacean dinoflagellate cysts from the British Isles. Nova Hedwigia, 29: 429–463.

Remane, J., Basset, M.G., Cowie, J.F., Gohrbandt, K.H., Lane, H.R., Michelsen, O., Naiwen, W., 1996. Revised guidelines for the establishment of global chronostratigraphic standards by the International Commission on Stratigraphy (ICS). Episodes 19, 77–81.

Richmond, G.M., 1996. The INQUA-approved provisional Lower–Middle Pleistocene boundary. *In*: TURNER, C. (ed.) The Early–Middle Pleistocene in Europe. Balkema, Rotterdam, 319–326.

Rochon, A., de Vernal, A., Turon, J., Matthiessen, J., and Head, M.J., 1999, Distribution of recent dinoflagellate cysts in surface sediments from the North Atlantic Ocean and adjacent seas in relation to sea-surface parameters: AASP Contributions Series, no. 35, p. 1–152.

Rodríguez-Tovar, F.J., Dorador, J., 2014. Ichnological analysis of Pleistocene sediments from the IODP Site U1385 "Shackleton Site" on the Iberian margin: approaching paleoenvironmental conditions. Palaeogeography, Palaeoclimatology, Palaeoecology 409, 24-32.

Ruddiman, W.F., 2007. The early anthropogenic hypothesis: Challenges and responses, Rev. Geophys., 45, RG4001, doi:10.1029/2006RG000207.

Sánchez Goñi M.F., Rodrigues T., Hodell D.A., Polanco-Martínez J.M., Alonso-García M., Hernández-Almeida I., Desprat S., Ferretti P., 2016. Tropically-driven climate shifts in southwestern Europe during MIS 19, a low eccentricity interglacial. Earth Planet Sci Lett 448:81–93. doi:10.1016/j.epsl.2016.05.018.

Sato, T., Takayama, T., Kato, M., Kudo, T., Kameo, K., 1988. Calcareous microfossil biostratigraphy of the uppermost Cenozoic formations distributed in the coast of the Japan Sea, Part 4: conclusion. Journal of the Japanese Association for Petroleum Technology 53, 474-491 (in Japanese with English abstract).

Seno, T., Takano, T., 1989. Seismotectonics at the Trench-Trench-Trench Triple Junction off Central Honshu. Pure and Applied Geophysics 129, 27-40.

Stancliffe, R.P.W., 1989. Microforaminiferal linings: their classi-fication, biostratigraphy and paleoecology, with special reference to specimens from British Oxfordian sediments. Micropaleontology, 35: 337-352.

Stockmarr, J., 1971. Tablets with spores used in absolute pollen analysis. *Pollen et Spores*, 13: 615–621.

Suganuma, Y., Chiba composite section community members, 2017. The Chiba Section,

Japan: a proposed Global Boundary Stratotype Section and Point (GSSP) for the base of the Middle Pleistocene Subseries. Unpublished.

Suganuma, Y., Haneda, Y., Kameo, K., Kubota, Y., Hayashi, H., Itaki, T., Okuda, M., Head, M.J., Sugaya, M., Nakazato, H., Igarashi, A., Shikoku, K., Hongo, M., Watanabe, M., Satoguch, Y., Takeshita, Y., Nishida, N., Izumi, K., Kawamura, K., Kawamata, M., Jun'ichi Okuno, J., Yoshida, T., Ogitsu, I., Yabusaki, H., Okada M. 2018. Paleoclimatic and paleoceanographic record of Marine Isotope Stage 19 at the Chiba composite section, central Japan: A reference for the Early–Middle Pleistocene boundary. Quaternary Science Reviews 191 (2018) 406–430.

Suganuma, Y., Okada, M., Horie, K., Kaiden, H., Takehara, M., Senda, R., Kimura, J., Kawamura, K., Haneda, Y., Kazaoka, O., Head, M.J., 2015. Age of Matuyama–Brunhes boundary constrained by U-Pb zircon dating of a widespread tephra. Geology 43 (4). http://dx.doi.org/10.1130/G36625.1.

Sun, Y., An, Z., Clemens, S.C., Bloemendal, J., Vandenberghe, J., 2010. Seven million years of wind and precipitation variability on the Chinese Loess Plateau. Earth Planet. Sci. Lett. 297, 525–535. https://doi.org/10.1016/j.epsl.2010.07.004.

Sun, Y.B., Clemens, S.C., An, Z.S., Yu, Z.W., 2006. Astronomical timescale and palaeoclimatic implication of stacked 3.6-Myr monsoon records from the Chinese Loess Plateau. Quat. Sci. Rev. 25, 33e48. https://doi.org/10.1016/j.quascirev.2005.07.005.

Suzuki, T., Obara, M., Aoki, T., Murata, M., Kawashima, S., Kawai, M., Nakayama, T., Tokizane, K., 2011. Identification of Lower Pleistocene tephras under Tokyo and reconstruction of Quaternary crustal movements, Kanto Tectonic Basin, central Japan. Quaternary International 246, 247-259.

Takemoto, A., Oda, M., 1997. New planktic foraminiferal transfer functions for the Kuroshio-Oyashio current region off Japan. Paleontological Research 1, 291–310. https://doi.org/10.2517/prpsj.1.291.

Takeshita, Y., Matsushima, N., Teradaira, H., Uchiyama, T., Kumai, H., 2016. A marker tephra bed close to the Middle Pleistocene boundary: Distribution of the Ontake-Byakubi tephra in central Japan, Quaternary International, 397:27–38. doi: 10.1016/j.quaint.2015.03.054.

Telford, R.J., 2006. Limitations of dinoflagellate cyst transfer functions. Quat. Sci. Rev. 25,

1375–1382. http://dx.doi.org/10.1016/j.quascirev.2006.02.012.

Telford, R.J., Birks, H.J.B., 2009. Evaluation of transfer functions in spatially structured environments. Quat. Sci. Rev. 28, 1309–1316. http://dx.doi.org/10.1016/j.quascirev.2008.12.020.

Telford, R.J., Birks, H.J.B., 2011. QSR Correspondence "Is spatial autocorrelation introducing biases in the apparent accuracy of palaeoclimatic reconstructions?". Quat. Sci. Rev. 30, 3210–3213. http://dx.doi.org/10.1016/j.quascirev.2011.07.019.

Tokuhashi, S., Endo, H., 1984. Geology of Anesaki District with Geologic Map Sheet, 1:50,000. Geological Survey of Japan (in Japanese with English abstract).

Traverse, A., Ginsburg, R.N., 1966. Palynology of the surface sediments of Great Bahama Bank, as related to water movement and sedimentation. Marine Geology, 4:417-459.

Tsunakawa, H., Okada, M., Niitsuma, N., 1999. Further application of the deconvolution method of post-depositional DRM to the precise record of the Matuyama-Brunhes reversal in the sediments from the Boso Peninsula. Japan. Earth Planets Space 51, 169-173.

Tzedakis, P.C., 2010. The MIS 11–MIS 1 analogy, southern European vegetation, atmospheric methane and the early anthropogenic hypothesis. Clim. Past 6, 131-144.

Tzedakis, P.C., Channell, J.E.T., Hodell, D.A., Skinner, L.C., Kleiven, H.F., 2012. Determining the natural length of the current interglacial. Nature Geosci. 5, 138–141.

Ujihara, A., 1986. Pelagic Gastropoda assemblages from the Kazusa Group of the Boso Peninsula, Japan and Plio-Pleistocene climatic changes. Journal of the Geological Society of Japan 92, 639-651 (in Japanese with English abstract).

Versteegh, G.J.M., 1994. Recognition of cyclic and non-cyclic environmental changes in the Mediterranean Pliocene: a palynological approach. Marine Micropaleontology, 23:147–183.

Versteegh, G.J.M., 1995. Palaeoenvironmental changes in the Mediterranean and North Atlantic in relation to the onset of northern hemisphere glaciations (2.5 Ma B.P.)—a palynological approach. Published doctoral dissertation; CIP Gegevens Koninklijke Bibliotheek, Den Haag, 134 p.

Versteegh, G.J.M., Zonneveld, K.A.F., 1994. Determination of (palaeo-)ecological preferences of dinoflagellates by applying detrended and canonical correspondence

analysis to Late Pliocene dinoflagellate cyst assemblages of the south Italian Singa section. Review of Palaeobotany and Palynology, 84:181–199.

Versteegh, G.J.M., Zonneveld, K.A.F, 2002. Use of selective degradation to separate preservation from productivity. Geology 30(7): 615-618. DOI: 10.1130/0091.

Wall, D., and Dale, B., 1966, "Living fossils" in western Atlantic plankton: Nature, v. 211, p. 1025–1026.

Wall, D., Dale, B., Lohman, G.P., Smith, W.K., 1977. The environmental and climatic distribution of dinoflagellate cysts in the North and South Atlantic Oceans and adjacent seas. Mar. Micropaleontol. 2, 121–200.

Warny, S.A., J.H., Wrenn., 1997. New species of dinoflagellate cysts from the Bou Regreg Core: a Miocene–Pliocene boundary section on the Atlantic Coast of Morocco. Review of Palaeobotany and Palynology, 96:281–304.

Williams, G.L., Lentin, J.K., Fensome, R.A., 1998. The Lentin and Williams index of fossil dinoflagellates; 1998 edition. American Association of Stratigraphy Palynologists Contributions Series 34, p 817.

Yin, Q.Z., Berger, A., 2012. Individual contribution of insolation and CO2 to the interglacial climates of the past 800,000 years. Clim. Dyn. 38, 709–724. doi: 10.1007/s00382-011-1013-5.

Yoshioka, K., 1973. Plant Geography. Kyoritsu-Shuppan publishing house, Tokyo, 84pp (in Japanese).

Zonneveld, K.A.F., Versteegh, G.J.M., de Lange, G.J., 1997. Preservation of organic-walled dino£agellate cysts in di¡er- ent oxygen regimes: A 10,000 year natural experiment. Mar. Micropaleontol. 29, 393–405.

Zonneveld, K.A.F., Versteegh, G.J.M., de Lange, G.J., 2001. Palaeoproductivity and post-depositional aerobic organic matter decay re£ected by dino£agellate cyst assemblages of the Eastern Mediterranean S1 sapropel. Mar. Geol. 172, 181–195.

Zonneveld, K.A.F., Marret, F., Versteegh, G.J.M., Bogus, K., Bonnet, S., Bouimetarhan, I., Crouch, E., de Vernal, A., Elshanawany, R., Edwards, L., Esper, O., Forke, S., Grøsfjeld, K., Henry, M., Holzwarth, U., Kielt, J.-F., So-Young, K., Ladouceur, S., Ledu, D., Chen, L., Limoges, A., Londeix, L., Lu, S.-H., Mahmoud, M.S., Marino, G., Matsouka[sic], K., Matthiessen, J., Mildenhal[sic], D.C., Mudie, P., Neil, H.L., 99 Pospelova, V., Qi, Y., Radi, T., Richerol, T., Rochon, A., Sangiorgi, F., Solignac, S.,

Turon, J.-L., Verleye, T., Wang, Y., Wang, Z., and Young, M., 2013, Atlas of modern dinoflagellate cyst distribution based on 2405 datapoints: Review of Paleobotany and Palynology, v. 191, p. 1–197.

APPENDIX 1

Descriptions of selected dinocyst and acritarch taxa

Genus *Brigantedinium* Reid 1977 ex Lentin et Williams 1993

Brigantedinium spp.

Plate 4, Figs. 4-6.

Description: Spherical cysts with a smooth surface. Wall is brown in colour and thin. The archeopyle is intercalary. No indication of tabulation. **Remarks:** Individual species could not be determined due to poor preservation.

Genus *Lingulodinium* Wall 1967 emend. Dodge 1989

Lingulodinium machaerophorum (Deflandre and Cookson 1955) Wall 1967

Plate 1, Figs. 7-9.

Description: Spherical cysts with a microgranulate to granulate cyst wall. The processes are hollow, randomly distributed on the central body and distally closed. The processes have a circular base, taper distally and tend towards flattening. The surface of the processes is usually smooth but may bear small spinules at the distal tips. Process form can greatly vary from short to long and from rounded to accuminate tips. Archeopyle formed by loss of one or more precingular plates. **Remarks:** Very few specimens were found with long processes.

Genus *Nematosphaeropsis* Deflandre and Cookson 1955 emend. Wrenn 1988

***Nematosphaeropsis labyrinthus* (Ostenfeld 1903) Reid 1974**

Plate 3, Figs. 7-9.

Description: Trabeculate cysts with an ovoidal central body. Surface of central body and processes is smooth. Processes are exclusively gonal, tall, slender and hollow with distal trifurcations. The bifurcate tips are connected to adjacent processes by parallel pairs of ribbon-like trabeculae that follow reflected plate sutures. Cyst body sometimes has an apical protuberance. Archeopyle is precingular formed by loss of 3'' plate.

Genus *Operculodinium* Wall 1967 emend. Matsuoka et al. 1997

***Operculodinium israelianum* (Rossignol 1962) Wall 1967**

Plate 1, figs 1-3.

Description: Central cyst body is subspherical to ovoidal with a relatively thick and granulate cell wall. Tabulation is not apparent from the process distribution. Processes are hollow with acuminate distal tips and fibrous at the base. Archeopyle formed by the loss of precingular plate 3''.

***Genus Protoceratium* Bergh 1881**

Cysts of *Protoceratum reticulatum* (Claparède and Lachmann 1859) Bütschli 1885

(=*Operculodinium centrocarpum* sensu Wall and Dale, 1966)

Plate 1, figs. 4-6.

Description: Spherical cysts with radiating slender processes, evenly distributed around the central body with no evidence of tabulation other than the archeopyle. The wall is thin and microgranular. Processes are hollow, circular in cross section and distally open sometimes with expanded tips. Archeopyle is formed by loss of single precingular plate (3''). **Dimensions:** Cyst body diameter 33-48 μm. Process length 7-14 μm. **Remarks:** All the specimens recorded had long (7-14 μm) processes. Cysts of *Protoceratum reticulatum* are recorded frequently in the Quaternary literature as *Operculodinium centrocarpum* sensu Wall and Dale (1966) (see Paez-Reyes and Head, 2013).

Genus *Protoperidinium* Bergh 1882

Cyst of *Protoperidinium nudum* Meunier 1999

Plate 3, Figs. 10-11.

Description: Small, spiny brown-pigmented cysts. Subspherical shape with weak polar compression. Very similar to *Selenopemphix quanta* but processes are relatively longer. Process bases are circular in cross-section. Cyst–theca relationship established by Wale and Dale (1968).

Genus *Pyxidinopsis* Habib 1976

Pyxidinopsis reticulata McMinn and Sun 1994 emend. Marret and de Vernal 1997

Plate 5, Figs. 1-3.

Description: Small spherical to subspherical cysts. Cell wall is covered by variable low muri that form an irregular, nontabular reticulum. Fields within the reticulum can be microgranulate to finely corrugate. No indication of tabulation. Archeopyle formed by loss of plate 3''.

Genus *Selenopemphix* Benedek 1972 emend. Head 1993

***Selenopemphix nephroides* Benedek 1972 emend. Bujak et al. 1980**

Plate 3, fig. 12 and Plate 4, fig. 1.

Description: The cyst is polar compressed with ovoidal outline in polar view. Wall is brown-pigmented, single layered and smooth. It bears low apical and antapical horns with rounded terminations. Cingulum is wide and deeply indented. The archeopyle is hexa-intercalary formed by the loss of plate 2a.

***Spiniferites hyperacanthus* (Deflandre and Cookson 1955) Cookson and Eisenack 1974**

Plate 2, figs 1-3.

Description: Spiniferate cyst with a broadly ovoidal to spheroidal central body. Microgranulate cell wall. Tabulation is weakly expressed due to very low and sometimes absent sutural crests. Both gonal and intergonal processes are present and are distally furcate with recurved trifurcate tips. Archeopyle formed by loss of plate 3''. **Remarks:** *Spiniferites hyperacanthus* is grouped with *S. mirabilis* and differs from it by not having the broad antapical flange.

***Spiniferites mirabilis* (Rossignol 1964) Sergent 1970**

Plate 1, figs 10-12.

Description: Spiniferate cysts having a broadly ovoidal to spheroidal central body with microgranulate wall. Tabulation is weakly expressed due to very low or sometimes absent sutural crests over most of the cyst. Both gonal and intergonal processes are present and are distally furcate with recurved bifurcate tips. Sutural crests at the antapex form a broad and conspicuous flange between antapical processes. Archeopyle formed by loss of plate 3''. **Remarks:** *S. mirabilis* is distinguished from *S. hyperacanthus* by the presence of a broad antapical flange that can only be distinguished when orientation and preservation are favourable (de Vernal et al., 1992).

Genus *Tuberculodinium* Wall 1967

***Tuberculodinium vancampoae* (Rossignol 1962) Wall 1967**

Plate 4, Figs 7-9.

Description: Cyst is subcircular in polar view and subrectangular in lateral view. The central body is supported by 30-50 distally connected barrel-shaped processes arranged in longitudinal rows. According to Matsuoka et al. (1998), the compound archeopyle is epicystal.

Genus *Xandarodinium* Reid 1977

***Xandarodinium xanthum* Reid 1977**

Plate 4, figs 3-4.

Description: Central body wall thin with a smooth surface. Processes are simple, circular or complex flanges and apparently tabular in distribution. The flanges are terminated by simple solid spines or multifurcate solid tips. Presence of one apical and two distinct antapical horn. Archeopyle formed by loss of a single intercalary plate.

Group ACRITARCHA Evitt 1963

Genus *Nannobarbophora* Habib and Knapp 1982

***Nannobarbophora walldalei* Head 1996**

Plate 5, Figs. 7-8.

Description: A species of *Nannobarbophora* having numerous, solid, tapering, and distally-closed processes. Small spinules present on process surfaces and is usually concentrated over distal half. The base of processes is usually fibrous and proximally expanded. Under light microscope, central body surface appears smooth.

APPENDIX 2:

Plate 1:

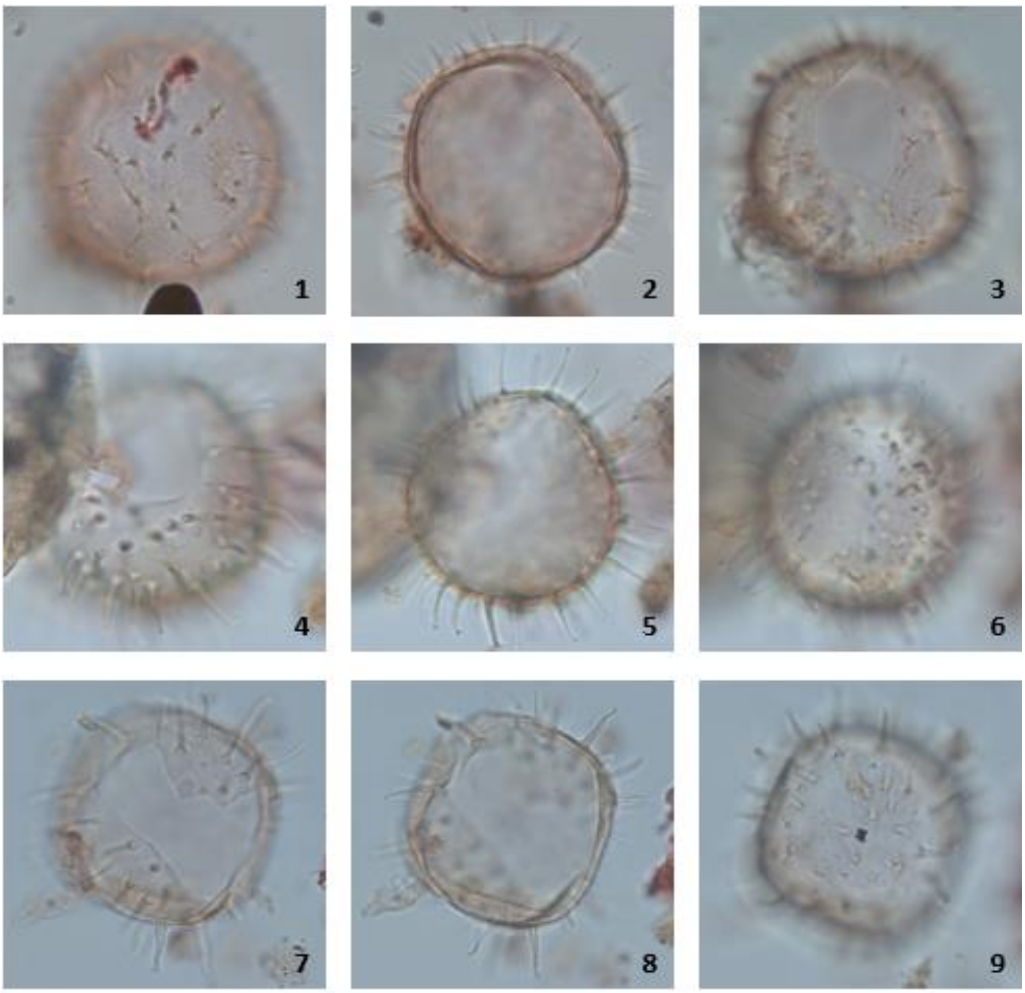

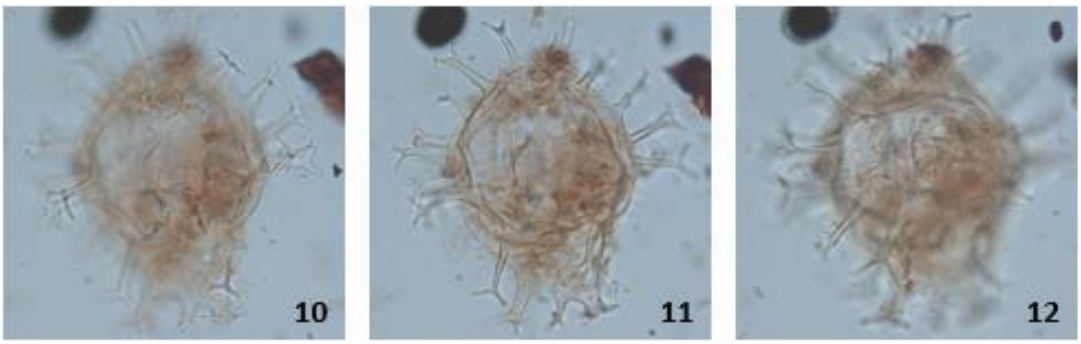

Figs. 1-3: *Operculodinium israelianum*. Ventral view of ventral surface, mid focus and dorsal surface. Diam. of central body: 48µm. Process length: 6 µm. Sample ID: TB 31, slide 1, W21/1.

Figs. 4-6: *Protoceratum reticulatum*. Dorsal view of dorsal surface, mid focus and ventral surface. Diam. of central body: 38 µm. Process length: 9 µm. Sample ID: TB2 26, slide 1, U37/3.

Figs. 7-9: *Lingulodinium machaerophorum*. Dorsal view of dorsal surface, mid focus, ventral surface. Diam. of central body: 45 µm. Process length: 10 µm. Sample ID: TB 16, slide 2, W42/4.

Figs. 10-12: *Spiniferites mirabilis*: Ventral view of ventral surface, mid focus and dorsal surface. Max. Diam. of central body: 65 µm. Process length: 21 µm. Sample ID: TB 16, slide 1, V17/3.

Plate 2:

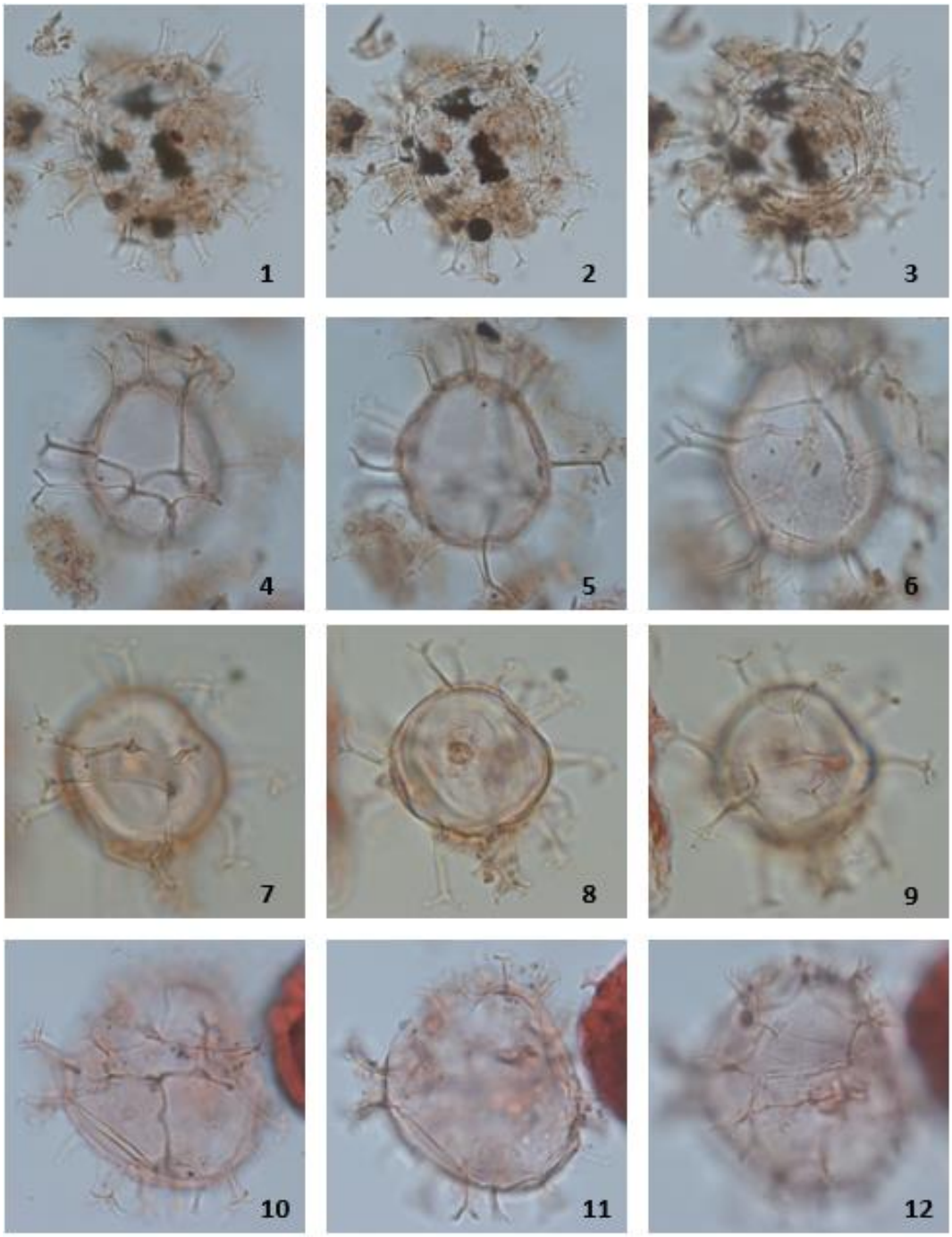

Figs. 1-3: *Spiniferites hyperacanthus*. Lower, mid and upper foci. Diam. of central body: 53 µm. Process length: 15-20 µm. Sample ID: TB 14, slide 1, B38/2.

Figs. 4-6: *Spiniferites* sp. 1. Dorsal view of dorsal surface, mid focus and ventral surface. Max. diam. of central body: 42µm. Process length: 12 µm. Sample ID: TB 16, slide 2, J30/3.

Figs. 7-9: *Spiniferites* sp. 2. Left lateral view of lower, mid and upper foci. Diam. of central body: 30 µm. Process length: 10 µm. Sample ID: TB 16, slide 2, L35/3.

Figs. 10-12: *Spiniferites* spp. Left lateral view of upper, mid and upper foci. Max. diam. of central body: 40 µm. Process length: 6 µm. Sample ID: TB 42, slide 1, V31/4.

Plates 3:

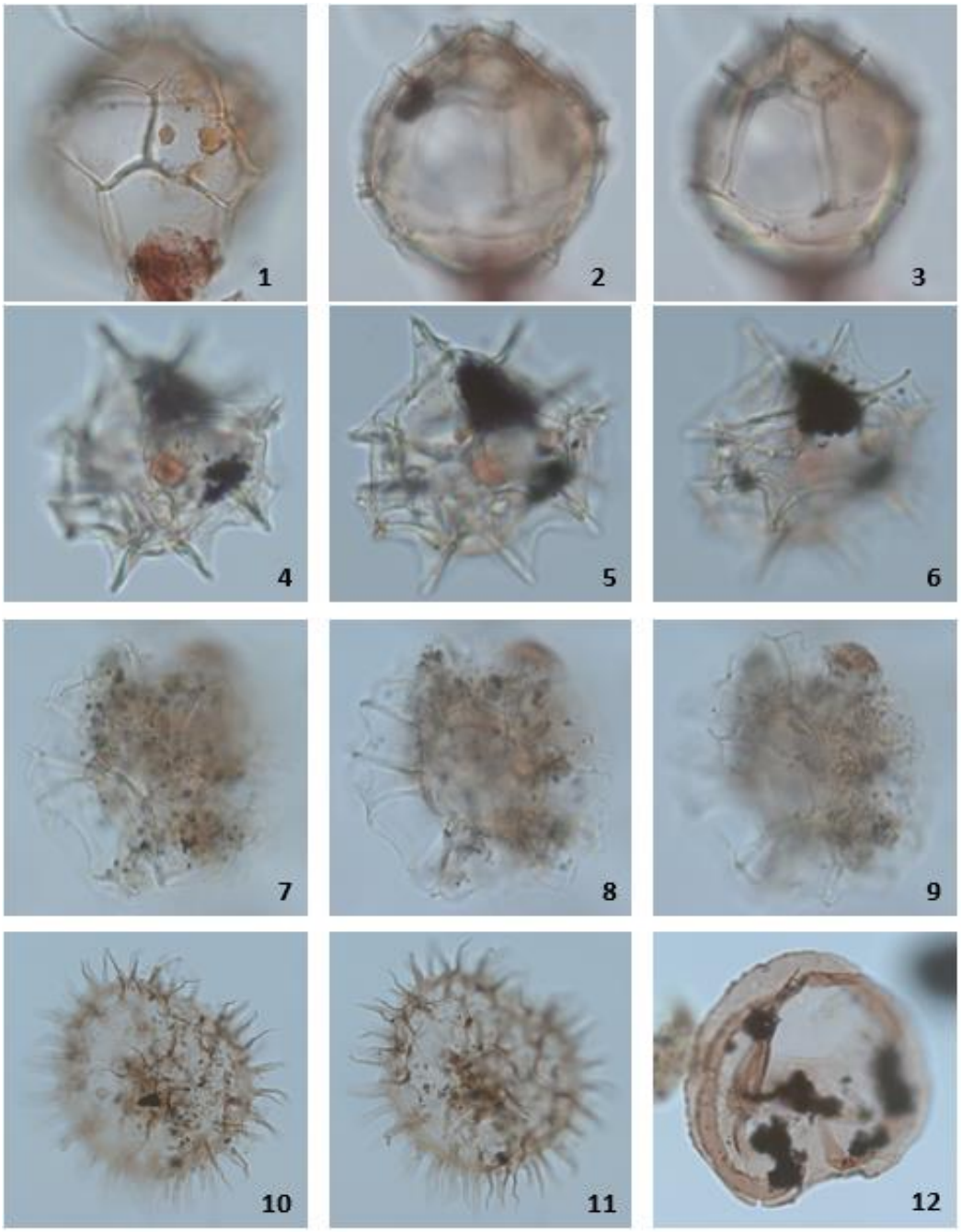

Figs. 1-3: *Impagidinium patulum*. Ventral view of ventral surface, mid focus and dorsal surface. Diam. of central body: 56µm. Process length: 5µm. Sample ID: TB2 26, slide 1, Q40/1.

Figs. 4-6: *Impagidinium aculeatum*. Lower, mid and upper foci. Diam. of central body: 33 µm. Process length: 7 µm. Sample ID: TB2 26, slide 1, E20/3.

Figs. 7-9: *Nematosphaeropsis labyrinthus*. Lower, mid and upper foci. Diam. of central body: 32 µm. Process length: 15 µm. Sample ID: TB2 32, slide 3, E31/0.

Figs. 10-11: *Selenopemphix quanta*: Lower and upper foci. Max. diam. of central body: 70 µm. Process length: 10 µm. Sample ID: TB 88, slide 2, W31/1.

Fig. 12: *Selenopemphix nephroides*: Apical view of lower focus.

Plates 4

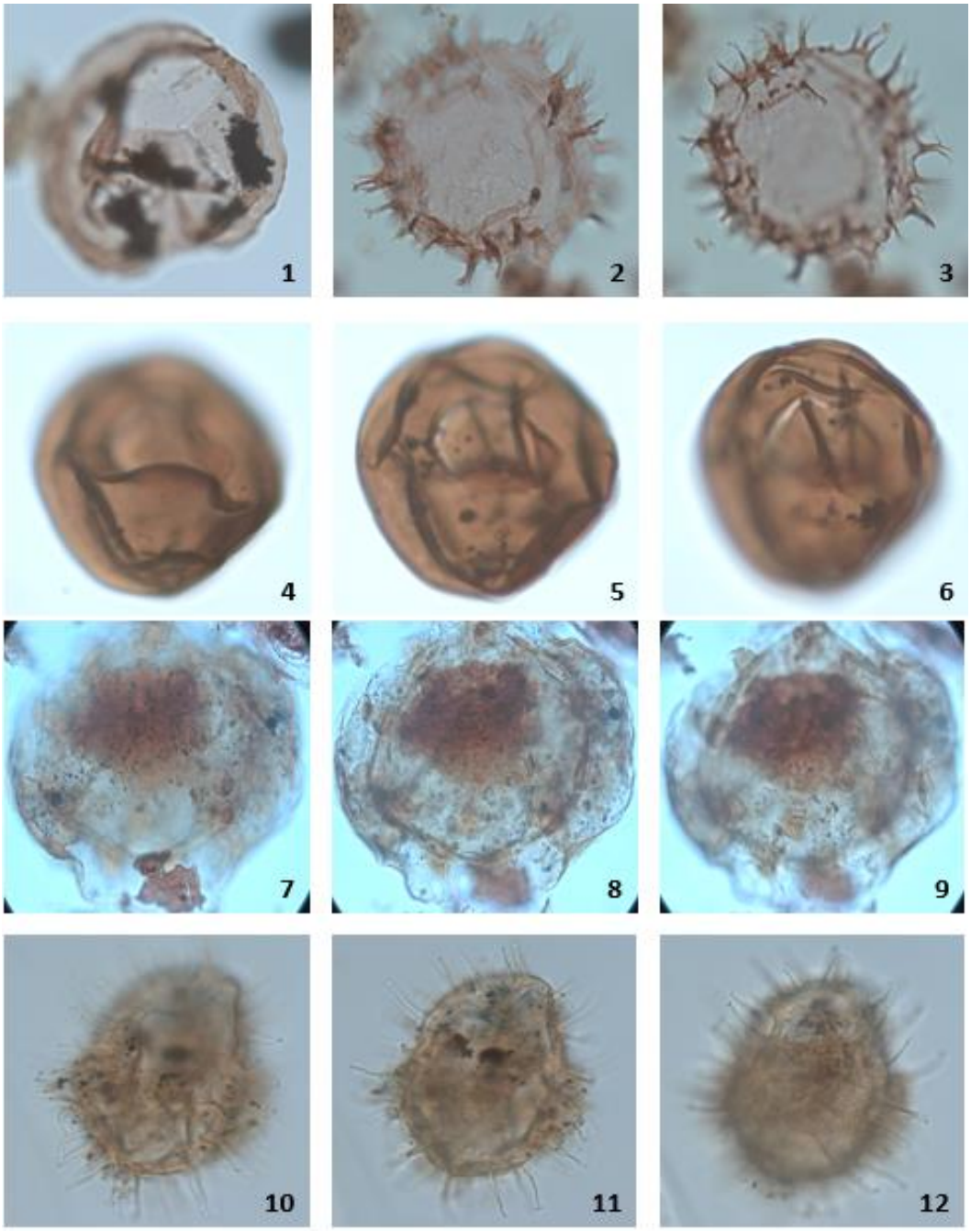

Figs. 1: *Selenopemphix nephroides*. Apical view of upper focus. Max. diam. of central body: 55 µm. Sample ID: 52, slide 2, E11/3.

Figs. 2-3: *Xandarodinium xanthum*. Lower and upper foci. Diam. of central body: 50 µm. Process length: 5 µm. Sample ID: 18, slide 1, F22/1.

Figs. 4-6: *Brigantedinium* spp. Dorsal view of dorsal surface, mid focus and upper surface. Diam. of central body: 35 µm. Sample ID: 72, slide 1, K38/1.

Figs. 7-9: *Tuberculodinium vancampoae*. Lower, mid and upper foci. Diam. of central body: 110 µm. Flange: 23 µm. Sample ID: TB2 30, slide 1, J32/2.

Fig. 10-12: *Cleistosphaeridium placacanthum* (reworked). Dorsal view of lower surface, mid focus and upper surface. Max. diam. of central body: 60 µm. Process length: 15 µm. Sample ID: 78, slide 2, H20/1.

Plates 5

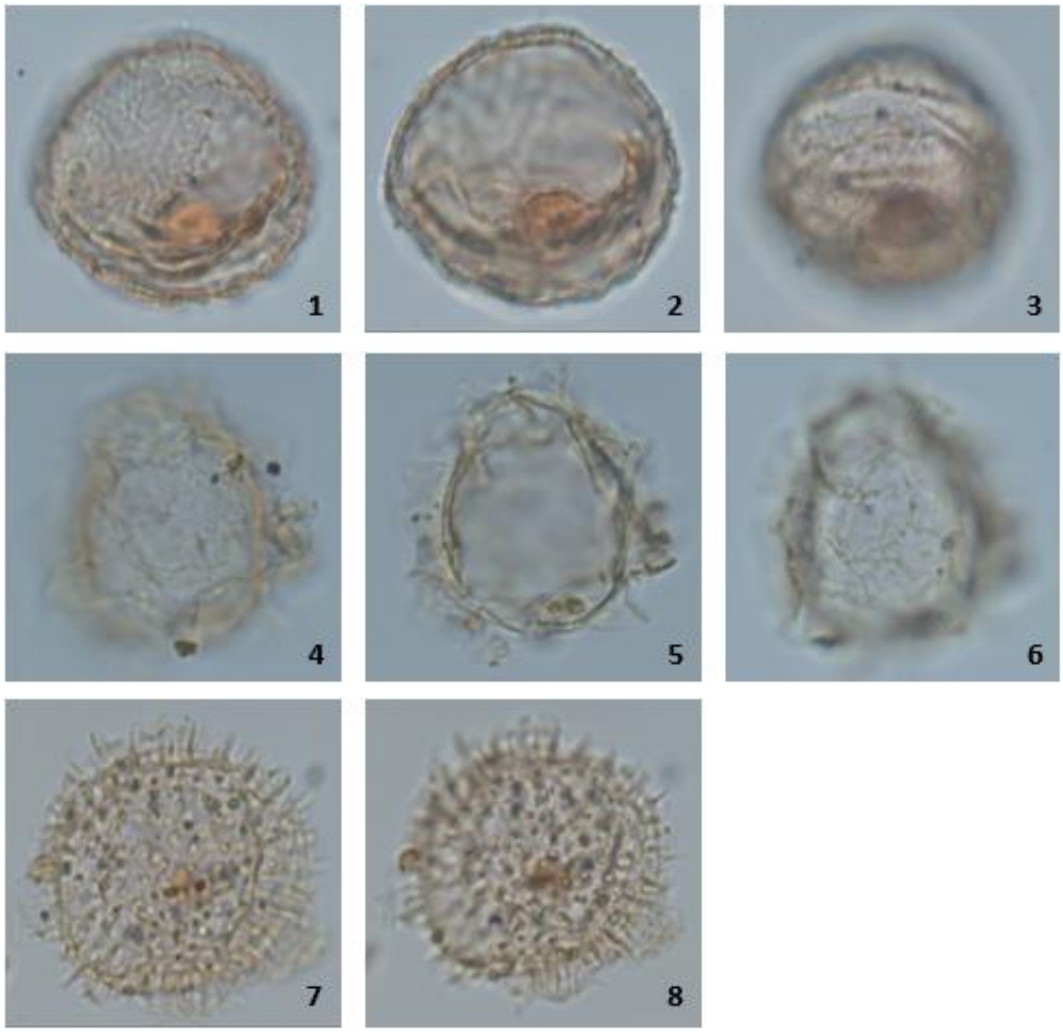

Figs. 1-3: *Pyxidinopsis reticulata*. Lower, mid and upper foci. Diam. of central body: 35 µm. Sample ID: 16, slide 1, S21/1.

Figs. 4-6: Cyst of *Scrippsiella trifida*. Lower, mid and upper foci. Max. diam. of central body: 30 µm. Flange: 5 µm. Sample ID: 56, slide 2, R39/3.

Figs. 7-8: *Nannobarbophora walldalei* (Acritarch). Lower and upper foci. Diam. of central body: 30 µm. Process length: 3 µm. Sample ID: TB2 30, slide 2, E15/3.

APPENDIX 3

3.1 Palynological processing

The palynological procedures used in the sample processing for this study follows the standard palynological processing of Earth Sciences department, Brock University (M.J. Head, January 2014: adapted from the MSc thesis of Fernando Mantilla Duran, Brock University, 2013). The sample processing was done in the Earth Sciences palynology laboratory, Brock University. It is noteworthy that during the sample processing some important laboratory precautions were followed. First, personal safety measures which involves the use of HF-rated gloves when working with HF in the fume hood and when using liquified phenol (used to prevent microbial growth in palynological residues). Sodium carbonate solution was always placed in the fume hood to neutralize drops of spilt HF and decontaminate gloves after use. Secondly, contamination between samples and residues was minimized to zero by preventing liquid splash and covering all containers during processing. Thirdly, residue loss when decanting was completely avoided which could possibly lead to biased counts and wrong interpretation.

Each of the 71 samples were placed in a baking cup and dried in the laboratory heating oven at a temperature of about 50^{o}C for approximately 5 hrs, they were then wrapped in an aluminium foil paper and gently crushed with a hammer on a flat steel plate. The sediment

samples were weighed to 10 grams each and gently transferred into a clean 400 ml beaker and covered with parafilm to avoid any airborne contamination prior to and during processing. The beakers were transferred into the fume hood and cold 20% conc. HCl was added. Due to the carbonate-rich composition of the samples, the HCl was introduced in small increments and gently swirling the sediments into suspension in the process to avoid a vigorous reaction that could induce overspill. 200 ml of HCl was gently added to each beaker and allowed to stand overnight to dissolve all carbonates, with the beaker firmly covered with parafilm. After overnight standing, the sediments were swirled into suspension, distilled water was added vigorously up to 500 ml and eventually decanted using a clean glass pipette until it is completely neutralized with a pH of about 6. After swirling the sediments into suspension, cold 38% conc. HF was added up to 200 mL to remove silicate fraction and swirled continuously 3 times a day for 5 days. After this, the HF was decanted and cold 38% conc. HF was added the second time up to 200 mL and swirled continuously 3 times a day for 5 days. The HF was decanted and the residue neutralized to a pH of 6. The residue was then transferred to a 50 mL screw-top disposable conical test tubes labelled with the same designated sample number used in the beakers. 40 ml of HCl was added again to remove any precipitates formed during HF treatment and left to stand for about 3 hours, distilled water was added and the supernatant was decanted using a centrifuge until it was neutralized to a pH of 6. In order to estimate the concentration of dinoflagellate cysts in each sample, 1 tablet of *Lycopodium Clavatum* (Batch number 1031) was added to each sample (Stockmarr, 1971). It was dissolved with little quantity of HCl and neutralized by decanting using centrifuge. The residue was sieved using 10 μm nylon mesh. After sieving, wet preparation did not indicate any need for ultrasound, hence no ultrasound was carried out on the samples. Sieved residue was transferred into 15 mL test tubes each and stained with one drop of safranin-o,

surplus stain was removed by mixing and decanting using a centrifuge. The sieved materials for each sample were then mounted on standard microscope slides using glycerine jelly on a slide warmer by adding 10 drops of residue on the cover slip. Surplus residue was stored in vials containing glycerine to which one drop of liquefied phenol had been added to prevent microbial growth. The prepared slides were all accurately labelled with the sample numbers assigned to each sample from the field. At least, 3 slides for each sample were prepared for microscopic study.

3.2 Palynological analysis and data collection

Palynological analysis was carried out on the prepared slides by examining and counting palynomorphs occurring on each slide using a Leica DM 2500 transmitted light microscope. During counting, each slide was scanned using a 40X magnification, while the 100X oil immersion objective lens was used for key analysis which involves detailed examination and identification of small palynomorphs, poorly preserved and obscured species, particularly small size acritarch. Also, the 20X magnification was used to count large size specimen. The main palynomorphs counted during the analysis was dinoflagellate cysts which is the focus of this study. However, other palynomorphs were also included in the counts, they include; foraminifera linings, bisaccate pollen, monosaccate (*Tsuga*) angiosperm pollen, fern and bryophyte spores and fungal spores. For dinocysts analysis, a minimum of 300 specimens were counted for each sample, and this number was achieved for most of the samples except for few samples (6) with low dinocyst concentration which yielded reduced counts, for these samples, a minimum of 200 specimens were counted. Also, 8 samples had less than 200 counts of dinocyst specimens, even after scanning up to 3 slides for each of them (see Table 1). An average of 500 *Lycopodium* spores were counted for each sample. The relative

abundance of only dinocysts and terrestrial palynomorphs were calculated based on the method of Stockmarr (1971).

For each sample, a nicely preserved specimen occurring on a particular slide was marked with an England Finder reference number. As mentioned earlier, a detailed morphological analysis mainly for identification purpose was performed on some species particularly dinocysts using a 100X oil objective lens. Photographs of specimens appearing nicely were all taken with a Leica 2500 MC 170 HD digital camera. Table 1 and 2 shows the complete count of all taxa encountered during the palynological analysis. All analysis was performed in the Earth Sciences department, Brock University.

APPENDIX 4

						Dinoflagellate cysts																																		
Subseries	**Magnetic Polarity**	**Age (Ma)**	**Depth**	**Biozonation**	**Sample No**	*Archomosphaera sp.*	*Brigantididum spp.*	*Cyst of P. nudum*	*I. aculeatum*	*I. patulum*	*I. paradoxum*	*I. sphaericum*	*Impagidinium Sp.*	*L.. machaerophorum*	*N. labyrinthus*	*P. reticulatum*	*O. israelianum*	*Protoperidinioid sp.*	*p. reticulata*	*Cyst of S. trifida*	*s. nephroides*	*S. nephroides 2*	*S. hyperacanthus*	*Spiniferitis indet*	*Spiniferitis mirabilis*	*Spiniferitis pacificus*	*Spiniferitis delicatus*	*Spiniferitis sp. 2*	*Spiniferitis sp. 3*	*Spiniferitis sp. 4*	*Spiniferitis spp.*	*T. vancampoae*	*X. xanthum*	*Dinocyst indet*	**TOTAL**	**Dinocyst concen.**	**No of *L*. counted**	**Sample weight/gram**	**No of *L*. tablet**	**No of *L*./tablet**
Early Pleistocene	Brunhes	768	3.45	Biozone 6	TB2 02	1							1		282											17		1							302	27374.3	23	10	1	20848
		768	3.25		TB2 04	3							6		232											55	2	6							304	23473.3	27	10	1	20848
		769	3.05		TB2 06	1			1				3		261							1				31	2	2							302	157402	4	10	1	20848
		769	2.85		TB2-08	1	6						8		221											55	2	9			1				303	52641.2	12	10	1	20848
		769	2.65		TB2-10	2	2						4		274							1				18	1	3							305	317932	2	10	1	20848
		769	2.45		TB2-12	2	1						5		270									1		21		2							302	52467.4	12	10	1	20848
		770	2.25		TB2-14	1	1						4	2	274											18	2	3							305	37403.7	17	10	1	20848
		770	2.05		TB2-16	1	1						11		268											13		7							300	29782.8	21	10	1	20848
		770	1.85		TB2-18	1	1						13		270	1				1						11		3							300	21567	29	10	1	20848
		771	1.65		TB2-20	1	1						6		250											33		8		2					300	23164	27	10	1	20848
		771	1.45		TB2-22	2	4						6		259							2				17		6		5	1				300	62544	10	10	1	20848
		771	1.25		TB2-24	1	6						14	1	243							3				17		12		4					300	26060	24	10	1	20848
Middle Pleistocene	Matuyama	772	1.05	Biozone 5	TB2-26	3	22	1	1				68		53			2		2		27		2		43	3	56		10	5				300	4667	134	10	1	20848
		772	0.85		TB2-28	2	38						53		13	2				1		22		6		56	5	76		24	2				300	1829	342	10	1	20848
		772	0.65		TB2-30	1	28				1		60	3	26	3			1	3		22		5		23	3	96		15	7				300	2424	258	10	1	20848
		773	0.45		TB2-32	3	30	1					99	1	15	1						19		6		22		86		11	7				300	1992	314	10	1	20848
		773	0.25		TB2-34	2	51						40	1	21	1			1		1	11		2	1	4		143	1	19					300	2064	303	10	1	20848
		773	0.05		TB 2	30	47		1				40		10				1	1	2	22		27	1	5	71	9		41	15				326	3503	194	10	1	20848
		774	-0.4		TB 4	52	63				1		18	1	15	1		2	4	3		10		6		4	66	10		85	5				352	2091	351	10	1	20848
		774	-0.6		TB 6	71	47						23		19	2			3	3		16	36	9		8	30	40		38	2				356	2595	286	10	1	20848
		775	-0.8		TB 8	25	62		1				37	2	10	1				1		49	37	17		6	19	34		20	2				325	2005	338	10	1	20848
		775	-1		TB 10	66	61	1					6	1	12					3	1	15	17	7	1	3	9	13		46	4				272	2383	238	10	1	20848
		775	-1.2		TB 12	183	52	1	2				29	1	18	6			2	9	5	40	30	7		6	26	2		45	11	1			483	1687	597	10	1	20848
		776	-1.4		TB 14	81	41	3	4				66	1	20	6			6	5		48	11	7		19	14	5		35	3				381	2414	329	10	1	20848
		776	-1.6		TB 16	129	30	1	3				29		17	6		1	5	2		62	14	21		41	21	14		20	6				424	2290	386	10	1	20848
		776	-1.8		TB 18	103	43	2	6				23		20	2				2	2	75	8	17		24	18	18		26	10				403	1949	431	10	1	20848
		777	-2		TB 20	63	34		3		1		20		28	12	1			1		45	6	18		39	34	13	1	39	4				363	1720	440	10	1	20848
		777	-2.2	Biozone 4	TB 22	46	29		1				80	1	21	9			5	2	1	25	15	11	1	33	25	15	2	22	1				346	1781	405	10	1	20848
		778	-2.4		TB 24	47	34		3				119		13	4	1		1	1		18	3	6		36	20	22	2	15	2				347	2067	350	10	1	20848
		778	-2.6		TB 26	51	18	1					139		15	6		6	2	2	1	13	3	2		16	12	25		35	2	2			353	2329	316	10	1	20848
		779	-2.8		TB 28	46	19						141		15	5		1	1	1		7	1	4		36	2	51		12	3	1			347	2929	247	10	1	20848
		779	-3		TB 30	29	27						140		28	8			2	1		14		14		14	5	24	1	22		1			330	2157	319	10	1	20848
		780	-3.2		TB 32	29	34		2				93		24	12	1		4	3		28	8	7		11		43	1	27	2				330	1844	373	10	1	20848
		780	-3.4		TB 34	31	19		1				143	1	19	12			2	2		15	2	6		15	4	30		27					300	1767	354	10	1	20848
		780	-3.6		TB 36	28	61		1				58	3	24	5			3			47		9		18	7	33		29					300	1390	450	10	1	20848
		781	-3.8		TB 38	50	40	1					75	2	37	3			3	2	1	11		2		30	35	35		17	1				300	1752	357	10	1	20848

Table 1: Summary of palynological analysis showing raw counts of dinocysts in all 71 samples from the Chiba section, Japan.

						Dinoflagellate cysts																																		
Subseries	**Magnetic Polarity**	**Age (Ma)**	**Depth**	**Biozonation**	**Sample No**	*Archomosphaera sp.*	*Brigantididum spp.*	*Cyst of P. nudum*	*I. aculeatum*	*I. patulum*	*I. paradoxum*	*I. sphaericum*	*Impagidinium Sp.*	*L.. machaerophorum*	*N. labyrinthus*	*P. reticulatum*	*O. israelianum*	*Prototoperidinoid sp.*	*p. reticulata*	*Cyst of S. trifida*	*s. nephroides*	*S. nephroides 2*	*S. hyperacanthus*	*Spiniferitis indet*	*Spiniferitis mirabilis*	*Spiniferitis pacificus*	*Spiniferitis delicatus*	*Spiniferitis sp. 2*	*Spiniferitis sp. 3*	*Spiniferitis sp. 4*	*Spiniferitis spp.*	*T. vancampoae*	*X. xanthum*	*Dinocyst indet*	**TOTAL**	**Dinocyst concen.**	**No of *L*. counted**	**Sample weight/gram**	**No of *L*. tablet**	**No of *L*./tablet**
Middle Pleistocene	**Matuyama**	781	-4	Biozone 3	TB 40	45	62		3				25	9	26	8				2		16	4	1		37	21	54	1	24	2	1			301	1609	390	10	1	20848
		782	-4.2		TB 42	60	55	3	3				13	13	32	7			4		2	7	3	1		20	26	79		25	2				300	1737	360	10	1	20848
		782	-4.4		TB 44	80	46	2	3				8	11	35	10			2	3		6		3		42	10	109	1	6	1				300	2896	216	10	1	20848
		783	-4.6		TB 46	95	31					1	27		20	5		2	5	1		5		1		46	28	102		21					300	2195	285	10	1	20848
		783	-4.7		TB 48	54	57						4	1	15	11			1	2	2	9		2		37	16	120		20					300	2387	262	10	1	20848
		784	-5	Biozone 2	TB 50	90	33		1				3	1	19	1			4		3	13				36	5	73		4					197	1222	336	10	1	20848
		784	-5.2		TB 51	119	28						5		13	6	1			2	2	10	3	2		45		60	2				1		299	1119	557	10	1	20848
		784	-5.3		TB 52	92	21		2				4		6	4			3	4		9		2		15	14	42		10					136	515	551	10	1	20848
		785	-5.4		TB 53	85	29		2			1	1		15	8				9	5	10	2			36		93			1		7		304	3122	203	10	1	20848
		785	-5.5		TB 54	70	25		1				5		13	1			1		3	10		2		6	3	57	1	4		1			132	1035	266	10	1	20848
		786	-5.6		TB 55	89	27						7	2	20	7				8	4	12	1			33	12	76			1		1		300	2950	212	10	1	20848
		788	-5.7		TB 56	84	18						2		8				1	3	2	5		3		7		45		10					104	1141	190	10	1	20848
		789	-5.8		TB 57	97	19					1	1		31	4				11	3	6	5	1		9	7	103					2		300	4115	152	10	1	20848
		789	-5.9		TB 58	93	50					1	6		44	2			5	7	5	5		4	1	7	4	121		36					298	2011	309	10	1	20848
		790	-5.9		TB 59	119	54						10		24		1			12	7	13		1	1	5		42		5			2		296	2844	217	10	1	20848
		790	-6.2		TB 60	131	45		1				6		18	3				11	3	22	4	2		7		43			2		1		299	1699	367	10	1	20848
		791	-6.3		TB 61	120	50	1	1				7		21	4	1			9	4	14	4					59					2		297	2538	244	10	1	20848
		791	-6.4		TB 62	87	43						9		31	1				13	5	14	5			14		75					2		299	3645	171	10	1	20848
		791	-6.5		TB 63	91	22	1	1				4		16	1	1			11	6	8	3		2			43			1		2		213	2659	167	10	1	20848
		791	-6.6		TB 64	96	33		1				4		8	1				2	7	9	2	3			1	48			1		2		218	3223	141	10	1	20848
		791	-6.7		TB 65	140	42			1			12		19	3				7	6	15	1	1				49			1		2		299	3281	190	10	1	20848
		791	-6.8		TB 66	95	46			1		1	8	1	23	2	1			13	8	15	1	1		1		77					7		301	2648	237	10	1	20848
		791	-6.9	Biozone 1	TB 70	83	9		1					1	9	2				9	6	9	1	1				15							146	1456	209	10	1	20848
		791	-6.9		TB 71	58	4						3		7	1				7	8	11	1	1				17					2		120	1737	144	10	1	20848
		792	-7		TB 72	98	19	1				1	5		15		3			14	12	16	4	5		2	4	23							222	1215	381	10	1	20848
		792	-7.1		TB 73	130	18						3		12		1			6	8	34	6	8		3	5	21					4		259	1385	390	10	1	20848
		792	-7.1		TB 74	75	13						2		2					2	3	11	2		1		1	9							121	1342	188	10	1	20848
		792	-7.3		TB 76	77	11						1	1	10					10	1	13	1	12		2	3	9					4		155	1110	291	10	1	20848
		792	-7.4		TB 78	278	5								1					4		2		1			1	8							300	3658	171	10	1	20848
		792	-7.6		TB 80	96	14	1	1				5	1	10	2				4	1	7	4	1		1	4	17					1		170	1136	312	10	1	20848
		792	-7.8		TB 82	119	8		1					1	8	6	1			7	4	4	2			1	1	27					3		193	1656	243	10	1	20848
		792	-7.9		TB 84	39	3						1		6	2				3	4	4		2		1		13					3		81	1011	167	10	1	20848
		792	-8.1		TB 86	111	12						4	4	9	4	3			10		9	2	3			1	36					1		209	1388	314	10	1	20848
		792	-8.3		TB 88	137	12						3	21	9	10				11	1	11	5				2	62					2		286	1812	329	10	1	20848
		792	-8.5		TB 90	59	7			1			1	5	8					1	2	6	1	2			4	12					3		112	1290	181	10	1	20848

Table 1: Continued.

Subseries	Magnetic Polarity	Age (Ma)	Depth	Sample No	Pollen and spores				Total pollen/spores	Foraminiferal linings	Acritarch	Reworked
					Bisaccate pollen	*Tsuga*	Angiosperm pollen	Spores			Nanobarbophora wall dalei (Acritarch)	*Cleistosph placacanthum*
Early Pleistocene	Brunhes	767.9	3.45	TB2 02	5	4	6	6	21	1		
		768.2	3.25	TB2 04	16	6	3	6	31	1	1	
		768.5	3.05	TB2 06	8	4	1	1	14	0		
		768.8	2.85	TB2-08	11	7	1	2	21	3		
		769.2	2.65	TB2-10	2	5	1	1	9	0		
		769.5	2.45	TB2-12	7	9	1	2	19	2		
		769.8	2.25	TB2-14	15	9	1	6	31	5	1	
		770.1	2.05	TB2-16	18	10	35	1	64	6	1	
		770.5	1.85	TB2-18	41	8	47	2	98	6		
		770.8	1.65	TB2-20	22	15	36	2	75	4	1	
		771.1	1.45	TB2-22	21	14	24	2	61	1	1	
		771.4	1.25	TB2-24	18	11	42	2	73	2		
		771.8	1.05	TB2-26	172	23	272	17	490	31	2	
Middle Pleistocene	Matuyama	772.1	0.85	TB2-28	228	95	287	16	626	17	4	
		772.4	0.65	TB2-30	344	109	466	18	937	53	15	
		772.7	0.45	TB2-32	289	74	210	23	596	35	4	
		773.1	0.25	TB2-34	252	82	188	9	531	33	4	
		773.4	0.05	TB 2	321	84	193	9	607	40	5	
		774	-0.35	TB 4	199	93	212	15	519	39	20	
		774.4	-0.55	TB 6	329	85	1365	48	1827	35	15	
		774.7	-0.75	TB 8	225	63	549	33	870	13	3	
		775	-0.95	TB 10	98	40	488	26	652	19	10	
		775.3	-1.15	TB 12	332	94	1029	43	1498	29	1	
		775.7	-1.35	TB 14	178	50	416	24	668	23	1	
		776	-1.55	TB 16	256	83	794	66	1199	29	1	
		776.4	-1.75	TB 18	472	85	479	29	1065	31	1	
		776.9	-1.95	TB 20	390	76	424	30	920	47		
		777.3	-2.15	TB 22	295	60	210	31	596	20		1
		777.8	-2.35	TB 24	221	60	209	11	501	21	1	
		778.2	-2.55	TB 26	276	40	382	10	708	28	2	
		778.7	-2.75	TB 28	219	42	262	8	531	14	1	
		779.1	-2.95	TB 30	193	45	112	2	352	41	3	
		779.6	-3.15	TB 32	120	56	179	8	363	29	2	
		780	-3.35	TB 34	131	36	151	6	324	8	1	
		780.4	-3.55	TB 36	186	48	184	4	422	35	1	1
		780.9	-3.75	TB 38	120	28	227	5	380	25		
		781.3	-3.95	TB 40	161	33	175	2	375	15	2	
		781.8	-4.15	TB 42	104	49	311	4	468	43	6	
		782.2	-4.35	TB 44	92	23	217	6	338	28	5	
		782.7	-4.55	TB 46	72	17	258	8	355	19	8	
		783.1	-4.75	TB 48	111	17	135	6	269	17	1	
		783.6	-4.95	TB 50	102	31	134	10	277	15	1	
		784	-5.15	TB 51	72	21	94	30	217	18		4
		784.4	-5.25	TB 52	94	43	238	9	384	20		
		784.9	-5.35	TB 53	71	28	6	10	115	16		2
		785.3	-5.45	TB 54	80	27	164	7	278	16		
		785.8	-5.55	TB 55	43	22	2	10	77	6		1
		788.2	-5.65	TB 56	69	17	146	8	240	9		
		788.7	-5.75	TB 57	112	38	6	12	168	21	1	3
		789.1	-5.85	TB 58	93	54	307	27	481	12	4	
		789.6	-5.9361	TB 59	128	70	28	22	248	19	3	
		790	-6.15	TB 60	165	107	18	23	313	35	1	
		790.6	-6.25	TB 61	123	85	26	24	258	21	1	
		791	-6.35	TB 62	130	61	18	16	225	31		1
		791	-6.45	TB 63	205	112	22	35	374	26		1
		791.1	-6.55	TB 64	168	109	15	28	320	16	1	
		791.1	-6.65	TB 65	182	152	24	34	392	40	1	3
		791.2	-6.75	TB 66	65	102	16	27	210	19	1	4
		791.4	-6.85	TB 70	111	120	6	17	256	13		
		791.5	-6.9204	TB 71	112	112	16	17	257	18		
		791.5	-7	TB 72	94	128	13	22	257	21		
		791.6	-7.0919	TB 73	174	186	31	33	424	19	1	3
		791.6	-7.1	TB 74	88	112	6	13	219	9		1
		791.7	-7.2633	TB 76	87	129	7	29	252	9		1
		791.8	-7.426	TB 78	99	89	5	14	207	10		3
		791.9	-7.586	TB 80	224	200	14	21	459	13		3
		791.9	-7.786	TB 82	167	145	11	14	337	17	1	2
		792	-7.946	TB 84	150	100	9	13	272	6		3
		792.1	-8.1083	TB 86	216	190	11	27	444	9		5
		792.4	-8.3163	TB 88	248	177	9	16	450	28		2
		792.4	-8.455	TB 90	228	116	8	18	370	9		3

Table 2: Summary of palynological analysis showing raw counts of pollen and spores, foraminiferal linings, acritarch and reworked dinocysts in all 71 samples from the Chiba section, Japan.